A Measurement of Tau Lepton Polarization Using the L3 Detector at LEP

Thomas Cantzon Paul

A thesis submitted to

The Johns Hopkins University

in conformity with the requirements for the degree of
Doctor of Philosophy

Baltimore, Maryland
1994

Abstract

We report on the measurement of the average polarization and forward-backward polarization asymmetry of tau leptons produced in electron-positron collisions at the Large Electron Positron (LEP) collider at the European Laboratory for Particle Physics (CERN). The data was collected using the L3 detector during 1990, 1991, 1992, and 1993 and consists of approximately 86 000 $Z \to \tau^+\tau^-$ events. The tau polarization was determined as a function of the production polar angle using the following 1-prong decay modes: $\tau^- \to e^-\bar{\nu}_e\nu_\tau$, $\tau^- \to \mu^-\bar{\nu}_\mu\nu_\tau$, $\tau^- \to \pi^-\nu_\tau$, $\tau^- \to \rho^-\nu_\tau$, and $\tau^- \to a_1^-\nu_\tau$. From this measurement we obtain the following ratio of vector- to axial-vector weak neutral couplings for taus and electrons: $g_V^\tau/g_A^\tau = 0.0752 \pm 0.0063(\text{stat.}) \pm 0.0045(\text{syst.})$, $g_V^e/g_A^e = 0.0791 \pm 0.0099(\text{stat.}) \pm 0.0025(\text{syst.})$. This is consistent with the hypothesis of $e - \tau$ universality of the weak neutral current. Assuming lepton universality, we find the effective weak mixing angle $\sin^2\theta_W^{\text{eff}} = 0.2309 \pm 0.0016$.

Thesis Advisor: Professor Peter Fisher

Contents

List of Figures

List of Tables

Acknowledgements

Since L3 is a large collaboration, the analysis presented in this thesis is ultimately the result of the efforts of scores of people; I first make the lame but unavoidable gesture of thanking them all collectively. More directly I wish to thank my advisor, Peter Fisher, for much help and guidance, as well as Aihud Pevsner for supporting me. I owe a great deal to Andrei Kunin who led the tau polarization analysis, acting as de facto advisor to a number of students, and who is responsible for the quality of the results presented here. I thank Krishna Kumar for getting me started and for writing reference letters, Andreas Gougas, who helped with a spectrum of problems, and Wayne Kinnison who looked after me while I was at Los Alamos. I'm indebted to many people for providing useful bits of code, computer incantations, insight or enlightening conversations; I thank especially Jayant Shukla, John Swain, Lucas Taylor, David McNally, Pratibha Vikas, Rizwan Khan, Ian Scott, and James Gerald.

I offer many thanks to friends encountered on the way through school. A number of them are included in the names above, but I don't want to forget Mark, Amanda, Eric, Brian, Rafa, Wes, and Suman, all in Baltimore, and Carolyn in Los Alamos.

Above all I thank my parents for their unwavering support.

Chapter 1

Theory and Motivation

The theory of weak and electromagnetic interactions, or Standard Electroweak Model (SM), was placed on solid experimental footing with the discoveries of the $W^{\pm}$ and Z bosons at the CERN Super Proton-Antiproton Synchrotron in 1983 [13]. Since that time the structure of the charged and neutral weak currents mediated by these particles has been studied in more detail, and much of the progress on this front is a product of e^+e^- colliding beam machines operating at center of mass energies on and around the Z peak. The copious Z production at the Large Electron Positron collider (LEP) at CERN and the beam polarization achieved at the SLAC Linear Collider (SLC) have made possible high precision measurements of the parameters of the Z resonance. Such precision measurements serve not only to check the SM, but can be used to constrain parameters like the top and higgs masses within the context of the model. Large deviations from the SM predictions which cannot be accounted for by variations in these less precisely known parameters would also point the way to physics beyond the Standard Model.

In the following chapters we present results of a precision measurement of several $Z \to f^+f^-$ coupling constants. First a brief historical outline is given to place the τ polarization measurement in its experimental context. The main points of the SM are then summarized with emphasis on the structure of the coupling of fermions to the Z and their relation to the weak mixing angle, $\sin^2\theta_W$. This is followed by a short section on quantum corrections. Next we discuss observables in the reaction $e^+e^- \to Z \to f^+f^-$ which can be used to infer the values of the Z to fermion coupling constants. The goal here is to demonstrate the merits of the measurement of final state lepton polarization. Finally we discuss radiative corrections.

1.1 Introduction

The phenomenology that makes the τ polarization interesting was born in the context of the Fermi theory of β decay [1]. In analogy with Quantum Electrodynamics (QED), Fermi expressed the decay $n \rightarrow p^+e^-\bar{\nu}_e$ as a current-current interaction,

$$\mathcal{M} = \frac{G_F}{\sqrt{2}} J^{\dagger}_{\mu(\text{baryon})} J^{\mu}_{(\text{lepton})} \tag{1.1}$$

where $J^{\dagger}_{\mu(\text{baryon})}$ is the charge raising weak current coupling neutrons to protons and $J^{\mu}_{(\text{lepton})}$ is the charge lowering current connecting electrons with neutrinos. The coupling constant G_F determines the strength of the interaction.

The form of the weak current was revealed through a number of experiments, beginning with the observation of parity violation in the β decay of ^{60}Co by C.S. Wu and collaborators in 1957 [2]. This was quickly followed up by numerous experiments, not only confirming parity violation in other systems [3], but indicating that parity violation is maximal; only neutrinos of a single helicity participate [4] and they happen to be left-handed [5]. These experiments, together with the first direct observation of neutrino interactions [6] made the case for the $V-A$ version of the Fermi theory [29], in which the lepton current of equation 1.1 may be written,

$$J^{\mu}_{(\text{lepton})} = \bar{\psi}_e \gamma^{\mu} \left(1 - \gamma^5\right) \psi_{\nu} \tag{1.2}$$

This current involves only left-handed neutrinos (see section 1.3).

The $V-A$ theory was a satisfactory description of the data at low energies, but predicted a νe scattering amplitude which diverged at high energy. It had been apparent for some time that the Fermi theory might better be formulated as an Intermediate Vector Boson (IVB) theory, like QED, in which a vector boson transmits the force. Owing to the weakness of weak interactions, the boson would presumably be heavy; the original Fermi theory would be the low energy limit of the IVB theory. Attempts to construct a theory of weak interactions with heavy vector bosons ultimately resulted in the Standard Electroweak Model. The SM contains the heavy charged bosons involved in the charge-raising and lowering currents of the Fermi theory (the $W^{\pm}$ bosons), as well as the photon and a third neutral heavy boson, the Z. The SM, with its introduction of a new weak neutral current, solved the divergent amplitude problem of the Fermi theory, and furthermore proved to be renormalizable [7], meaning amplitudes could be calculated in all orders of the coupling constants.

The first evidence for weak neutral currents came in 1973 from the Gargamelle bubble chamber experiment at CERN [8]. This experiment used beams of muon neutrinos and antineutrinos incident on a freon-filled bubble chamber. Neutral current interactions produce events of the type $\nu_\mu \mathrm{N} \to \nu_\mu \mathrm{X}$, distinct from the charged current interactions, which produce $\nu_\mu \mathrm{N} \to \mathrm{X}\mu^-$ events. Thus the signature for the weak neutral current was hadronic energy produced by a neutral particle and no associated muon.

A later experiment by Prescott and collaborators [9] at SLAC revealed a minute parity violation in the scattering of polarized electrons off a deuterium target, a result of the interference of photon and Z exchange. The experiment involved measuring the asymmetry,

$$A = \frac{\sigma_R - \sigma_L}{\sigma_R + \sigma_L} \tag{1.3}$$

where $\sigma_{R(L)}$ is the cross section for scattering right(left)-handed electrons. The electron polarization was controlled in two ways. First, the circular polarization of the light used to eject the polarized electrons from a gallium arsenide crystal was varied using a combination of a prism and Pockels cell, a crystal with birefringence proportional to an applied electric field. Second, the beam energy was varied. Since the electron beam was magnetically bent before striking the target, the longitudinal component of the electron spin precessed an amount proportional to the beam energy. The scattered electrons were then momentum analyzed in a magnetic spectrometer and the flux measured as a function of the electron polarization, yielding the result depicted schematically in Figure 1.1. This experiment was able to measure a phenomenally small asymmetry of order 0.001%. Thus the neutral current was shown to violate parity, as the charged current does.

In the SM, the relationships among the boson masses and couplings are prescribed by three parameters which must be determined from experiment. The fine structure constant α and the Fermi coupling G_F may serve as two of the input parameters. Neutral current experiments like the ones described above yielded a third input, the phenomenological parameter $\sin^2\theta_W$ (see section 1.2). Given these three parameters, the SM predicts the masses of the $W^\pm$ and Z bosons. This prediction sparked the effort at CERN to convert the existing Super Proton Synchrotron to a colliding proton-antiproton machine in order to achieve the energies necessary to directly produce the $W^\pm$ and Z. By 1983 these particles were found with their predicted masses by the UA1 and UA2 collaborations, a spectacular confirmation of the Standard Model.

Since 1989, the LEP $\mathrm{e}^+\mathrm{e}^-$ collider has provided an abundant source of Z bosons.

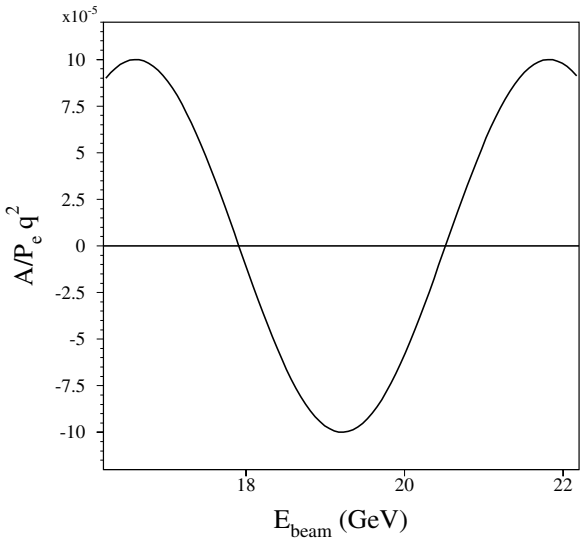

Figure 1.1: General shape of the asymmetry, A, as a function of beam energy in the Prescott experiment. $P_{\rm e}$ is the electron polarization and q^2 is the momentum transfer of the electron. The asymmetry is predicted to depend on q^2 at the level of $10^{-4}q^2$.

At center of mass energies near M_Z, Z production is enhanced by about a factor of 1000 over photon exchange. Furthermore e^+e^- collisions are free from the hadronic debris that accompanies colliding protons. This has provided an ideal environment for detailed study of the Z. As we shall see in the following chapters, the τ polarization measurement is a means of studying weak neutral currents using τ's. The essential phenomenon is parity violation, and the goal of the measurement is determination of the vector and axial-vector coupling constants which enter into the weak neutral current.

1.2 Standard Electroweak Model

In the Standard Electroweak Model [12] spontaneous breaking of an $SU(2)_L \otimes U(1)_Y$ local guage symmetry leads to one massless and three massive vector bosons with coupling strengths to fermions and to each other determined (at tree level) by three parameters. The fermions are grouped into left-handed weak isospin doublets and right-handed singlets, as summarized in Table 1.1.

	Q	Y	T	T^3
$\begin{pmatrix}\nu_e\\ e\end{pmatrix}_L$ $\begin{pmatrix}\nu_\mu\\ \mu\end{pmatrix}_L$ $\begin{pmatrix}\nu_\tau\\ \tau\end{pmatrix}_L$	0	-1	$1/2$	$+1/2$
	-1	-1	$1/2$	$-1/2$
e_R μ_R τ_R	-1	-2	0	0
$\begin{pmatrix}u\\ d'\end{pmatrix}_L$ $\begin{pmatrix}c\\ s'\end{pmatrix}_L$ $\begin{pmatrix}t\\ b'\end{pmatrix}_L$	$+2/3$	$+1/3$	$1/2$	$+1/2$
	$-1/3$	$+1/3$	$1/2$	$-1/2$
u_R c_R t_R	$+2/3$	$+4/3$	0	0
d'_R s'_R b'_R	$-1/3$	$-2/3$	0	0

Table 1.1: Quantum numbers for fermions in the SM. The primes on the quarks are to indicate that the mass eigenstates do not correspond to the electroweak eigenstates.

The $SU(2)_L$ subgroup is associated with a triplet of weak isospin currents that couple with strength g to three vector fields $\vec{W}_\mu$. The fields

$$W_\mu^\pm = \sqrt{\frac{1}{2}}\left(W_\mu^1 \mp iW_\mu^2\right) \tag{1.4}$$

couple to weak isospin raising and lowering parts of the current; these fields are the $W^\pm$ bosons. The weak isospin raising and lowering currents are associated with transitions between the elements in the left-handed isospin doublets shown in the table. This embodies the experimental observations of maximal parity violation in the weak charged current as well as lepton number conservation, since only left-handed leptons from the same generation enter into the current.

The remaining field, W_μ^3, which couples to the charge-preserving current cannot be associated with the photon or the Z because these two particles are observed to interact with both right- and left-handed matter. Glashow first enlarged the $SU(2)_L$ scheme to $SU(2)_L \otimes U(1)_Y$. Y is the hypercharge,

$$Y = 2\left(Q + T^3\right) \tag{1.5}$$

where Q is the charge and T^3 is the third component of the weak isospin. Y is a conserved quantity under a rotation in $SU(2)_L$ weak isospin space (see Table 1.1). The current associated with this subgroup couples with a strength conventionally

written $g'/2$ to a single vector field B_μ. As a consequence of symmetry breaking, the process which gives mass to the vector bosons, the two neutral fields in the model, W^3_μ and B_μ, mix to form the physical Z and photon fields,

$$\begin{aligned} A_\mu &= B_\mu \cos\theta_W + W^3_\mu \sin\theta_W \\ Z_\mu &= -B_\mu \sin\theta_W + W^3_\mu \cos\theta_W \end{aligned} \tag{1.6}$$

where the parameter θ_W is known as the weak mixing angle. The identification of A_μ with the photon leads to a relation between the electromagnetic coupling, $e = \sqrt{4\pi\alpha}$, the $\mathrm{SU(2)_L}$ and $\mathrm{U(1)}_Y$ couplings g and g', and the parameter θ_W,

$$e = g \sin\theta_W = g' \cos\theta_W \tag{1.7}$$

Requiring agreement between the Fermi $V-A$ theory of beta decay and SM calculations leads to the relation between the Fermi coupling and SM parameters,

$$\frac{G_F}{\sqrt{2}} = \frac{g^2}{8M_W^2} = \frac{\pi\alpha}{2\sin^2\theta_W M_W^2} \tag{1.8}$$

where M_W is the mass of the $W^\pm$ boson. Further, the SM predicts that the masses of the W and the Z are related by the weak mixing angle [15],

$$\frac{M_W}{M_\mathrm{Z}} = \cos\theta_W \tag{1.9}$$

Combining equations 1.7, 1.8, and 1.9 yields,

$$\sin^2\theta_W \cos^2\theta_W = \frac{\pi\alpha}{\sqrt{2}G_F M_Z^2} \tag{1.10}$$

relating the weak mixing angle to three precisely measured quantities, summarized in Table 1.2. Equation 1.10 will be useful for the discussion of quantum corrections in section 1.4.

The weak neutral current that couples to Z_μ is given by,

$$-i\frac{g}{\cos\theta_W}\bar{\psi}^f\gamma^\mu\left[T^3\frac{1}{2}\left(1-\gamma^5\right) - Q\sin^2\theta_W\right]\psi^f Z_\mu \tag{1.11}$$

This is commonly written in terms of the so-called vector and axial-vector coupling constants, which are defined,

$$\begin{aligned} g_V^f &= T^3 - 2Q\sin^2\theta_W \\ g_A^f &= T^3 \end{aligned} \tag{1.12}$$

Parameter	Value	Uncertainty (ppm)
α [50]	1/137.0359895	0.045
$G_F/(\hbar c^3)$ [51]	1.16639×10^{-5} GeV^{-2}	20
M_{Z} [52]	91.1888 GeV	48

Table 1.2: Precisely measured parameters in the SM.

where f labels the fermion type. We note that if lepton universality is assumed, then g_V^f and g_A^f are the same for all leptons. Equations 1.11 and 1.12 lead to the vertex factor show in in Figure 1.2.

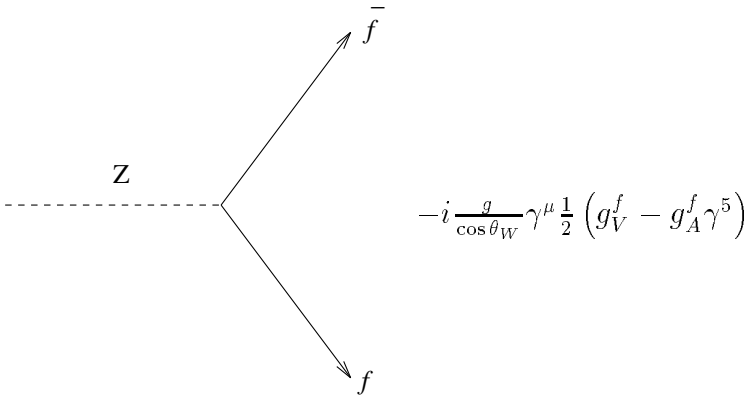

Figure 1.2: Vertex factor for $\mathrm{Z} \to f\bar{f}$.

From equations 1.12 and the numbers in Table 1.1 we get the following relation between the lepton coupling constants and the weak mixing angle,

$$\frac{g_V^\ell}{g_A^\ell} = 1 - 4\sin^2\theta_W \tag{1.13}$$

This relation will be useful in the sections 1.6 where we discuss the sensitivity of the various final state fermion asymmetries to $\sin^2\theta_W$.

1.3 Helicity and parity violation

We now recall the definitions of chirality, or "handedness," and helicity. In the Weyl representation [15] the Dirac equation reads,

$$\begin{pmatrix} -\vec{\sigma}\cdot\vec{p} & m \\ m & \vec{\sigma}\cdot\vec{p} \end{pmatrix}\psi = E\psi \tag{1.14}$$

where $\vec{\sigma}$ is the vector of Pauli matrices, m is the mass, and $\vec{p}$ is the momentum. We write the four-component spinor ψ in terms of two-component spinors,

$$\psi = \begin{pmatrix} \omega \\ \phi \end{pmatrix} \tag{1.15}$$

In this representation,

$$\gamma^5 = \begin{pmatrix} -I & 0 \\ 0 & I \end{pmatrix} \tag{1.16}$$

so that,

$$\begin{aligned} \frac{1}{2}\left(1-\gamma^5\right)\psi &= \begin{pmatrix} I & 0 \\ 0 & 0 \end{pmatrix}\psi = \begin{pmatrix} \omega \\ 0 \end{pmatrix} \equiv \psi_L \\ \frac{1}{2}\left(1+\gamma^5\right)\psi &= \begin{pmatrix} 0 & 0 \\ 0 & I \end{pmatrix}\psi = \begin{pmatrix} 0 \\ \phi \end{pmatrix} \equiv \psi_R \end{aligned} \tag{1.17}$$

$$\tag{1.18}$$

defining the left- and right-handed components of ψ.

Equation 1.14 can be rewritten using 1.15,

$$\begin{aligned} \frac{\vec{\sigma}\cdot\vec{p}}{|\vec{p}|}\omega &= \frac{-E}{|\vec{p}|}\omega + \frac{m}{|\vec{p}|}\phi \\ \frac{\vec{\sigma}\cdot\vec{p}}{|\vec{p}|}\phi &= \frac{E}{|\vec{p}|}\phi - \frac{m}{|\vec{p}|}\omega \end{aligned} \tag{1.19}$$

In the limit $m \to 0$, equations 1.19 decouple leaving ω and ϕ as eigenstates of the helicity operator, $\vec{\sigma}\cdot\hat{p}$.

$$\begin{aligned} \sigma\cdot\hat{p}\omega &= -\omega \\ \sigma\cdot\hat{p}\phi &= \phi \end{aligned} \tag{1.20}$$

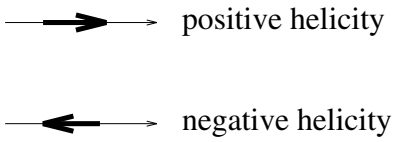

Figure 1.3: Representation of positive and negative helicity states. The thin arrows indicate the momentum and the thick arrows represent the spin projection along the momentum direction.

As evident from the helicity operator, helicity is the projection of the spin along the direction of motion, as indicated schematically in Figure 1.3. Notice that in the massless limit the left- and right-handed spinors ψ_R and ψ_L are identical to the definite helicity states. For $m \neq 0$ there is a contribution from the "wrong" helicity state which is supressed by a factor $1/\gamma$.

The vertex factor in Figure 1.2 contains a linear combination $\frac{1}{2}(1-\gamma^5)$ and $\frac{1}{2}(1+\gamma^5)$, so that in general the Z couples preferentially to either left- or right-handed fermions. Evidently parity is violated in Z decays. In the decay $Z \to \nu\bar{\nu}$, for example, equation 1.12 indicates that $g_V^f = g_A^f = 1/2$, so the Z couples exclusively to left-handed neutrinos; the neutrinos are 100% polarized. In the case of the other fermions, the coupling depends on the value of $\sin^2\theta_W$ (see equation 1.12). As we shall see in section 1.6, inserting realistic values of $\sin^2\theta_W$ into equation 1.12 reveals that the charged leptons are about 15% polarized. In contrast, b quarks are produced with a polarization of about 94%.

1.4 Quantum corrections

We have seen in the previous section that the Standard Model determines tree-level relations between the vector boson masses, two coupling strengths, and the weak mixing angle (see equations 1.7, 1.8, and 1.9. The full phenomenology, however, must include all the amplitudes connecting initial and final states. Of particular interest is the correction to the tree level relations resulting from the interaction of Z and $W^{\pm}$ bosons with virtual heavy quarks or with the higgs field,

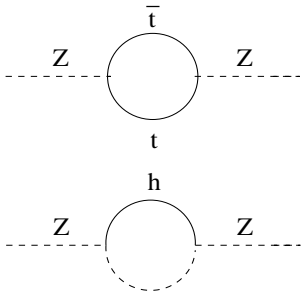

Diagrams like these introduce a correction to equation 1.10 of the form [62],

$$\sin^2\theta_W \cos^2\theta_W = \frac{\pi\alpha}{\sqrt{2}G_F}\frac{1}{1-\Delta r(m_t, m_h)} \tag{1.21}$$

Δr depends quadratically on m_t and logarithmically on m_h, and is thus much more sensitive to the top mass than the higgs mass. α, G_F, and M_Z have all been measured with high precision (see Table 1.2). $\sin^2\theta_W$ can be precisely determined[1] from measurements of the couplings of fermions to the Z (see equation 1.13). These measurements then determine Δr, thus providing an indirect measurement of the top and higgs masses. A Δr value to large to be accounted for within the context of the SM would indicate the need for a new or extended theory.

1.5 Asymmetries in $e^+e^- \to Z \to f^+f^-$

We now examine the process $e^+e^- \to f^+f^-$ at $\sqrt{s} \approx M_Z$ to find out how observables in this reaction are related to parameters in the Standard Model. First a simple pictorial argument will be used to suggest independent observables to pursue. Next, we find the relationship between these observables and the couplings of the fermions to the Z.

We will assume that all fermions are massless. This is quite a reasonable approximation since the heaviest fermion kinematically allowed in Z decays is the b quark, whose mass of between 4.1 and 4.5 GeV [30] is much smaller than $M_Z = 91.2$ GeV. Since helicity is conserved in the massless limit, there are four combinations of initial and final state fermion helicity configurations which have a nonzero cross section. These are shown in Figure 1.4. The four cross sections

[1] In fact we determine the *effective* weak mixing angle, $\sin^2\theta_W^{\rm eff}$, appropriate at $\sqrt{s} = M_Z$. See section 1.7.

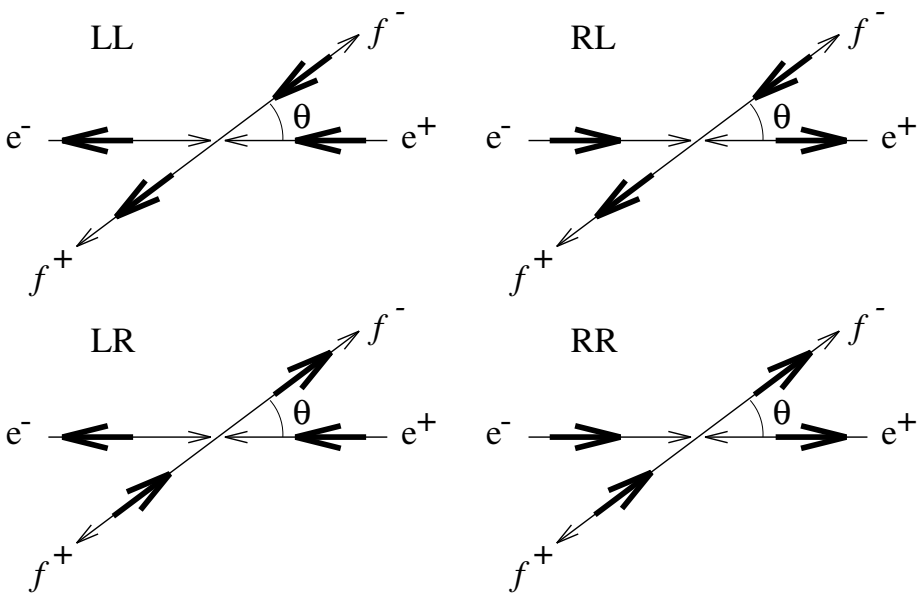

Figure 1.4: Initial and final state fermion spin configurations allowed by helicity conservation. The thin arrows show the particle momenta and the thin arrows indicate the spins.

corresponding to these diagrams can be combined into four linearly independent combinations which correspond to observable quantities.

Clearly we can measure the total cross section for $e^+e^- \to f^+f^-$; this corresponds to a sum of all the pictures,

$$\sigma_{\rm tot} = \sigma_{\rm LL} + \sigma_{\rm RL} + \sigma_{\rm LR} + \sigma_{\rm RR} \tag{1.22}$$

where the cross section corresponding to figure 1.4(LL) is $\sigma_{\rm LL}$, and so forth. The measurement of $\sigma_{\rm tot}$ as a function of $\sqrt{s}$, or Z line shape measurement, has been the subject of intensive study among all the LEP experiments (see for example [10] [53]). Note that since this is a measurement of an absolute cross section, knowledge of the luminosity is required.

Next, we combine the cross sections into $\sigma_F = \sigma_{\rm LL} + \sigma_{\rm RR}$ and $\sigma_B = \sigma_{\rm RL} + \sigma_{\rm LR}$. Notice that σ_F corresponds to a rotation of a spin 1 system through an angle θ, whereas σ_B corresponds to a rotation of a spin 1 system through an angle $\theta + \pi$. σ_F can thus be changed to σ_B by replacing θ with $\theta + \pi$. We therefore interpret σ_F

as the cross section for scattering the f^- into the forward ($\cos\theta > 0$) hemisphere and σ_B as the cross section for scattering the f^- into the backward ($\cos\theta < 0$) hemisphere. The cross section,

$$\sigma_{FB} = \sigma_F - \sigma_B = \sigma_{\rm LL} + \sigma_{\rm RR} - (\sigma_{\rm RL} + \sigma_{\rm LR}) \tag{1.23}$$

is clearly an experimentally measurable quantity. In fact if the asymmetry $\sigma_{FB}/\sigma_{\rm tot}$ is measured, knowledge of the luminosity is not necessary. This is usually called the forward-backward charge asymmetry.

The combinations $\sigma_+ = \sigma_{\rm LL} + \sigma_{\rm RL}$ and $\sigma_- = \sigma_{\rm LR} + \sigma_{\rm RR}$ are the cross sections for producing negative helicity and positive helicity f^- fermions, respectively. The cross section

$$\sigma_{\rm pol} = \sigma_+ - \sigma_- = \sigma_{\rm LL} + \sigma_{\rm RL} - (\sigma_{\rm LR} + \sigma_{\rm RR}) \tag{1.24}$$

can then be used to form $\sigma_{\rm pol}/\sigma_{\rm tot}$, known as the polarization asymmetry.

The remaining combination we call,

$$\sigma_{FB}^{\rm pol} = \sigma_{\rm LL} - \sigma_{\rm RR} - (\sigma_{\rm RL} - \sigma_{\rm LR}) \tag{1.25}$$

Rather than summing the cross sections for events scattered into a given hemisphere, as was done for σ_F and σ_B, we have computed here the difference between the final state fermion polarization asymmetries in the forward and backward hemispheres. The asymmetry $\sigma_{FB}/\sigma_{\rm tot}$ is referred to as the forward-backward polarization asymmetry.

Thus we have combined the four pictures in Figure 1.4 into four linearly independent combinations that correspond to experimentally accessible quantities: a total cross section, a forward-backward charge asymmetry for the final state fermions, and the polarization and forward-backward polarization asymmetries for the final state fermions. The relationship between these quantities and the Z to fermion couplings can be determined with the help of Figure 1.4. For simplicity, we will outline this only for the asymmetries,

In addition to the assumption of massless fermions, the following assumptions greatly simplify the discussion[2],

[2]Both assumptions are perfectly justified for our purposes, since, as described in Chapter 6, the coupling constants are determined in this analysis by first "correcting" the data for the effects of photon exchange, γ-Z interference, and variation in $\sqrt{s}$. A formula which is strictly valid only on the Z pole and for the case of no photon exchange may then be used to determine the couplings from the corrected data. The full expression for the cross section, including photon exchange and γ-Z interference, is given in Appendix A

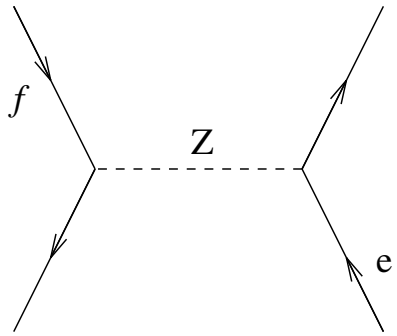

Figure 1.5: The only Feynman diagram contributing to $e^+e^- \to f^+f^-$ for the assumptions given in the text.

- $\sqrt{s} = M_Z$
- photon exchange can be neglected

Further, we will only consider the cases for which the final state fermion is a muon or tau so that the t-channel contribution to the cross section need not be computed. We are then left with one diagram, shown in Figure 1.5. Using the vertex factor in Figure 1.11 gives an amplitude,

$$\mathcal{M} \propto \left[\bar{\psi}^f \gamma^\mu \left(g_V^f - g_A^f \gamma^5\right) \psi^f\right] \left[\bar{\psi}^e \gamma_\mu \left(g_V^e - g_A^e \gamma^5\right) \psi^e\right] \tag{1.26}$$

If we introduce the constants,

$$\begin{aligned} g_R^i &\equiv g_V^i - g_A^i \\ g_L^i &\equiv g_V^i + g_A^i \end{aligned} \tag{1.27}$$

where $i = e, f$, we can rewrite the terms in parenthesis in equation 1.26,

$$g_V^i - g_A^i \gamma^5 = g_R^i \frac{1}{2}\left(1 + \gamma^5\right) + g_L^i \frac{1}{2}\left(1 - \gamma^5\right) \tag{1.28}$$

Now the terms with the g_R^i and g_L^i coefficients project out the right- and left-handed parts of the spinors, so that the amplitude becomes,

$$\mathcal{M} \propto \left[g_R^f \bar{\psi}_R^f \gamma^\mu \psi_R^f + g_L^f \bar{\psi}_L^f \gamma^\mu \psi_L^f\right] \left[g_R^e \bar{\psi}_R^e \gamma_\mu \psi_R^e + g_L^e \bar{\psi}_L^e \gamma_\mu \psi_L^e\right] \tag{1.29}$$

The terms in $\mathcal{M}$, in which only combinations of right- and left-handed fermion states appear, can now be identified with the pictures in Figure 1.4. We can associate an amplitude with each of these pictures by combining the appropriate terms from equation 1.29 with the amplitudes for rotation of a spin-1 system through an angle θ. This is summarized in Table 1.3.

helicity e	helicity f	amplitude	
L	L	$\mathcal{M}_{\mathrm{LL}} \propto g_L^f g_L^{\mathrm{e}} d^1_{11}(\theta)$	$\propto g_L^f g_L^{\mathrm{e}} (1+\cos\theta)$
R	L	$\mathcal{M}_{\mathrm{RL}} \propto g_L^f g_R^{\mathrm{e}} d^1_{11}(\theta+\pi)$	$\propto g_L^f g_R^{\mathrm{e}} (1-\cos\theta)$
L	R	$\mathcal{M}_{\mathrm{LR}} \propto g_R^f g_L^{\mathrm{e}} d^1_{11}(\theta+\pi)$	$\propto g_R^f g_L^{\mathrm{e}} (1-\cos\theta)$
R	R	$\mathcal{M}_{\mathrm{RR}} \propto g_R^f g_R^{\mathrm{e}} d^1_{11}(\theta)$	$\propto g_R^f g_R^{\mathrm{e}} (1+\cos\theta)$

Table 1.3: Amplitudes corresponding to the four spin configurations allowed by helicity conservation in the reaction $\mathrm{e^+e^-} \to f^+f^-$. The d^1_{11} terms are the spin-1 rotation matrices.

The asymmetries discussed previously can be calculated directly from the amplitudes in Table 1.3. The final state fermion polarization, for example, is defined,

$$\mathcal{P}_\tau(\cos\theta) = \frac{d\sigma_R/d(\cos\theta) - d\sigma_L/d(\cos\theta)}{d\sigma_R/d(\cos\theta) + d\sigma_L/d(\cos\theta)} \tag{1.30}$$

where $d\sigma_R/d(\cos\theta)$ and $d\sigma_L/d(cos\theta)$ are the production cross sections for right- and left-handed fermions, respectively. These can be computed from the amplitudes corresponding to the diagrams in Figure 1.4,

$$\begin{aligned} d\sigma_R/d(\cos\theta) &\propto |\mathcal{M}_{\mathrm{RR}}|^2 + |\mathcal{M}_{\mathrm{LR}}|^2 \\ d\sigma_L/d\cos\theta) &\propto |\mathcal{M}_{\mathrm{RL}}|^2 + |\mathcal{M}_{\mathrm{LL}}|^2 \end{aligned} \tag{1.31}$$

Inserting the amplitudes from Table 1.3 into equations 1.31 and using 1.30 and 1.27 yields,

$$\mathcal{P}_f(\cos\theta) = -\frac{\mathcal{A}_f + 2\mathcal{A}_{\mathrm{e}}\cos\theta/(1+\cos^2\theta)}{1 + 2\mathcal{A}_f\mathcal{A}_{\mathrm{e}}\cos\theta/(1+\cos^2\theta)} \tag{1.32}$$

where the polarization factors $\mathcal{A}_f$ and $\mathcal{A}_{\mathrm{e}}$ are defined in terms of the coupling constants,

$$\mathcal{A}_i = \frac{2g_V^i g_A^i}{(g_V^i)^2 + (g_A^i)^2} \tag{1.33}$$

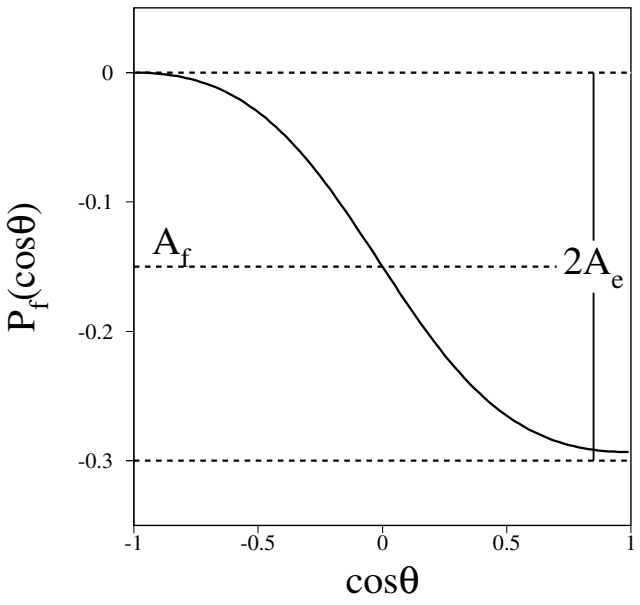

Figure 1.6: $\mathcal{P}_\tau(\cos\theta)$ for $\mathcal{A}_\mathrm{e} = \mathcal{A}_f = 0.15$.

where $i = \mathrm{e}, f$. Thus by measuring the final state fermion polarization as a function of the polar angle, the couplings of both the initial state electrons and final state fermions to the Z can be determined. If we collect a sample of muon or tau pairs from Z decays, for example, then measuring the $\mathcal{P}_f(\cos\theta)$ distribution provides a direct test of the lepton universality hypothesis. The $\mathcal{P}_f(\cos\theta)$ curve is plotted in Figure 1.6.

$\mathcal{P}_f(\cos\theta)$ embodies both σ_pol and σ_{FB}^pol discussed above, but for the sake of comparison we shall determine the polarization and forward-backward polarization asymmetries separately, as well as the forward-backward charge asymmetry. The polarization asymmetry is defined,

$$\mathcal{P}_f = \frac{\sigma_R - \sigma_L}{\sigma_R + \sigma_L} \tag{1.34}$$

where the cross sections can be computed using Figure 1.4 and Table 1.3,

$$\sigma_R \;=\; \int_{-1}^{1} \left(|\mathcal{M}_\mathrm{RR}|^2 + |\mathcal{M}_\mathrm{LR}|^2 \right) d(\cos\theta)$$

$$\sigma_L = \int_{-1}^{1} \left(|\mathcal{M}_{\mathrm{RL}}|^2 + |\mathcal{M}_{\mathrm{LL}}|^2 \right) d(\cos\theta) \tag{1.35}$$

The result is,

$$\mathcal{P}_f = -\frac{2 g_V^f g_A^f}{\left(g_V^f\right)^2 + \left(g_A^f\right)^2} = -\mathcal{A}_f \tag{1.36}$$

The forward-backward polarization asymmetry is defined,

$$\mathcal{P}_f^{FB} = \frac{[\sigma_R(\cos\theta > 0) - \sigma_L(\cos\theta > 0)] - [\sigma_R(\cos\theta < 0) - \sigma_L(\cos\theta < 0)]}{\sigma_{\mathrm{tot}}} \tag{1.37}$$

The cross sections in this expression are computed using equation 1.35 with the range of the integrations over $\cos\theta$ appropriately adjusted. The result is,

$$\mathcal{P}_f^{FB} = -\frac{3}{4}\frac{2 g_V^{\mathrm{e}} g_A^{\mathrm{e}}}{\left(g_V^{\mathrm{e}}\right)^2 + \left(g_A^{\mathrm{e}}\right)^2} = -\frac{3}{4}\mathcal{A}_{\mathrm{e}} \tag{1.38}$$

Interestingly, this cross section is sensitive only to the electron couplings; averaging over the polar angle cancels out the contribution from the final state fermion couplings evident in equation 1.32.

Finally we compute the forward-backward charge asymmetry,

$$\mathcal{A}_{FB} = \frac{\sigma_F - \sigma_B}{\sigma_F + \sigma_B} \tag{1.39}$$

where,

$$\begin{aligned} \sigma_F &= \sigma_R(\cos\theta > 0) + \sigma_L(\cos\theta > 0) \\ \sigma_R &= \sigma_R(\cos\theta < 0) + \sigma_L(\cos\theta < 0) \end{aligned} \tag{1.40}$$

σ_F and σ_B are determined using equations 1.35 with the range on the integration over $\cos\theta$ appropriately adjusted. The result is,

$$\mathcal{A}_{FB} = \frac{3}{4}\frac{2 g_V^f g_A^f}{\left(g_V^f\right)^2 + \left(g_A^f\right)^2}\frac{2 g_V^{\mathrm{e}} g_A^{\mathrm{e}}}{\left(g_V^{\mathrm{e}}\right)^2 + \left(g_A^{\mathrm{e}}\right)^2} = \frac{3}{4}\mathcal{A}_f\mathcal{A}_{\mathrm{e}} \tag{1.41}$$

1.6 τ polarization asymmetries in the Standard Model.

As we shall discuss in Chapter 2, measurement of the τ lepton polarization turns out to be viable from an experimental point of view. Therefore we will now limit the discussion to this asymmetry and apply the results of the previous two sections to evaluate the sensitivity of this measurement to parameters in the SM.

Current experimental results suggest a weak mixing angle[3] $\sin^2\theta_W = 0.2315$ [58]. Thus from equation 1.12 and Table 1.1 we see that $g_V^\ell \ll g_A^\ell$, so that equation 1.36 becomes,

$$\mathcal{P}_\tau \approx -2\frac{g_V^\tau}{g_A^\tau} = -2\left(1 - 4\sin^2\theta_W\right) \tag{1.42}$$

First note that since $\mathcal{P}_\tau$ is approximately linear in the couplings, the relative sign of g_V^τ and g_A^τ can be determined. Furthermore, the factor of eight multiplying $\sin^2\theta_W$ implies that measurement error on $\mathcal{P}_\tau$ translates to an error on $\sin^2\theta_W$ which is a factor of eight smaller. The $\mathcal{P}_\tau^{FB}$ measurement exhibits similar virtues, except that the sensitivity is to $\sin^2\theta_W$ is reduced by a factor 3/4, as evident from equation 1.38.

In contrast, the forward-backward charge asymmetries depend on the product of the electron and final state fermion couplings (equation 1.41), and hence do not reveal the relative sign of g_V and g_A. These asymmetries are also somewhat less sensitive to $\sin^2\theta_W$. Table 1.4 summarizes the sensitivity to $\sin^2\theta_W$ for the three asymmetries as well as the standard model prediction based on $\sin^2\theta_W = 0.2315$.

Asymmetry	Prediction	$\Delta\sin^2\theta_W^{\rm eff}$
$\mathcal{P}_\tau$	0.147	$\frac{1}{8}\Delta\mathcal{P}_\tau$
$\mathcal{P}_\tau^{FB}$	0.110	$\frac{1}{6}\Delta\mathcal{P}_\tau^{FB}$
$\mathcal{A}_{FB}^\ell$	0.016	$\approx \frac{1}{1.7}\Delta\mathcal{A}_{FB}^\ell$

Table 1.4: Standard Model predictions and sensitivities to $\sin^2\theta_W^{\rm eff}$ for various asymmetries with $\sin^2\theta_W^{\rm eff} = 0.2315$. The sensitivity given for $\mathcal{A}_{FB}^\ell$ is approximate as it depends on $\sin^2\theta_W^{\rm eff}$.

[3]This is in fact the *effective* weak mixing angle appropriate for $\sqrt{s} = M_Z$. See section 1.7.

1.7 Radiative corrections and center of mass dependence

We now consider how radiative corrections and variation of the center of mass energy ($\sqrt{s}$) affect the asymmetries. It is convenient to divide the various effects into two categories. We group the $\sqrt{s}$ dependence of the asymmetries and the corrections due to real photon emission (Figure 1.7(a)) into the first category. The second category contains radiative corrections to the vertex (Figure 1.7(b)) and propagator (Figure 1.7(c)).

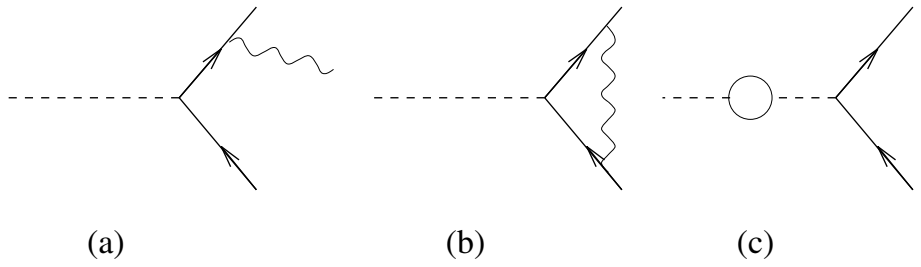

Figure 1.7: Examples of (a) emission of a real photon, (b) a vertex correction, and (c) a propagator correction.

As an example of the dependence of the asymmetries on effects from the first category, we show in Figure 1.8 the τ polarization and forward-backward charge asymmetries as a function of $\sqrt{s}$ with and without initial state radiation (ISR). The monotonic $\sqrt{s}$ dependence in the range[4] $88 < \sqrt{s} < 94$ GeV is a result of γ-Z interference. Note that the slope for $\mathcal{A}_{FB}(\sqrt{s})$ is markedly steeper and opposite in sign to the slope for $\mathcal{P}_\tau(\sqrt{s})$. This can be understood from equations A.2 and A.4, which give the asymmetries including photon exchange and γ-Z interference. For $\mathcal{A}_{FB}$ equations A.2 indicate that the term proportional γ-Z interference is multiplied by only axial-vector coupling constants. For $\mathcal{P}_\tau$, on the other hand, the γ-Z term is multiplied by a vector coupling constant, which for charged leptons is more than an order of magnitude smaller than than the axial-vector coupling. Thus the effect of the interference term is suppressed in the case of $\mathcal{P}_\tau$. Note also that equations A.2 and A.4 indicate that the slopes are opposite for $\mathcal{P}_\tau$ and $\mathcal{A}_{FB}$,

[4] A LEP scan of the Z resonance typically covers the range from 88 GeV to 94 GeV.

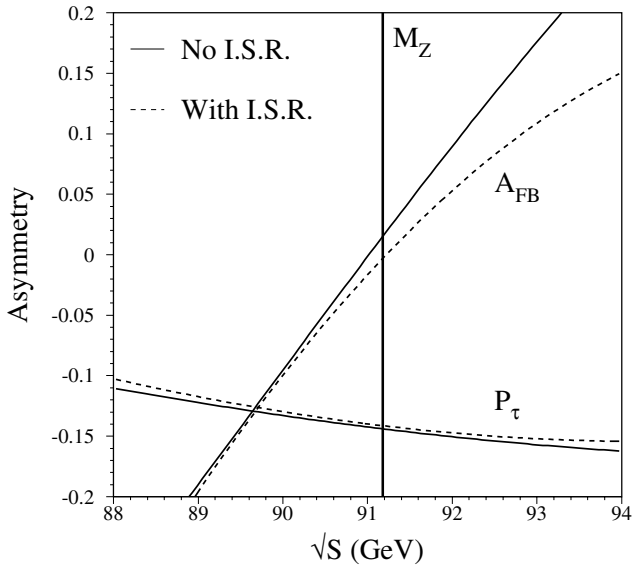

Figure 1.8: $\mathcal{P}_\tau$ and A_{FB} as a function of $\sqrt{s}$ with and without initial state radiation (I.S.R.). The curves were calculated using the program ZFITTER [45].

as reflected in Figure 1.8. Since initial state radiation shifts the Z resonance peak, and since $\mathcal{A}_{FB}$ depends more strongly on $\sqrt{s}$ than does $\mathcal{P}_\tau$, the effect of ISR is correspondingly larger for $\mathcal{A}_{FB}$ than for $\mathcal{P}_\tau$. These effects are generally uninteresting and are corrected during the fitting procedure, as described in section 6.3.1.

The treatment of corrections from the second category is more subtle; beyond the lowest order relations described in section 1.2 there is some ambiguity in the use of $\sin^2\theta_W$ [54]. We shall *define* the effective weak mixing angle, $\sin^2\theta_W^{\rm eff}$, in terms of the vector- and axial-vector coupling constants measured at $\sqrt{s} = M_Z$,

$$1 - 4\sin^2\theta_W^{\rm eff} \equiv \frac{g_V^\ell}{g_A^\ell} \tag{1.43}$$

Corrections to the propagator are then absorbed into this parameter. As discussed in section 1.4, these corrections are of particular interest as they are sensitive to physics at mass scales above M_Z via the appearance of loops containing particles too heavy to be directly produced.

Chapter 2

Experimental Method

The polarization of final state fermions produced in the reaction $e^+e^- \to Z \to f^+f^-$ is not generally an experimentally accessible quantity for a collider detector. Several features of τ lepton decays, however, make possible the high precision measurement of the final state polarization of τ leptons.

First, the τ is a sequential lepton (see Table 1.1) so its decay is maximally parity violating [29]. In the τ rest frame, parity violation determines the angular distribution of the τ decay products with respect to the τ helicity. When boosted into the lab frame, this angular distribution is manifest in the form of the energy and angular distribution of the decay products, which can be measured. Thus the energy and angular distributions of τ decay products is a τ polarimeter.

Second, the mean τ decay length at $\sqrt{s} = M_Z$ is $\gamma\beta c\tau_\tau \approx 2.3$ mm, ensuring that τ decays are easily contained within a particle detector. In contrast, muons produced in $Z \to \mu^+\mu^-$ decays are penetrating and travel an average of about 300 km. Electrons are stable so their polarization cannot be determined via energy measurement of the final state.

Finally, the low multiplicity and simple kinematics of its decay modes make the τ an attractive candidate for extracting the polarization. In principle, every τ decay channel carries some polarization information in the energy and angular distributions of its decay products, but in practice the non-resonant decays with many hadrons in the final state have low sensitivity to the polarization and are difficult to fully reconstruct, so they have not been included in this analysis. Table 2.1 summarizes the decay channels used for the polarization measurement presented here [30]; they include 83% of all τ decays.

It is important to keep in mind that the quantities $\mathcal{P}_\tau$ and $\mathcal{P}_\tau(\cos\theta)$ described

in Chapter 1 are defined in terms of the $\tau - \mathrm{Z}$ and $\mathrm{e} - \mathrm{Z}$ couplings (equation 1.32). However if the τ decay spectrum is employed as a polarization analyzer, then the structure of the $\tau - \mathrm{W}$ coupling comes into play, and what is in fact measured is $\xi\mathcal{P}_\tau$, where ξ is the chirality parameter, or alternatively the average ν_τ polarization. Assuming only V and A couplings of the W to the τ,

$$\xi = \frac{2g_V^{\mathrm{CC}} g_A^{\mathrm{CC}}}{(g_V^{\mathrm{CC}})^2 + (g_A^{\mathrm{CC}})^2} \tag{2.1}$$

where g_V^{CC} and g_A^{CC} are the vector and axial vector charged current couplings. If we assume the maximally parity violating $V-A$ structure of the $\tau-\mathrm{W}$ coupling, then $\xi = -1$ and the quantity measured by analysis of the τ decay spectra is just $\mathcal{P}_\tau$. In this analysis the $V-A$ hypothesis is assumed, consistent with current experimental evidence [17] [18]. We note that such an assumption is required as long as all τ decays in the sample are treated independently. However, the correlation between the decay distributions for τ's produced in a $\mathrm{Z} \to \tau^+\tau^-$ event is sensitive to the structure of both the charged and neutral weak currents [18].

Assuming only V and A couplings of the weak neutral current to the τ ensures helicity conservation in the high energy limit, so that the τ^+ and τ^- produced by the Z have opposite helicities. This approximation is good to $\mathcal{O}(m_\tau^2/m_Z^2)$. Since the two τ's have opposite helicity and opposite charge, their decay distributions are the same [16]. This follows from CP conservation. Therefore we define $\mathcal{P}_\tau \equiv \mathcal{P}_{\tau^-} = -\mathcal{P}_{\tau^+}$ so that the decay distribution for a given $\mathcal{P}_\tau$ does not depend on the τ charge.

Channel	Spin	Branching Ratio
$\pi^-\nu_\tau$	0	0.12
$\mathrm{K}^-\nu_\tau$	0	0.01
$\mathrm{e}^-\bar{\nu}_\mathrm{e}\nu_\tau$	1/2	0.18
$\mu^-\bar{\nu}_\mu\nu_\tau$	1/2	0.18
$\rho^-\nu_\tau \to \pi^-\pi^0$	1	0.24
$a_1^-\nu_\tau \to \pi^-\pi^0\pi^0$	1	0.10

Table 2.1: τ decay channels used to measure the polarization. The column labeled "spin" gives the spin of the τ daughter.

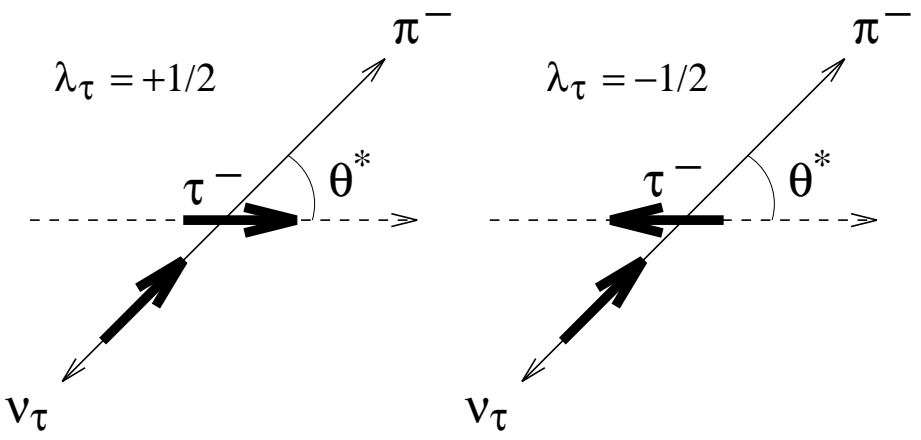

Figure 2.1: Definition of the angle θ^* in the decay $\tau^- \to \pi^-\nu_\tau$. The dashed line is the axis defined by the τ flight direction, and the thick arrows indicate the helicity of the $J = 1/2$ particles. The amplitude $\mathcal{M}_+$ defined in the text corresponds to the $\lambda_\tau = +1/2$ picture; $\mathcal{M}_-$ corresponds to $\lambda_\tau = -1/2$.

Below we describe the decay distribution for each τ decay channel used in this polarization analysis, as well as the sensitivity to polarization that characterizes each distribution. A short summary of important systematic errors in included at the end[1].

2.1 Polarization in $\tau^- \to \pi^-\nu_\tau$ and $\tau^- \to \mathrm{K}^-\nu_\tau$

In the $\tau^- \to \pi^-(\mathrm{K}^-)\nu_\tau$ channel, the τ decays to a single spin-0 particle and a neutrino, so the kinematics is simple; the π^- or K^- is monoenergetic in the τ rest frame and all of the angular momentum is carried off by the neutrino. Since these channels are the simplest, and since they exhibit the highest sensitivity to $\mathcal{P}_\tau$, it is worthwhile to briefly outline how we arrive at the relation between the τ polarization and the π^- (or K^-) energy spectrum.

First consider the π^- channel[2]. We can use the fact that the neutrino is left-

[1] A quantitative summary of systematic errors relevant to the measurements discussed here is given in Chapter 6.

[2] Here and throughout this Chapter, the effects of radiative corrections are neglected. Radiative corrections are discussed in Chapter 1 and a correction for their effects is described in

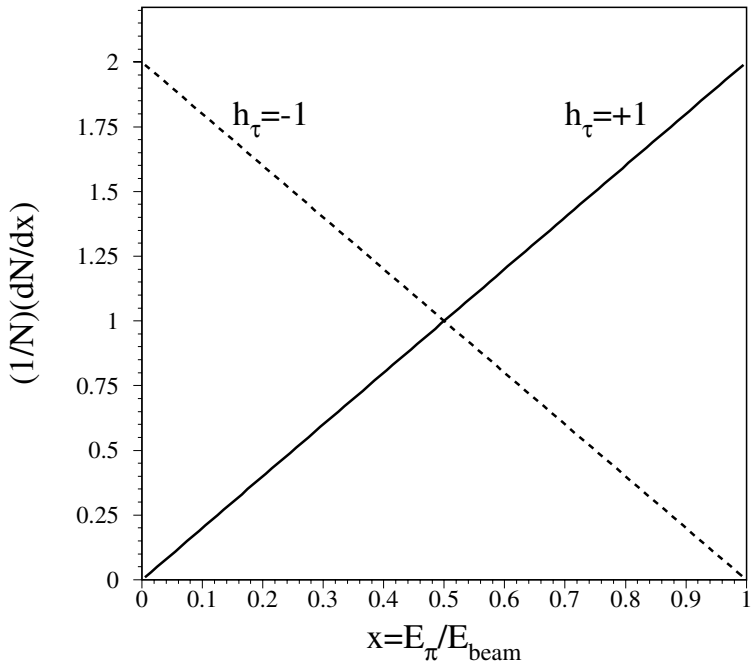

Figure 2.2: Energy distribution in the $\tau^- \to \pi^-\nu_\tau$ channel for $h_\tau = +1$ and $h_\tau = -1$. For the τ^-, the $h_\tau = +1$ spectrum corresponds to helicity $\lambda_\tau = +1/2$ and likewise the $h_\tau = -1$ spectrum corresponds to $\lambda_\tau = +1/2$.

handed together with conservation of angular momentum to write the decay amplitudes for positive and negative helicity taus; each amplitude is proportional to the quantum mechanical rotation of a spin-1/2 system:

$$\begin{aligned} \mathcal{M}_{\lambda_\tau=+1/2} \equiv \mathcal{M}_+ &\propto d^{1/2}_{1/2,1/2}(\theta^*) = \cos(\theta^*/2) \\ \mathcal{M}_{\lambda_\tau=-1/2} \equiv \mathcal{M}_- &\propto d^{1/2}_{1/2,1/2}(\pi - \theta^*) = \sin(\theta^*/2) \end{aligned} \tag{2.2}$$

where θ^* is the angle in the τ rest frame between the π^- flight direction and the axis defined by the τ flight direction, as shown in Figure 2.1, and the $d^{1/2}_{1/2,1/2}$ are the spin-1/2 rotation matrices. For τ's produced with polarization $\mathcal{P}_\tau$, the angular

Chapter 6.

distribution of the π^-'s in the τ rest frame is then,

$$\frac{dN}{d(\cos\theta^*)} \propto \frac{1+\mathcal{P}_\tau}{2} \mid \mathcal{M}_+ \mid^2 + \frac{1-\mathcal{P}_\tau}{2} \mid \mathcal{M}_- \mid^2 \tag{2.3}$$

The angle θ^* can be expressed in terms of the lab frame π^- energy,

$$\cos\theta^* = \frac{2x - m_\pi^2/m_\tau^2 - 1}{(1 - m_\pi^2/m_\tau^2)(1 - m_\tau^2/E_{\rm beam}^2)^{1/2}} \tag{2.4}$$

where $x = E_\pi / E_{\rm beam}$. The approximations $m_\tau / E_{\rm beam} \ll 1$ and $m_\pi / m_\tau \ll 1$ can be used to simplify equation 2.4,

$$\cos\theta^* \approx 2x - 1 \tag{2.5}$$

Combining equations 2.3 and 2.5 and multiplying by the appropriate normalization, yields the decay energy distribution,

$$\frac{1}{N}\frac{dN}{dx} \approx 1 + \mathcal{P}_\tau (2x - 1) \tag{2.6}$$

This distribution is shown in Figure 2.2 for $h_\tau = +1$ and $h_\tau = -1$, where we define $h_\tau = 2q\lambda_\tau$, q being the τ charge. This symbol is employed in lieu of $\mathcal{P}_\tau$ since $\mathcal{P}_\tau$ is normally associated with an ensemble of τ's of both helicities. The observed τ polarization should then be a linear combination of the $h_\tau = +1$ and $h_\tau = -1$ distributions.

In the case of $\tau^- \to K^- \nu_\tau$, the decay energy spectrum does not reach $E_K = 0$, but cuts off at $E_K / E_{\rm beam} = m_K^2 / m_\tau^2 \approx 0.08$. This is apparent from the kinematical limits imposed by equation 2.4.

2.2 Polarization in $\tau^- \to e^- \bar{\nu}_e \nu_\tau$ and $\tau^- \to \mu^- \bar{\nu}_\mu \nu_\tau$

These channels are three-body decays with two undetected neutrinos; the only observed particle is the e^- or μ^- which is not monoenergetic in the τ rest frame, and all three final-state particles carry angular momentum. Despite these complications, the e^- and μ^- energy spectra are still sensitive to the τ polarization. It is possible to see that there is at least some sensitivity by considering the cases in which the e^- or μ^- has maximal energy in the τ rest frame [16]. In these cases the neutrinos are emitted in the same direction, opposite to that of the charged

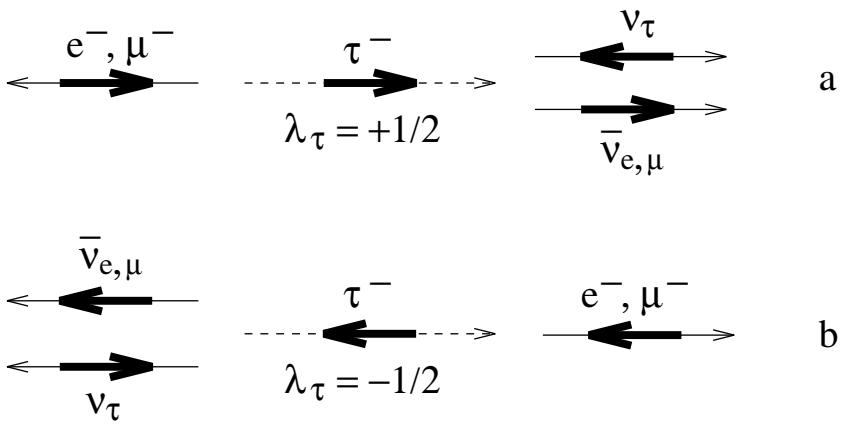

Figure 2.3: Favored spin and momentum configurations in $\tau^- \to e^- \bar{\nu}_e \nu_\tau$ and $\tau^- \to \mu^- \bar{\nu}_\mu \nu_\tau$ for the case in which the charged lepton has maximal energy in the τ rest frame. The dashed line is the axis defined by the τ flight direction, and the thick arrows indicate the spins.

lepton, as shown in Figure 2.3. Let the flight direction of the charged lepton define the z-axis. In the cases shown in the figure, there is no orbital angular momentum component along the z-axis, and the z-components of the neutrino spins sum to zero. So for $\lambda_\tau = +1/2$, conservation of the z-component of angular momentum and the fact that the e^- or μ^- is left-handed favor the configuration shown in Figure 2.3a, in which the charged lepton is emitted in the direction opposite to the flight direction of the τ. On the other hand, for $\lambda_\tau = -1/2$ the most favored configuration has the charged lepton emitted along the τ flight direction, as shown in Figure 2.3b. So in the lab frame, the energy of the charged lepton is greater for the $\lambda_\tau = -1/2$ case than for the case $\lambda_\tau = +1/2$, thus indicating it is possible to distinguish the two τ helicities based on the energy spectrum of the e^- or μ^-.

The analytic form of the energy distribution for the two leptonic channels is,

$$\frac{1}{N}\frac{dN}{dx} = \frac{1}{3}\left[(5 - 9x^2 + 4x^3) + \mathcal{P}_\tau(1 - 9x^2 + 8x^3)\right] \tag{2.7}$$

where $x = E_{e,\mu}/E_{\rm beam}$. Figure 2.4 shows the energy distributions for $h_\tau = +1$ and $h_\tau = -1$ electrons and muons. Notice that the $h_\tau = -1$ distribution has higher average energy than the $h_\tau = +1$ distribution, as expected from the arguments

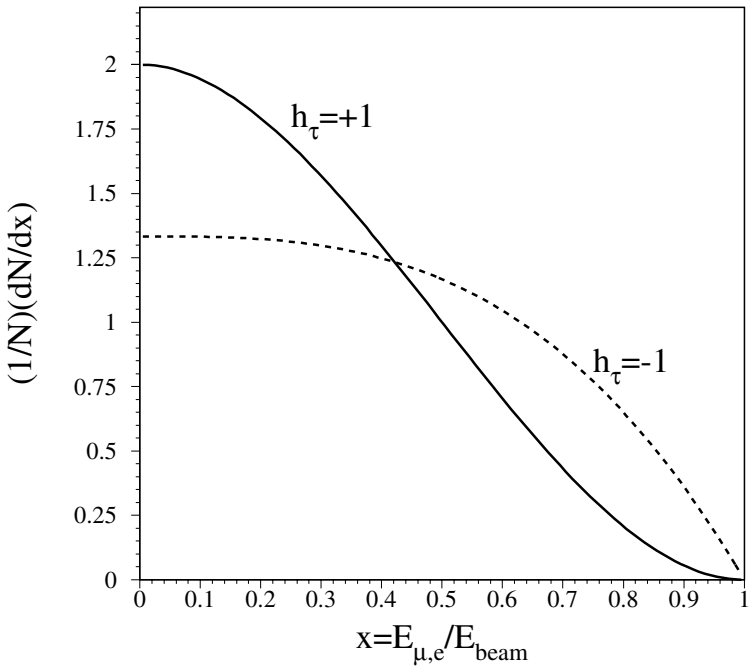

Figure 2.4: Energy distribution in the $\tau^- \to e^- \bar{\nu}_e \nu_\tau$ and $\tau^- \to \mu^- \bar{\nu}_\mu \nu_\tau$ channels for $h_\tau = +1$ and $h_\tau = -1$.

above.

2.3 Polarization in $\tau^- \to \rho^- \nu_\tau$

The $\tau^- \to \rho^- \nu_\tau$ channel offers the kinematic simplicity of a two-body decay, like the $\tau^- \to \pi^- \nu_\tau$ channel, but the dynamics is more complicated since the ρ is a vector particle and can therefore find itself with one of three possible helicities.

Figure 2.5 illustrates the main points. Conservation of angular momentum allows the ρ to have $\lambda_\rho = 0$ or $\lambda_\rho = -1$. The amplitudes A_0 and A_1 for these two helicities are related by [11],

$$\frac{|A_0|}{|A_1|} = \frac{\sqrt{2} m_\rho}{m_\tau} \tag{2.8}$$

This equation says that the $\lambda_\rho = 0$ state is accessible since the ρ is massive.

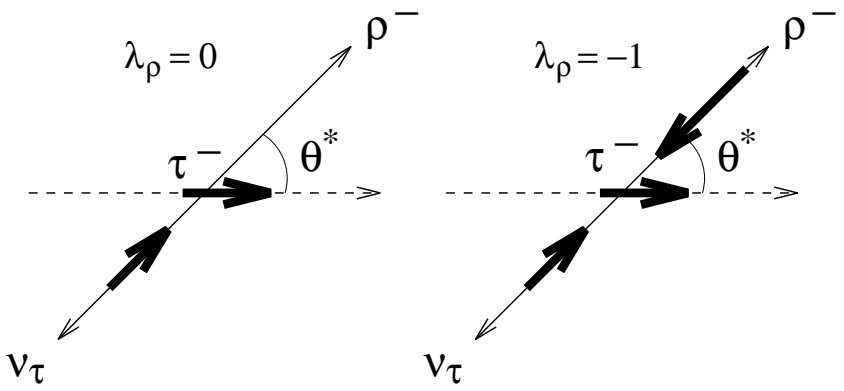

Figure 2.5: Definition of the angle θ^* in the decay $\tau^- \to \rho^- \nu_\tau$. The dashed line is the axis defined by the τ flight direction and the thick arrows indicate particle helicities. Note that there are two possible helicities for the ρ. The amplitudes corresponding to these pictures are given in the text.

Combining the helicity amplitudes with the θ^*-dependent amplitudes for all the possible configurations of ρ and τ helicities, we get

$$\begin{aligned}
\lambda_\rho = 0, \lambda_\tau = +1/2: \quad & \mathcal{M}^0_+ = A_0 d^{1/2}_{1/2,1/2}(\theta^*) && = A_0(1+\cos\theta^*) \\
\lambda_\rho = -1, \lambda_\tau = +1/2: \quad & \mathcal{M}^1_+ = A_1 d^{1/2}_{1/2,1/2}(\pi-\theta^*) && = A_1(1-\cos\theta^*) \\
\lambda_\rho = 0, \lambda_\tau = -1/2: \quad & \mathcal{M}^0_- = A_0 d^{1/2}_{1/2,1/2}(\pi-\theta^*) && = A_0(1-\cos\theta^*) \\
\lambda_\rho = -1, \lambda_\tau = -1/2: \quad & \mathcal{M}^1_- = A_1 d^{1/2}_{1/2,1/2}(\theta^*) && = A_1(1+\cos\theta^*)
\end{aligned} \tag{2.9}$$

From these we obtain the decay angular distribution,

$$\begin{aligned}
\frac{1}{N}\frac{dN}{d\cos\theta^*} &= \frac{1+\mathcal{P}_\tau}{2}\left[|\mathcal{M}^0_+|^2 + |\mathcal{M}^1_+|^2\right] \\
&+ \frac{1-\mathcal{P}_\tau}{2}\left[|\mathcal{M}^0_-|^2 + |\mathcal{M}^1_-|^2\right] \\
&= [1+\alpha\mathcal{P}_\tau\cos\theta^*]
\end{aligned} \tag{2.10}$$

where the factor $\alpha = \frac{|A_0|^2-|A_1|^2}{|A_0|^2+|A_1|^2} \approx 0.46$ is a direct result of the two possible helicity states of the ρ for each τ helicity. This factor represents our ignorance of λ_ρ, and so reduces sensitivity to the polarization, as explained in detail in section 2.5.

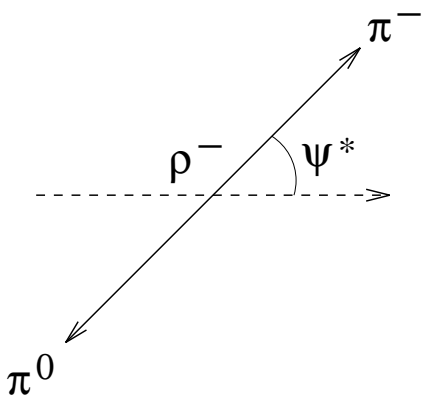

Figure 2.6: Definition of the angle ψ^*.

Loss of sensitivity due to α can be compensated by analyzing the subsequent decay $\rho^- \to \pi^-\pi^0$, whose energy and angular distributions depend on the ρ helicity, λ_ρ [11], and thus can be used to separate contributions from A_0 and A_1 to equation 2.10. In particular we can measure the quantity ψ^* which is the angle in the ρ rest frame between the axis defined by the ρ^- flight direction and the π^- flight direction. This is shown in Figure 2.6. Figure 2.7 shows the $h_\tau = +1$ and $h_\tau = -1$ decay distributions for $\tau^- \to \rho^-\nu_\tau$ as a function of the parameters $\cos\theta^*$ and $\cos\psi^*$. From these pictures it is evident that there is polarization information contained not only in $\cos\theta^*$ but in $\cos\psi^*$ as well.

In terms of directly measurable energies and angles, $\cos\theta^*$ and $\cos\psi^*$ are given by [14],

$$\cos\theta^* = \frac{4m_\tau^2}{m_\tau^2 - m_\rho^2}\frac{E_{\pi^0} + E_{\pi^-}}{E_{\rm beam}} - \frac{m_\tau^2 + m_\rho^2}{m_\tau^2 - m_\rho^2} \tag{2.11}$$

and,

$$\cos\psi^* = \frac{m_\rho}{\sqrt{m_\rho^2 - 4m_\pi^2}}\frac{E_{\pi^-} - E_{\pi^0}}{|\vec{P}_{\pi^-} + \vec{P}_{\pi^0}|} \tag{2.12}$$

Notice that equation 2.11 expresses the simple relation $\cos\theta^* \sim E_\rho/E_{\rm beam}$, which is exactly what we expect by analogy with the $\tau^- \to \pi^-\nu_\tau$ channel and equation 2.5. Equation 2.12 contains the relation $\cos\psi^* \sim (E_{\pi^-} - E_{\pi^0})/E_\rho$, which can be understood from Figure 2.6. For example, if $\cos\psi^* = 0$ then in the ρ rest frame the pions are emitted perpendicular to the ρ flight direction and will

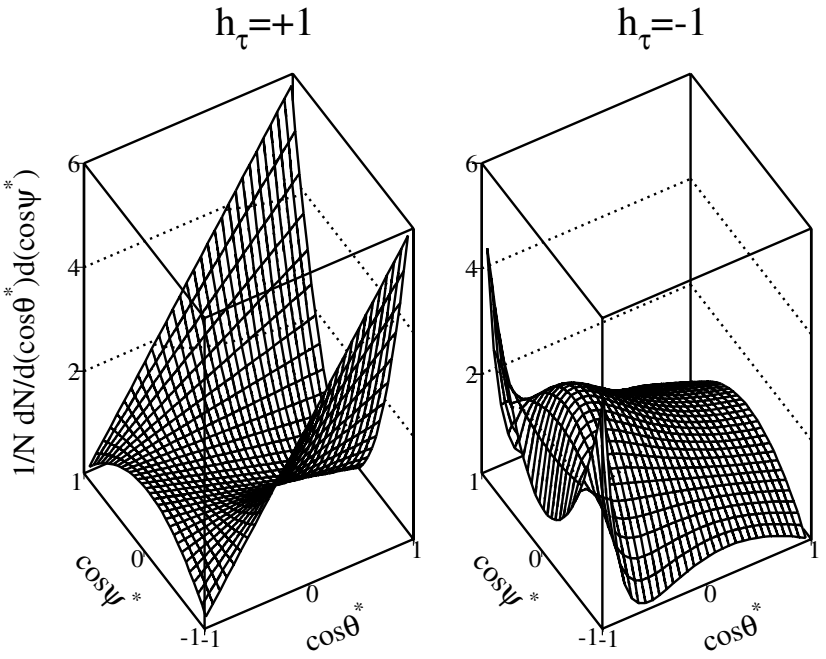

Figure 2.7: Distribution of $\cos\theta^*$ and $\cos\psi^*$ for $h_\tau = +1$ and $h_\tau = -1$.

therefore have equivalent energies in the lab frame. This is most likely for the case $\lambda_\rho = -1$. On the other hand, if $\cos\psi^* = 1$, then the π^- is emitted along the ρ flight direction, while the π^0 is emitted opposite to the ρ flight direction, so that in the lab frame $E_{\pi^-} > E_{\pi^0}$. This distribution is most likely if $\lambda_\rho = 0$.

2.4 Polarization in $\tau^- \to a_1^- \nu_\tau$

The a_1 is a pseudovector meson, so this decay channel is similar to $\tau^- \to \rho^- \nu_\tau$. The dilution factor α is larger, however, since $m_{a_1} = 1.26$ GeV, nearly the mass of the τ. Furthermore, the a_1 decays via $a_1 \to \pi^-\pi^-\pi^+$ and $a_1 \to \pi^-\pi^0\pi^0$, so the polarization sensitive observables are different. Maximum sensitivity is achieved through the use of three angles and three invariant masses taken between pairs of final state pions [31]. The angle θ^* is defined in the same way as for all the other channels. An angle β is defined as the angle in the a_1 rest frame between the normal to the 3-π decay plane and the a_1 flight direction; this is analogous to

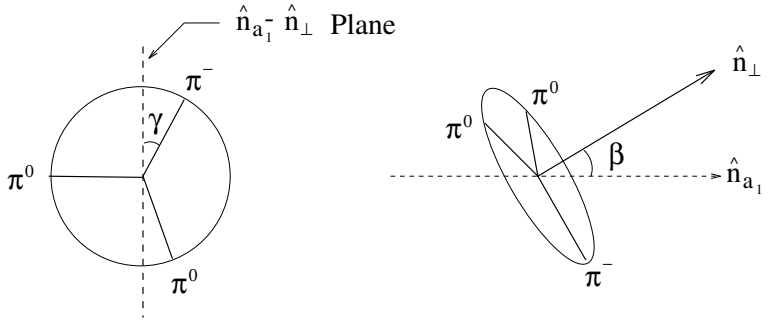

Figure 2.8: The angles β and γ used in determining the polarization in the $\tau^- \to a_1^- \nu_\tau$ channel. $\hat{n}_\tau$ is the vector defined by the τ flight direction, and $\hat{n}_\perp$ is the vector normal to the $3-\pi$ decay plane.

ψ^* of the $\tau^- \to \rho^- \nu_\tau$ channel. A third angle γ corresponds to a rotation around the normal to the 3-π decay plane, and characterizes the orientation of the pions in the 3-π plane. These angles are shown in Figure 2.8.

Incorporating all of these observables yields an ideal sensitivity twice as high as for the $\tau^- \to e^- \bar{\nu}_e \nu_\tau$ or $\tau^- \to \mu^- \bar{\nu}_\mu \nu_\tau$ channel. However, the relationship between these parameters and the τ polarization depends on the form of the hadronic structure functions, so there is a model dependence and corresponding theoretical uncertainty associated with the analysis in this channel. The associated systematic error on the polarization measurement is given in section 6.2.5

2.5 Sensitivities

The different sets of observables associated with the τ decay channels described above offer different sensitivities to the τ polarization. We have seen for example that the $\tau^- \to e^- \bar{\nu}_e \nu_\tau$ and $\tau^- \to \mu^- \bar{\nu}_\mu \nu_\tau$ channels are less sensitive than $\tau^- \to \pi^- \nu_\tau$ on account of the two undetected neutrinos in the leptonic channels. The sensitivity can be quantified by considering how the form of the distribution of decay observables contributes to the statistical error of the polarization measurement.

Ignoring for the moment that the decay spectra for the two τ's produced in a Z decay are correlated, the overall statistical error can be written in terms of the

errors for the i channels analyzed,

$$\sigma^2 = \left[\sum_{i=1}^{N_{\text{channels}}} \frac{1}{\sigma_i^2} \right]^{-1} \tag{2.13}$$

The terms on the right of equation 2.13 are the statistical weights for each channel. We define the sensitivity in terms of these weights,

$$S_i^2 = \frac{1}{N_i \sigma_i^2} \tag{2.14}$$

where N_i is the number of τ decays analyzed for the i'th channel, and S_i is the sensitivity. Notice that the N_i of on the right of equation 2.14 cancel the $1/\sqrt{N_i}$ dependence of the statistical error, so that S_i does not depend on the amount of data. The sensitivities can be written in terms of the branching ratios,

$$S_i^2 = \frac{1}{N B_i \sigma_i^2} \tag{2.15}$$

where N is the total number of events from all channels an B_i is the branching ratio for the i'th channel.

In practice, the σ_i's in equations 2.14 and 2.15 are the statistical errors associated with a some kind of fit to the measured energy and angular distributions of the τ decay products, so a sensible way to quantify the sensitivity is to compute the error that results from a fit to the ideal distributions. We consider the case of an unbinned maximum likelihood fit, for which the goal is to maximize the likelihood function,

$$\mathcal{L} = \prod_j \mathcal{W}(\vec{\eta_j}; \mathcal{P}_\tau) \tag{2.16}$$

where $\mathcal{W}$ is the normalized probability density for a given decay j to have the decay observables $\vec{\eta_j}$. Alternatively we can maximize $\ln \mathcal{L}$.

For a given channel, the probability density $\mathcal{W}$ can be written in terms of a piece that depends on the polarization and a piece that does not [11]:

$$\mathcal{W} = f_0(\vec{\eta}) + \mathcal{P}_\tau f_1(\vec{\eta}) \tag{2.17}$$

with $\int f_0(\vec{\eta}) d\vec{\eta} = 1$ and $\int f_1(\vec{\eta}) d\vec{\eta} = 0$ as normalization and positivity conditions. The linearity in $\mathcal{P}_\tau$ evident in equation 2.17 stems from the fact that a given decay originates from a τ with either $h_\tau = +1$ or $h_\tau = -1$, and so the decay distribution

$\mathcal{W}$ for an ensemble of τ's is a linear combination of the $h_\tau = +1$ and $h_\tau = -1$ distributions. We can now write the log-likelihood function,

$$\ln \mathcal{L} = \sum_{j=1}^{N} \ln \left[f_0(\vec{\eta_j}) + \mathcal{P}_\tau f_1(\vec{\eta_j}) \right] \tag{2.18}$$

and maximize it,

$$0 = \frac{\partial \ln \mathcal{L}}{\partial \mathcal{P}_\tau} = \sum_{j=1}^{N} \frac{f_1(\vec{\eta_j})}{f_0(\vec{\eta_j}) + \mathcal{P}_\tau f_1(\vec{\eta_j})} \tag{2.19}$$

Solving equation 2.19 gives $\hat{\mathcal{P}}_\tau$, an estimator of $\mathcal{P}_\tau$. The error on $\hat{\mathcal{P}}_\tau$ is,

$$\frac{1}{\sigma^2} = -\frac{\partial^2 \ln \mathcal{L}}{\partial \mathcal{P}_\tau^2}\bigg|_{\hat{\mathcal{P}}_\tau} = \sum_{j=1}^{N} \frac{f_1^2(\vec{\eta_j})}{[f_0(\vec{\eta_j}) + \hat{\mathcal{P}}_\tau f_1(\vec{\eta_j})]^2} \tag{2.20}$$

In the limit of large N this becomes,

$$\frac{1}{\sigma^2} = N \int \frac{f_1^2(\vec{\eta})}{[f_0(\vec{\eta}) + \hat{\mathcal{P}}_\tau f_1(\vec{\eta})]^2} \mathcal{W} d\vec{\eta} \tag{2.21}$$

where the probability density, $\mathcal{W}$, is from equation 2.17. Using equation 2.14, we arrive at the expression for sensitivity in terms of the distribution of decay observables:

$$S^2 = \int \frac{f_1^2(\vec{\eta})}{f_0(\vec{\eta}) + \hat{\mathcal{P}}_\tau f_1(\vec{\eta})} d\vec{\eta} \tag{2.22}$$

As an example, consider the case of the two-body τ decays. Here, $f_0 = 1$ and $f_1 = \alpha(2x-1)$, where $x = E_\pi / E_{\rm beam}$, and α is the factor defined in equation 2.10. Using equation 2.22 we find,

$$\begin{aligned} S^2 &= \mathcal{N} \int_a^1 \frac{\alpha^2 (2x-1)^2}{1 + \alpha \mathcal{P}_\tau (2x-1)} dx \\ &= \frac{\mathcal{N}\alpha^2}{2} \left[\left(\frac{1-b^3}{3} \right) - \left(\frac{1 - b^4 \alpha \mathcal{P}_\tau}{4} \right) + \left(\frac{1 - b^5 (\alpha \mathcal{P}_\tau)^2}{5} \right) - \ldots \right] \end{aligned} \tag{2.23}$$

where a is the energy at which the spectrum cuts off, $b = 2a - 1$, and the factor $\mathcal{N} = [1 - a(1 + a\mathcal{P}_\tau \alpha - \mathcal{P}_\tau \alpha)]^{-1}$ ensures that the probability density $\mathcal{W}$ of equation 2.17 is normalized over the range $a \leq x \leq 1$.

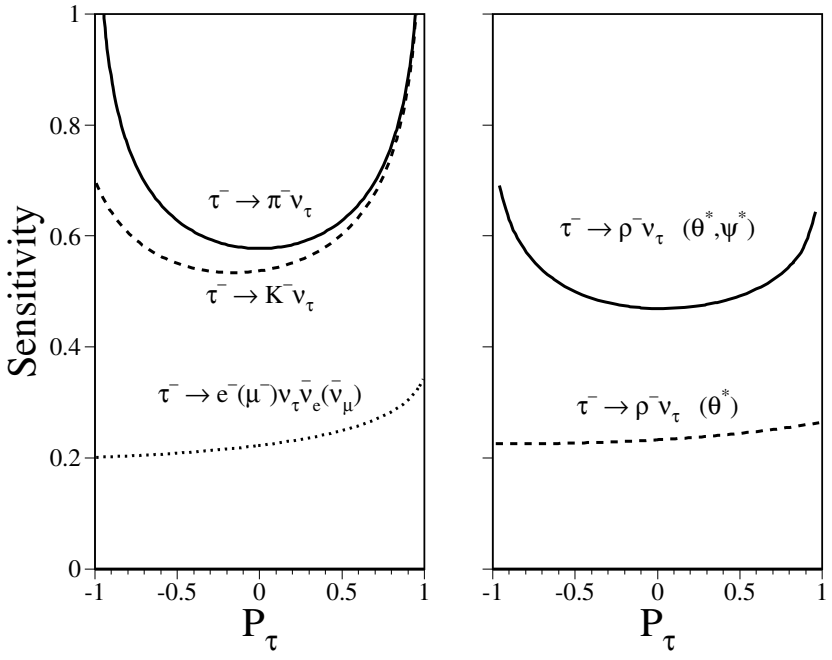

Figure 2.9: Sensitivity as a function of $\mathcal{P}_\tau$ for various decay channels. The sensitivity for the ρ^- channel is shown for the case in which only $\cos\theta^*$ is used and for the case in which both $\cos\theta^*$ and $\cos\psi^*$ are used.

The sensitivities derived from equation 2.23 for the $\tau^- \to \pi^-\nu_\tau$, $\tau^- \to K^-\nu_\tau$, and $\tau^- \to \rho^-\nu_\tau$ channels are shown in Figure 2.9. Notice the reduction in sensitivity of $\tau^- \to K^-\nu_\tau$ compared to $\tau^- \to \pi^-\nu_\tau$; this is due to the kinematic cutoff in the K^- spectrum described in section 2.1. The cutoff enters equation 2.23 through a. In the $\tau^- \to \rho^-\nu_\tau$ channel there is a substantial reduction in sensitivity compared to $\tau^- \to \pi^-\nu_\tau$ if only $\cos\theta^* \propto E_\rho$ is used to infer the polarization. Most of the reduction in sensitivity is a consequence of α, though there is a non-negligible effect of the cutoff, a. As we have seen, however, inclusion of the parameter ψ^* in the analysis of this channel compensates for the effect of α. This is shown in Figure 2.9, where the sensitivity curve in this case is derived in the same way as equation 2.23 except that the integration is carried out over the two angles θ^* and ψ^* using the distribution $\mathcal{W}(\theta^*, \psi^*)$ appropriate to the ρ [11]. Also shown in Figure 2.9 is the sensitivity for the leptonic channels. For this case, $\mathcal{W}$ can be read

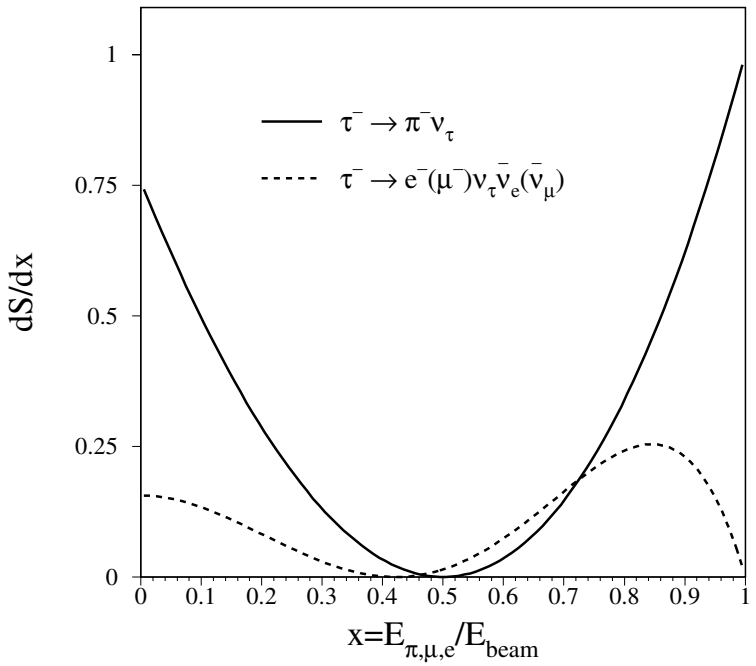

Figure 2.10: Sensitivity as a function of energy for the channels $\tau^- \to \pi^- \nu_\tau$, $\tau^- \to e^- \bar{\nu}_e \nu_\tau$ and $\tau^- \to \mu^- \bar{\nu}_\mu \nu_\tau$.

directly from equation 2.7.

The polarization sensitivity in a given channel is not the same for all regions of the polarization sensitive variables. In the case of $\tau^- \to \pi^- \nu_\tau$, for example, entries in the extreme high energy end of the spectrum ($x = 1$) come almost exclusively from decays of $\lambda_\tau = +1/2$ τ's. This is clear from Figures 2.1 and 2.2. Similarly, the $x = 0$ end is dominated by τ decays in which $\lambda_\tau = -1/2$. In contrast, the central region of the spectrum contains contributions from both helicity states. For example if $x = 1/2$ then $\theta^* = \pi/2$ (equation 2.5), and from equations 2.2 we see that the decay amplitudes for $\lambda_\tau = +1/2$ and $\lambda_\tau = -1/2$ are then the same. Thus there is no polarization sensitivity at $x = 1/2$. This effect is shown quantitatively in Figure 2.10, in which the sensitivity is computed as a function of energy according to equation 2.22. The analogous plot for the $\tau^- \to \rho^- \nu_\tau$ channel is shown in Figure 2.11. It is clearly important to exercise special care in analyzing the data that fall in the regions of highest sensitivity.

Table 2.2 summarizes the sensitivities and weights for each channel analyzed.

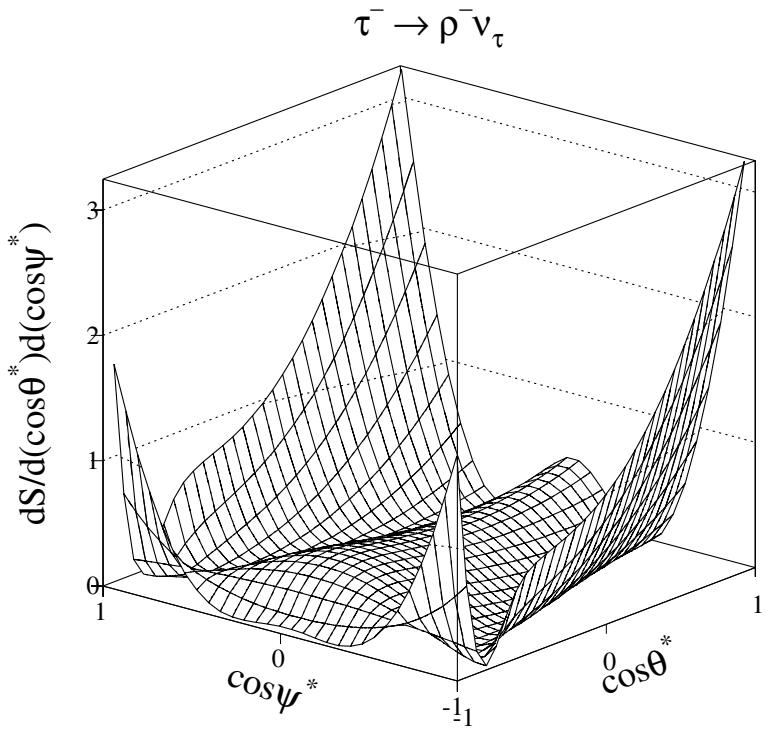

Figure 2.11: Sensitivity as a function of $\cos\theta^*$ and $\cos\psi^*$ for the channel $\tau^- \to \rho^- \nu_\tau$.

Note that the $\tau^- \to \pi^- \nu_\tau$ channel offers the highest sensitivity, as expected from its simple decay kinematics, but the ρ still carries a heavier weight because of its high branching ratio. The leptons exhibit somewhat lower sensitivity due to the two undetected neutrinos.

The data sample for this analysis consists of approximately 65,000 selected τ decays. Equation 2.15 predicts a statistical error on $\mathcal{P}_\tau$ of no better than about 0.011.

2.6 Systematic Errors

In this section we present a qualitative description of systematic errors in the τ polarization measurement arising from uncertainties in the selection procedure, the background estimation, the energy calibration, and the central tracking momentum

Channel	S	B.R.	W
$\pi^-\nu_\tau$	0.58	0.12	0.31
$K^-\nu_\tau$	0.52	0.01	0.02
$e^-\bar{\nu}_e\nu_\tau$	0.22	0.18	0.06
$\mu^-\bar{\nu}_\mu\nu_\tau$	0.22	0.18	0.06
$\rho^-\nu_\tau \rightarrow \pi^-\pi^0$	0.49	0.24	0.41
$a_1^-\nu_\tau \rightarrow \pi^-\pi^0\pi^0$	0.44	0.10	0.14

Table 2.2: Sensitivities, branching ratios, and weights for different decay channels used in the τ polarization measurement. Sensitivities are estimated for $\mathcal{P}_\tau = 0.14$. The weights are normalized.

resolution. A quantitative summary of systematic errors can be found in Chapter 6.

2.6.1 Selection

The τ selection, described in Chapter 4, is designed to be as energy independent as possible. Invariably, however, the selection efficiency depends to some extent on polarization sensitive quantities like energy[3]. The $\tau^- \rightarrow e^-\bar{\nu}_e\nu_\tau$, $\tau^- \rightarrow \mu^-\bar{\nu}_\mu\nu_\tau$, and $\tau^- \rightarrow \pi^-\nu_\tau$ selection efficiencies all fall off at low energies as shown in Figures 4.13, 4.14, and 4.15. In the case of the $\tau^- \rightarrow \rho^-\nu_\tau$ channel, the efficiency is dependent on θ^* and to a larger extent ϕ^* (Figure 4.17). If the shape of the efficiency curve is not faithfully reproduced in the Monte Carlo, then a bias may result. In the case of $\tau^- \rightarrow \pi^-\nu_\tau$, for example, an underestimation of the efficiency at low energy results in an overestimation of the number of low energy pions in the acceptance corrected spectrum. Figure 2.2 indicates that this would favor a more negative value for the polarization.

Since the τ polarization is an asymmetry, knowledge of the total acceptance is unnecessary. However maximizing the acceptance minimizes the statistical error.

2.6.2 Background

The problems introduced by background contamination are twofold. First, it increases the statistical error; the effect is more severe in regions where sensitivity

[3]The sources of these dependencies are described in Chapter 4.

to the polarization is high. Second, background contamination can bias the polarization measurement if it is not properly estimated and taken into account. Again, the severity of the bias depends on the sensitivity to polarization in the neighborhood of the background. Backgrounds from non-τ sources like $Z \to e^+e^-$, $Z \to \mu^+\mu^-$, two-photon interactions, and cosmic muons are estimated predominantly from data and cross checked with Monte Carlo simulation. Backgrounds from other τ decays are estimated from Monte Carlo.

Unfortunately, $Z \to e^+e^-$, $Z \to \mu^+\mu^-$, and two-photon events produce background at the extreme high and low energy regions of the τ decay spectra where sensitivity is generally high (Figures 2.10 and 2.11). The ideal decay spectra can be used to predict the gross effects of inaccurate background estimation. For example, Figure 2.4 indicates that an underestimation of $Z \to e^+e^-$ background in the $\tau^- \to e^-\bar{\nu}_e\nu_\tau$ channel will bias the polarization towards more negative values. On the other hand, underestimation of $Z \to e^+e^-$ background in the $\tau^- \to \pi^-\nu_\tau$ spectrum (Figure 2.2) will move the polarization in the opposite direction. A particularly insidious systematic in the $\mathcal{P}_\tau(\cos\theta)$ distribution for the the $\tau^- \to \pi^-\nu_\tau$ mode can arise if the $e^+e^- \to e^+e^-$ background is not handled carefully. The charge asymmetry in the reaction $e^+e^- \to e^+e^-$ is large because of the t-channel contribution to the cross section. For the $\tau^- \to \pi^-\nu_\tau$ channel this results in bhabha background that is some seven times higher in the forward than in the backward endcap. Figure 2.2 shows that an underestimated background at $E_\pi = E_{\rm beam}$ will shift the polarization to a more positive value. Thus the net result of underestimating the bhabha background is to bias the polarization measurement towards positive values at forward angles, which amusingly enough is opposite to the trend of the $\mathcal{P}_\tau(\cos\theta)$ curve (equation 1.32). Clearly then it is important to perform background estimation separately in each $\cos\theta$ bin.

2.6.3 Calibration

Uncertainties in the energy scale of the detector are potential sources of polarization bias since the energy is sensitive to polarization. Energy scale uncertainties may be manifest as either overall scale offsets or nonlinearities. The effect of a scale shift on $\mathcal{P}_\tau$ depends on the affected subdetector and the decay channel in question. For example, the $\mathcal{P}_\tau$ measurements in the $\tau^- \to \rho^-\nu_\tau$ and $\tau^- \to e^-\bar{\nu}_e\nu_\tau$ channels depend on the energy measurement from the electromagnetic calorimeter, described in Chapter 3. If the calorimeter were to systematically overestimate the energy, then the polarization measurement for $\tau^- \to e^-\bar{\nu}_e\nu_\tau$ would be shifted

towards more negative values, whereas the $\tau^- \to \rho^-\nu_\tau$ measurement would be shifted towards more positive values (Figures 2.2 and 2.7). Chapter 5 describes the methods used to verify the energy scales of L3 subdetectors.

In addition to energy scale, energy resolution is also important, mostly because it influences the statistical error. However a poor understanding of resolution can also produce a polarization bias, since in general the resolution depends on energy and so causes an energy-dependent smearing of the ideal spectrum shape. This is most easily seen in the case of the $\tau^- \to \pi^-\nu_\tau$ channel, which ideally has a spectrum that looks like Figure 2.2 but in practice produces the spectrum shown in Figure 6.6(a).

2.6.4 Charge Confusion

Charge confusion is the dominant systematic error in the $\mathcal{P}_\tau(\cos\theta)$ measurement. Every τ decay channel except $\tau^- \to \mu^-\bar{\nu}_\mu\nu_\tau$ relies on a charge measurement from the central tracker to determine the sign of $\cos\theta$. Occasionally the charge is misassigned; the probability for this charge confusion is a function of the momentum resolution of the central tracker, the momentum of the charged particle, and the underlying energy distribution for the decay channel in question. This is discussed in detail in Chapter 5. For the moment it is sufficient to note that the charge confusion is more severe at higher energies. If, due to charge confusion, the wrong sign is attached $\cos\theta$, then an entry which belongs in a bin at $\cos\theta$ migrates to $-\cos\theta$. This migration of events between forward and backward bins is illustrated in Figure 2.12. Charge confusion changes the shape of the $\mathcal{P}_\tau(\cos\theta)$ distribution in such a way that $|\mathcal{A}_\mathrm{e}|$ is always reduced and $\mathcal{A}_\tau$ remains almost unchanged.

The essential effects of charge confusion on the nominal values of $\mathcal{A}_\tau$ and $\mathcal{A}_\mathrm{e}$ can be understood from a few simple approximations. First consider the case of only two $\cos\theta$ bins, one for the forward ($\cos\theta > 0$) and one for the backward ($\cos\theta < 0$) hemisphere. We denote the *true* polarization in the forward bin by F and in the backward bin by B,

$$\begin{aligned} F &= \frac{N_+^F - N_-^F}{N_+^F + N_-^F} \\ B &= \frac{N_+^B - N_-^B}{N_+^B + N_-^B} \end{aligned} \tag{2.24}$$

where N_+^F is the *true* number of events with $h_\tau = +1$ in the forward hemisphere,

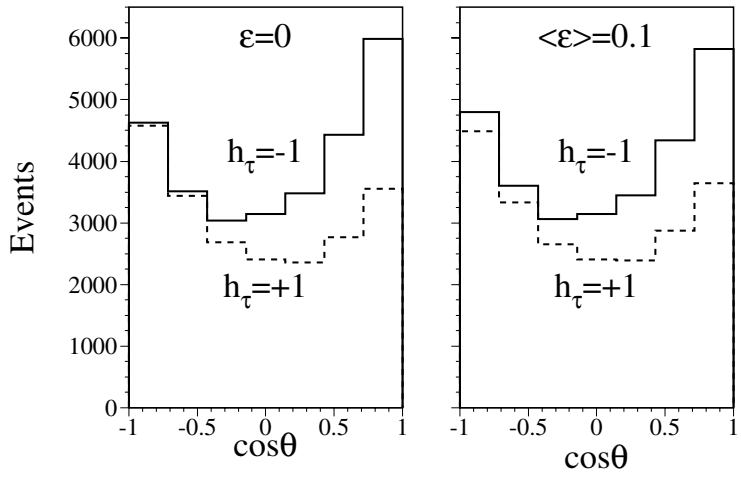

Figure 2.12: Distribution of $h_\tau = +1$ and $h_\tau = -1$ τ's as a function of $\cos\theta$ from Monte Carlo with polarization $\mathcal{P}_\tau = -0.13$ and average charge confusion ϵ. The spectrum on the left has no charge confusion. In the spectrum on the right, about 10% of the events are charge confused, resulting in a clear reduction in the difference between the polarization at forward and backward angles. The energy dependence of the charge confusion was accounted for in the simulation.

N_-^B is the number with $h_\tau = -1$ in the backward hemisphere, etc. Now we introduce charge confusion effects, subject to the following assumptions:

1. The probability for events to migrate between bins depends the average charge confusion, ϵ, where the average is taken over energy. ϵ can be used to readjust the number of positive and negative helicity τ's in the forward and backward bins. The resulting polarization can then be determined by counting these adjusted numbers.

2. ϵ is the same for both helicity states and is the same in the forward as in the backward bin.

Now, interpreting ϵ as the probability for events to migrate between the hemispheres, the *observed* polarizations are:

$$F' = \frac{N_+^F(1-\epsilon) + N_+^B\epsilon - N_-^F(1-\epsilon) - N_-^B\epsilon}{N^F(1-\epsilon) + N^B\epsilon} \tag{2.25}$$

$$B' = \frac{N_+^B(1-\epsilon) + N_+^F\epsilon - N_-^B(1-\epsilon) - N_-^F\epsilon}{N^B(1-\epsilon) + N^F\epsilon}$$

where $N^B = N_+^B + N_-^B$ and $N^F = N_+^F + N_-^F$. Using equation 2.24 these can be rewritten,

$$\begin{aligned} F' &= \frac{F(1-\epsilon)(1+\mathcal{A}_{\rm FB}) + B\epsilon(1-\mathcal{A}_{\rm FB})}{1+\mathcal{A}_{\rm FB}(1-2\epsilon)} \\ B' &= \frac{B(1-\epsilon)(1-\mathcal{A}_{\rm FB}) + F\epsilon(1+\mathcal{A}_{\rm FB})}{1-\mathcal{A}_{\rm FB}(1-2\epsilon)} \end{aligned} \tag{2.26}$$

where $\mathcal{A}_{FB} = (N^F - N^B)/(N^F + N^B)$ is simply the forward-backward charge asymmetry. The quantities we want to know, $\mathcal{A}_\tau$ and $\mathcal{A}_{\rm e}$, are given by

$$\mathcal{A}_\tau = \frac{F' + B'}{2} \tag{2.27}$$

and,

$$\mathcal{A}_{\rm e} = \frac{4}{3}(F' - B') \tag{2.28}$$

Interestingly, both $\mathcal{A}_{\rm e}$ and $\mathcal{A}_\tau$ are affected by charge confusion despite the symmetry imposed by assumption 2. The effect on $\mathcal{A}_{\rm e}$ is clear from Figure 2.12 and equation 2.28; the less obvious effect on $\mathcal{A}_\tau$ is due to the presence of $\mathcal{A}_{\rm FB}$ in equations 2.26. The shift in $\mathcal{A}_\tau$ is very small, however, since for $\mathcal{A}_\tau = \mathcal{A}_{\rm e} = -0.14$, $\mathcal{A}_{\rm FB} = \frac{3}{4}\mathcal{A}_\tau\mathcal{A}_{\rm e} \approx 0.015$. For example, in the extreme case of maximal charge confusion, $\epsilon = 50\%$, $\mathcal{A}_{\rm e}$ vanishes completely, but $\mathcal{A}_\tau$ only changes by 0.001. The average endcap charge confusion derived from a simulation using the measured detector resolution is about 3% (see Chapter 6); this represents the worst case. If this number is used then $\mathcal{A}_{\rm e}$ decreases by .008 (the change in $\mathcal{A}_\tau$ is minute).

It is also worth noting that equations 2.26 imply that $F' - B' = (F - B)(1 - 2\epsilon)$, neglecting $\mathcal{A}_{\rm FB}$. Since $\mathcal{A}_{\rm e} \propto F' - B'$, charge confusion can only reduce $|\mathcal{A}_{\rm e}|$.

In the argument above, assumption 1 ignores the fact that the polarization is in practice determined from the shape of the τ decay spectrum. The effect of charge confusion on this shape is quite complicated and depends on the decay channel, the helicity, the details of the detector resolution, and the method used to determine the charge. Assumption 2 is not strictly true since, for example, the average charge confusion is expected to be larger in the forward hemisphere since forward-going τ's are more strongly polarized and hence exhibit a more energetic

decay spectrum. Furthermore the charge confusion probability can be different for the two helicity states if both τ's in an event are used to determine the charge (see Chapter 6). However, the difference in the charge confusion among these various cases is small compared to the charge confusion itself[4], and the approximation is reasonable.

It is useful to check this approximation by taking another approach. This time we attempt to estimate the influence of charge confusion by considering its general effect on the shape of the decay energy distribution for the $\tau^- \to \pi^-\nu_\tau$ channel. Again, we split the hypothetical sample into two hemispheres, and retain assumption 2 from the previous approximation.

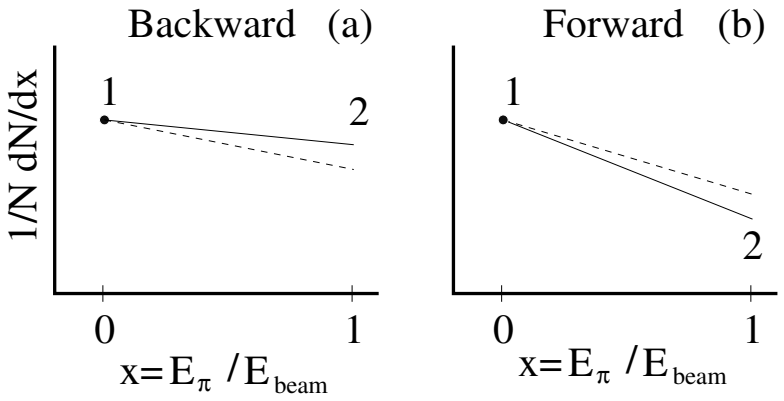

Figure 2.13: Schematic picture of the effect of charge confusion on the shape of the forward and backward energy spectra for $\tau^- \to \pi^-\nu_\tau$. The solid lines show the shape of the energy spectrum, and the dashed lines indicate the effect of charge confusion on the spectrum shape.

The solid line in Figure 2.13(a) indicates the shape of the ideal pion energy spectrum for the backward bin (see equation 2.6). The stronger polarization expected in the forward bin is reflected in a spectrum with a more negative slope, as depicted by the solid line in Figure 2.13(b). We approximate the effect of charge

[4]A detailed simulation using the measured detector resolution is described in Chapter 6. From this simulation, it was found that in the endcaps the difference between charge confusion at 45 GeV for $h = +1$ and $h = -1$ τ's is about 5% of the average charge confusion. The difference between the averages for the forward and backward endcaps is negligible. In the barrel, the charge confusion is about a factor of two smaller than in the endcaps.

confusion on the spectrum shape by considering only the spectrum endpoints, $E_{\pi^-}/E_{\rm beam} = 0$ and $E_{\pi^-}/E_{\rm beam} = 1$. At the point labeled 1 in Figure 2.13(a) there is no change in the spectrum because the charge confusion is $\epsilon_1 \approx 0$ for $E_{\pi^-}/E_{\rm beam} \approx 0$. At point 2, where the energy is highest, the charge confusion ϵ_2 is maximal. Charge confusion causes point 2 to shift down as indicated by the dashed line. The downward shift results since that there are more events at point 2 in the backward bin than at point 2 in the forward bin, and therefore more events migrate out of the backward bin than into it. By a similar argument, the slope in the forward bin becomes less negative.

This argument can be quantified as follows. Let F and B from equations 2.25 denote the polarizations in the forward and backward hemispheres. If we suppose $\mathcal{A}_\tau = \mathcal{A}_{\rm e} = 0.14$, then before charge confusion effects we have $F = -0.0875$ and $B = -0.1925$ (see equations 2.28 and 2.27). From equation 2.6, it is evident that the number of events at point 1 in Figure 2.13(b) is proportional to $1 - F$, and the number of events at point 2 is proportional to $1 + F$. Similarly for Figure 2.13(a), point 1 is proportional to $1 - B$ and point 2 is proportional to $1 + B$. Now we introduce charge confusion. As mentioned previously, there is no charge confusion at point 1, so the proportionality remains unchanged. At point 2, the proportionality is adjusted according to the migration of events between hemispheres:

$$\text{point 1}: \quad 1 - F = \mathcal{N}(1 - F') \tag{2.29}$$

$$\text{point 2}: \quad (1 + F)(1 - \epsilon_2) + (1 + B)\epsilon_2 = \mathcal{N}(1 + F') \tag{2.30}$$

where F' is the polarization observed after charge confusion and $\mathcal{N}$ is the normalization for the charge confused energy spectrum. Similar equations hold for the other hemisphere. Solving these equations yields,

$$\begin{aligned} B' &= \frac{2B + \epsilon_2(F - B)}{2 + \epsilon_2(F - B)} \\ F' &= \frac{2F - \epsilon_2(F - B)}{2 - \epsilon_2(F - B)} \end{aligned} \tag{2.31}$$

We take $\epsilon_2 = 0.07$, which is the endcap charge confusion at $E_{\pi^-} = 45$ GeV estimated using the measured detector resolution. This figure represents the worst case and corresponds to the numbers used in the previous approximation. Inserting the numbers for F, B, and ϵ_2 and using equation 2.27 gives the result $\mathcal{A}_{\rm e} = 0.129$,

which is a shift of 0.011 from the polarization before charge confusion. Notice that this is reasonably consistent with the result of the previous estimation.

The effect of charge confusion was also estimated using a fast Monte Carlo which includes all the τ decay spectra used in the analysis as well as realistic energy dependence of the charge confusion. The effect on the shape of $\mathcal{P}_\tau(\cos\theta)$ is shown in Figure 2.14 for the case of several θ bins. For this figure, ϵ was set to an unrealistically high value in order to make its effect easily discernable. When realistic tracking resolution is used in the Monte Carlo which generated the figure, the shift in $\mathcal{A}_e$ is less than 0.01, which is promising.

It is imperative to correct for this one-sided effect on $\mathcal{A}_e$. The approximations discussed above prove to be quite useful in estimating the correction for charge confusion as well as the systematic error on the correction. The key point is that to a good approximation the shift in polarization for a given $\cos\theta$ bin and τ decay channel is proportional to the product of the average charge confusion for events containing that channel and the difference of polarizations in oppositely signed $\cos\theta$ bins. We observe this for the approximation based on counting (equations 2.26) as well as the approximation based on the spectrum shape (equations 2.31). The dashed line in Figure 2.14 shows the result of applying this prescription to the distribution given by the solid line.

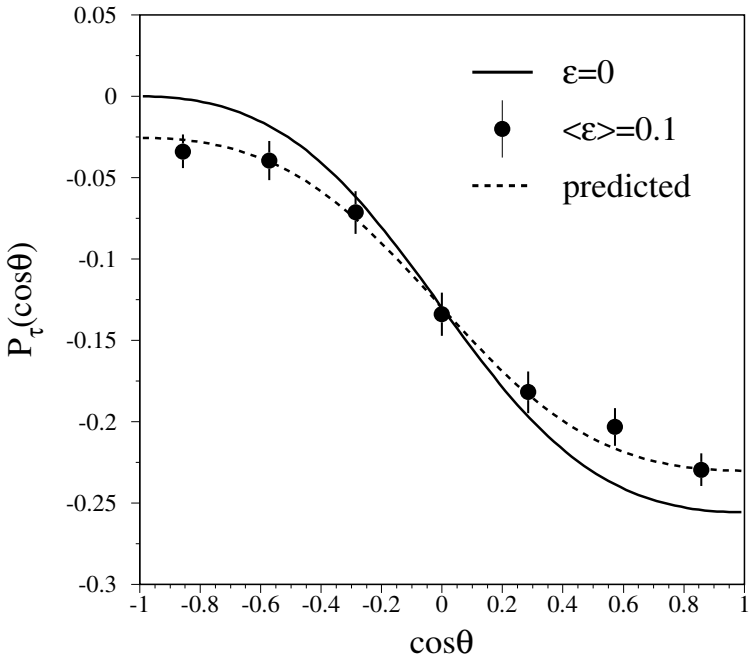

Figure 2.14: The $\mathcal{P}_\tau(\cos\theta)$ distribution from Monte Carlo with and without charge confusion. The line is for the case $\mathcal{A}_\tau = \mathcal{A}_e = -0.13$ and $\epsilon = 0$. The solid dots are for the case of average charge confusion $\langle\epsilon\rangle \approx 10\%$. The dashed line labeled "predicted" results if the values indicated by the solid line are shifted by the average charge confusion multiplied by the difference of polarizations at oppositely signed $\cos\theta$ points (see text).

Chapter 3

The L3 Detector

3.1 The LEP Collider

The CERN Large Electron Positron collider, LEP, is designed to provide colliding e^+ and e^- beams at center-of-mass energies up to 200 GeV. In 1993, the luminosity was typically in excess of $\mathcal{L} = 10^{31}\text{cm}^{-2}\text{s}^{-1}$. LEP is situated in a tunnel of 27 km circumference which passes through Swiss and French territory, as shown in in Figure 3.1. The collider consists of eight bending sections, each 2840 m in length, and eight 490 m straight sections. The bending sections contain the 3304 dipole magnets which steer the beams around the ring. Four of the eight straight sections house the large detectors ALEPH, DELPHI, L3, and OPAL. Two of the straight sections contain radiofrequency cavities which are used to accelerate the beams from injection energy to collision energy and to compensate synchrotron radiation. On either side of each detector, there are superconducting quadrupole magnets which compress the beams for increased luminosity. The veteran PS and SPS accelerators are used together with an accumulation ring and the LIL linear accelerator as an injection system for LEP. At the beginning of a fill, the injection complex provides electrons and positrons at an energy of 20 GeV. The beams are then ramped by LEP to collision energies, and a typical beam lifetime is around 20 h. LEP has been operated in both 4×4 and 8×8 bunch modes[1], with 8×8 operation predominant since 1992.

The data sample for the 1990-1993 running periods consists of a total integrated

[1] A bunch is a longitudinally localized group of electrons or positrons. 8×8 bunch mode, for example, means 8 bunches of electrons and 8 bunches of countercirculating positrons.

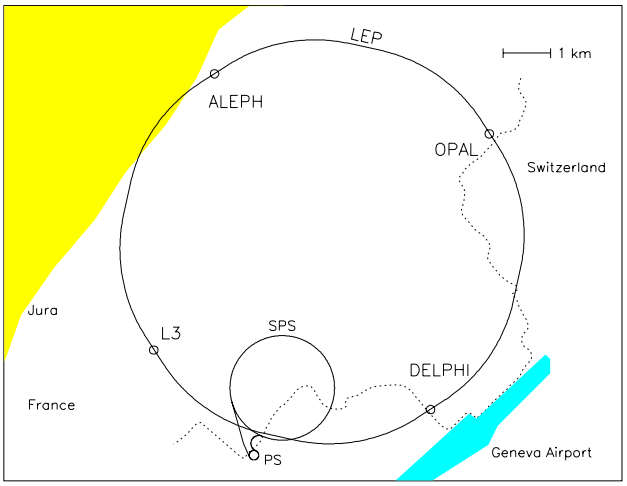

Figure 3.1: LEP geography.

luminosity of 79 pb^{-1}, collected on and around the Z peak.

3.2 The L3 Detector

The L3 detector design emphasizes high resolution energy measurements of electrons, photons, muons, and jets produced in e^+e^- collisions at energies up to 200 GeV. Figure 3.2 shows a perspective view of L3. Figure 3.3 and Figure 3.4 show $r-\phi$ and $r-z$ slices respectively.

The L3 subdetectors are supported by a 32 m long, 4.45 m diameter steel support tube which is coaxial with the LEP beam pipe. The central tracking and calorimetry is contained inside the support tube and consists of a muon filter, hadron calorimeter, electromagnetic calorimeter, tracking chamber, and silicon vertex detector (Figures 3.2, 3.3, and 3.4). These subdetectors are arranged in "barrel" elements around the beam pipe, and "endcap" elements in the forward and backward directions. Three layers of drift chambers which form the muon spectrometer are mounted outside the support tube.

All of the subdetectors are contained inside a large conventional magnet which

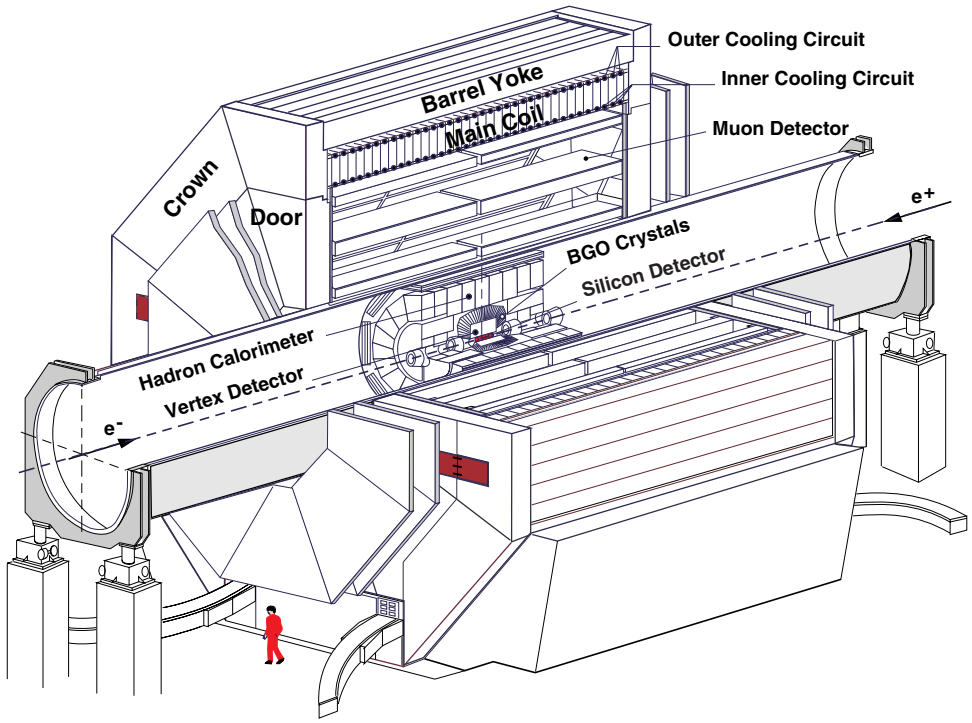

Figure 3.2: Perspective view of L3.

provides a uniform 0.5 T field for measuring charged particle momenta. A large magnet with a relatively low field was chosen in order to optimize muon momentum resolution, which improves linearly with the field but quadratically with the lever arm (equation 5.1).

Standard spherical coordinates are used to describe positions and directions in L3. The z-axis is defined by the direction of the e^- beam (Figure 3.4), and θ and ϕ are the polar and azimuthal angles, respectively. The origin is taken as the e^+e^- collision point.

A detailed description of L3 can be found in reference [19].

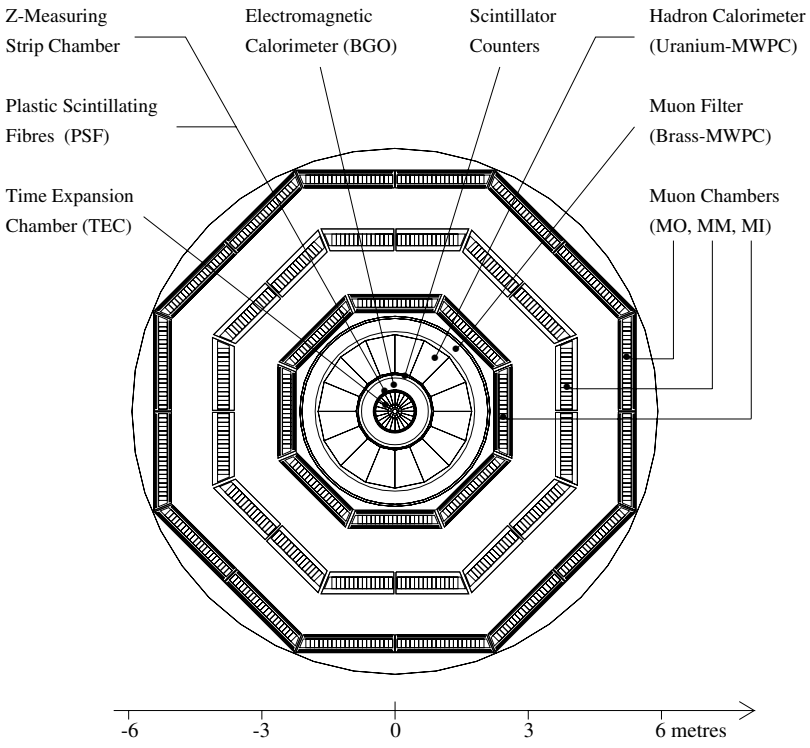

Figure 3.3: $r - \phi$ view of L3.

3.2.1 Magnet

The magnet coil is made from welded aluminum plates of inner radius 5.93 m and total length 11.9 m. The coil carries a current of 30 kA, providing a 0.5 T field parallel to the z-axis. The return yoke is made of soft iron with an inner radius of 8 m. A water-cooled thermal shield is located inside the coil to protect the detectors. The magnetic field is mapped inside the support tube with Hall probes, and outside with about 1000 magnetoresistors mounted to the muon spectrometer. Five NMR probes provide further monitoring of the absolute field value.

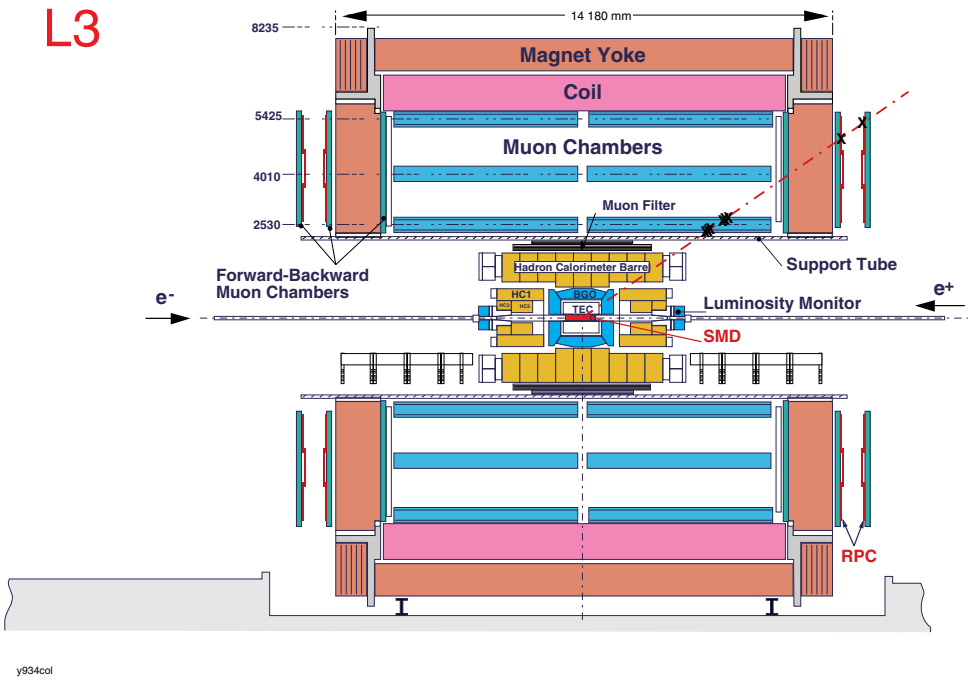

Figure 3.4: $r - z$ view of L3.

3.2.2 Central Tracking

The central tracking system consists of a Time Expansion Chamber (TEC) which provides tracking in $r - \phi$, a Z-chamber which measures the track $z-$coordinate, Forward Tracking Chambers (FTC's) in the endcap regions, a Silicon Microvertex Detector (SMD), and a Plastic Scintillating Fiber (PSF) system for use in calibration. The SMD was first installed for testing in the 1993 data taking period and has not yet been used in the τ polarization analysis, so it is not described here.

Due to size constraints imposed by the electromagnetic calorimeter, the TEC has only a modest lever arm of 31.7 cm, and as pointed out previously the L3 magnetic field is relatively low. This necessitates excellent spatial resolution in order to achieve the design goal of charge identification for 50 GeV particles at 95% confidence level. A drift chamber design which follows the time expansion principle was therefore chosen [20]. In this design a high field amplification region

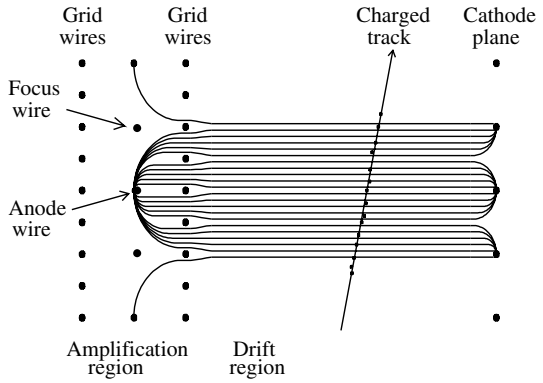

Figure 3.5: Amplification and drift regions in the TEC.

is separated from a low field drift region by two planes of grounded grid wires, as illustrated in Figure 3.5. A drift velocity of approximately 6μm/ns is attained in the low-field region, through which about 80% of all tracks pass completely. This low drift velocity together with a drift time measurement which employs a center of gravity technique results in a resolution of $\sigma \approx 60$ μm for the 8 inner anodes and $\sigma \approx 50$ μm for the 54 outer anodes[2].

The TEC anode wires are arranged in planes parallel to the $z-$axis, so that the coordinate measurement is made in the bending plane. The chamber is divided into 12 inner and 24 outer sectors as show in Figure 3.6. A plane of cathode wires separates the sectors. A detailed view of a single inner sector and the corresponding outer two sectors is shown in Figure 3.7. The matching of an inner half-sector to an outer sector helps to reduce pattern recognition problems associated with ambiguity in the sign of the drift distance from track to anode. Transverse momentum resolution varies as a function ϕ, but on average is $\sigma_{1/P_T} \approx 0.018$ in the drift region for tracks with $|\cos\theta| < 0.72$. A detailed discussion of resolution and an outline of the TEC calibration are given in Chapter 5.

The Z-chamber provides a precise measure of the track $z-$coordinate. This

[2]In fact the single wire resolution depends also on the drift distance to the wire and varies from less than 40 μm near the grid to about 100 μm close to the cathode plane.

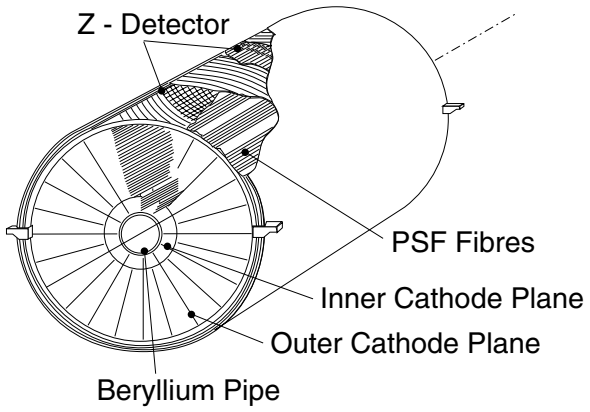

Figure 3.6: Perspective view of the TEC, Z-chamber, and PSF.

detector covers the outer cylinder of TEC, and consists of two thin cylindrical multiwire proportional chambers with cathode strip readout. The cathode strips are inclined with respect to the $z-$axis by 69° and 90° for the inner chamber, and by $-69°$ and $-90°$ for the outer chamber. The $z-$coordinate resolution is about 320 μm. The FTC consists of drift chambers between the TEC endflange and the electromagnetic calorimeter endcap. It can in principle be used to measure the charge of tracks in the forward and backward hemispheres. The PSF system consists of ribbons of scintillating fibers arranged between the outer surface of the TEC and the inner surface of the Z-chamber, as depicted in Figure 3.6. The fibers provide an external space point which can be used to calibrate the global drift velocity in the TEC. The TEC, Z-chamber, and PSF systems are described in detail in reference [21].

3.2.3 Electromagnetic Calorimeter

The electromagnetic calorimeter [23] is constructed of an array of bismuth germanium oxide (BGO) crystals which serve as both a showering and the detecting medium, thereby reducing sampling fluctuations. The crystals are in the shape of truncated pyramids arranged so that they all point towards the interaction region, as shown in Figure 3.8. The calorimeter is divided into a barrel region which

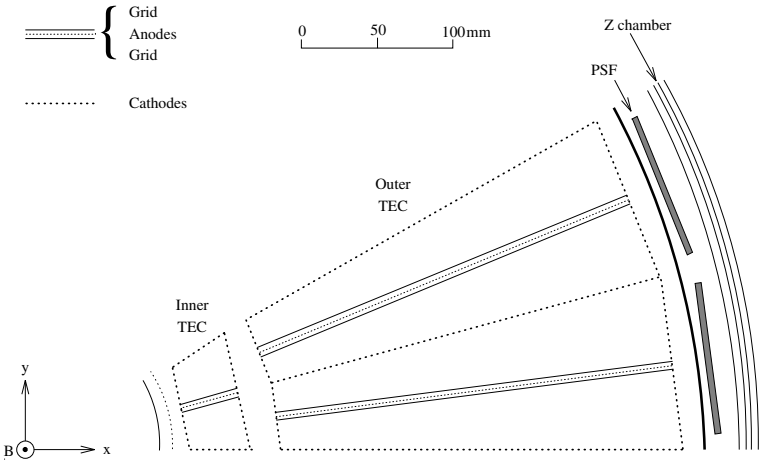

Figure 3.7: Geometry of a TEC sector.

covers $-0.72 < \cos\theta < 0.72$ and consists of 7680 crystals, and two endcap regions which cover the range $0.80 < |\cos\theta| < 0.98$ and and each contain 1527 crystals. The geometry of a single crystal is shown in Figure 3.9. The scintillation light in a crystal is read out by two photodiodes glued to its rear face.

Due to aging and radiation damage, the transparency of BGO changes with time. Crystal transparency is monitored using light from xenon lamps which is delivered to the crystals via fiber optic cables [22]. Bhabha events are used together with information from the xenon monitoring system to determine the BGO calibration.

The BGO exhibits excellent resolution for electromagnetic showers over a large range of energies . At 100 MeV the energy resolution is about 5%, and between 1 GeV and 100 GeV the resolution is better than 2%. Compared to the Molière radius in BGO (2.3 cm), the calorimeter is finely segmented, so electromagnetic showers typically spread over nine or more crystals. This allows accurate reconstruction shower centroids. The resulting position resolutions vary from about 4 mm at 1 GeV to 1 mm at 45 GeV. This translates to an angular resolution of between 4 mrad and 7 mrad. The fine segmentation also makes possible precise analysis of transverse energy deposition in the calorimeter, thus allowing discrimination between electrons and pions (see chapter 4).

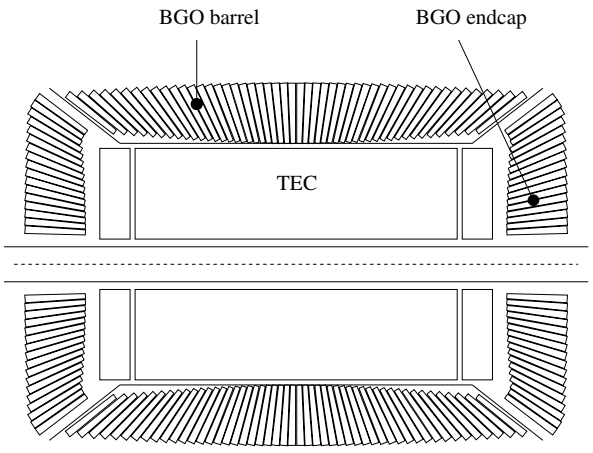

Figure 3.8: $r - z$ view of the electromagnetic calorimeter (BGO) showing the projective geometry.

3.2.4 Scintillation Counters

The scintillation counter system is positioned between the electromagnetic and hadron calorimeters, as shown in Figure 3.10, and consists of 30 plastic scintillating counters read out by photomultiplier tubes, and covers the polar range $|\cos\theta| < 0.83$, and about 93% of the azimuthal angle.

This system can be used to trigger hadronic events based on scintillator hit multiplicity, and to reject cosmic muons based on timing. Cosmic muons that pass near the interaction vertex can mimic dimuons produced in e^+e^- collisions.

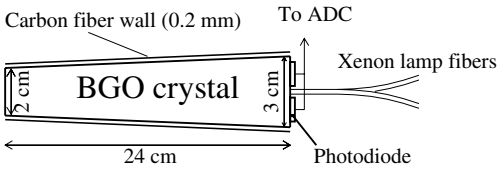

Figure 3.9: A single BGO crystal.

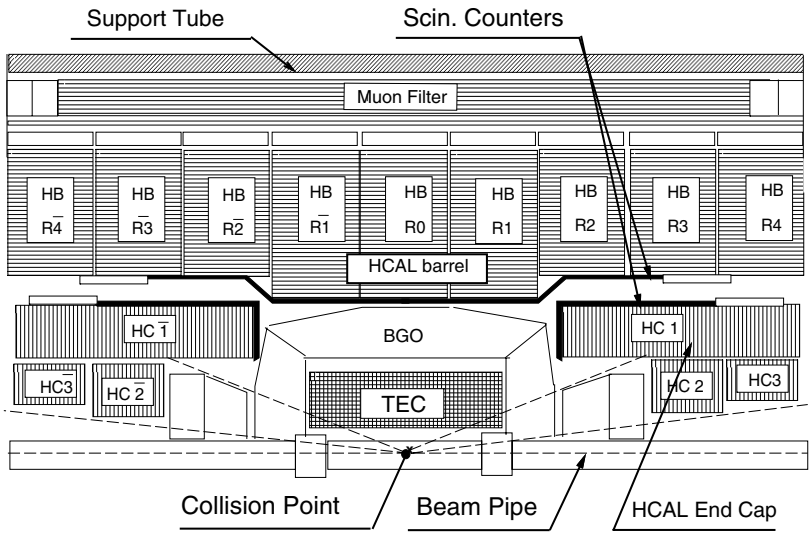

Figure 3.10: A slice of L3 showing the location of, among other things, the scintillator system.

However, cosmics require about 6 ns to traverse the space between scintillators, whereas muons from e^+e^- interactions strike opposing scintillators simultaneously. The scintillator timing resolution of better than 0.5 ns makes it possible to distinguish these two cases.

3.2.5 Hadron Calorimeter and Muon Filter

The energy of hadrons produced in e^+e^- collisions is measured by the total absorption technique using a combination of the electromagnetic and hadron calorimeters. The hadron calorimeter (HCAL) [24] can also be used to identify muons from their minimizing-ionizing signature. Total absorption in the HCAL and the muon filter also serves to shield the muon spectrometer from showering particles.

The HCAL consists of a barrel region which covers the angular range $34° < \theta$ $145°$ and two endcaps which cover $5° < \theta < 35°$ and $145° < \theta < 175°$. The HCAL barrel

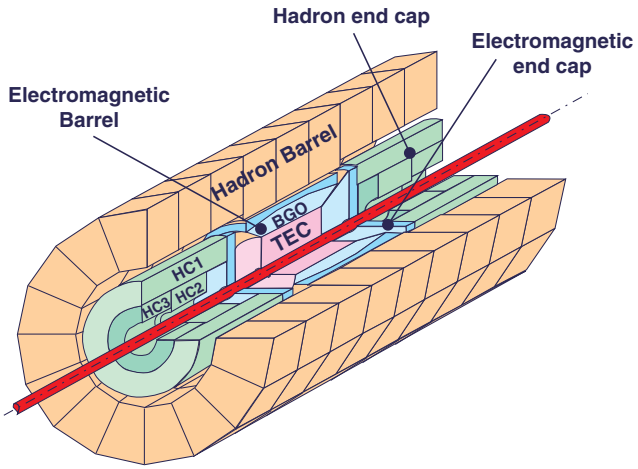

Figure 3.11: The hadron calorimeter.

is made of 55 mm thick depleted uranium absorbers interspersed with 7968 brass tube proportional chambers. The choice of a uranium absorber was motivated by the need for a compact calorimeter which allows the largest possible lever arm for the muon spectrometer. The HCAL is divided into 9 rings of 16 modules each. The endcaps each consist of one outer and two inner rings. The barrel and endcap geometry is depicted in Figures 3.10 and 3.11.

The wires in each module are grouped into readout towers, each of which typically covers an angular interval $\delta\theta = 2°$, $\delta\phi = 2°$. The wires are oriented alternately along and perpendicular to the z-axis.

The muon filter is located outside the HCAL barrel as show in Figure 3.11. It is divided into octants, each made from brass plates interleaved with proportional tubes. The muon filter increases the nuclear absorption length of the barrel calorimeter, further shielding the muon chambers from showering particles. In total, the barrel calorimeter constitutes about 5 nuclear interaction lengths.

The calorimeter system allows determination of the jet axis with a resolution

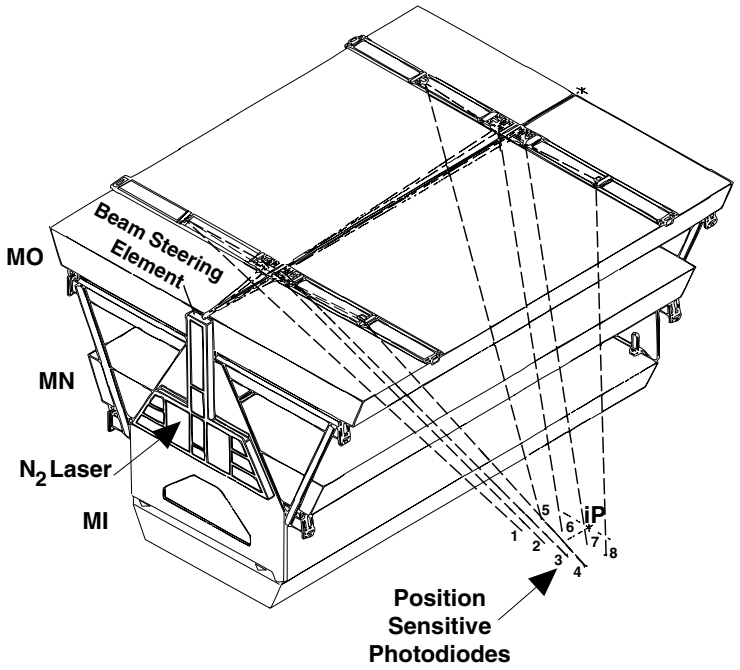

Figure 3.12: A muon spectrometer octant.

of about 2.5° and charged pion energy measurement with resolution better than[3] 20% above about 15 GeV.

3.2.6 Muon Spectrometer

The muon spectrometer [25] is designed to measure the momentum of penetrating charged particles with accuracy $\sigma_P/P \approx 2.5\%$ at 45 GeV. The spectrometer is located between the support tube and the magnet coil, as shown in Figure 3.2, and consists of 16 independent units arranged into 2 octagonal ferris wheels. A single unit or "octant" is shown in Figure 3.12.

Each of the 16 octants consists of three layers of drift chambers as shown in Figure 3.12, and more schematically in Figure 3.13. All three layers contain "P-

[3]Resolution is improved by combining the calorimeter and TEC measurements, as described in Chapter 5.

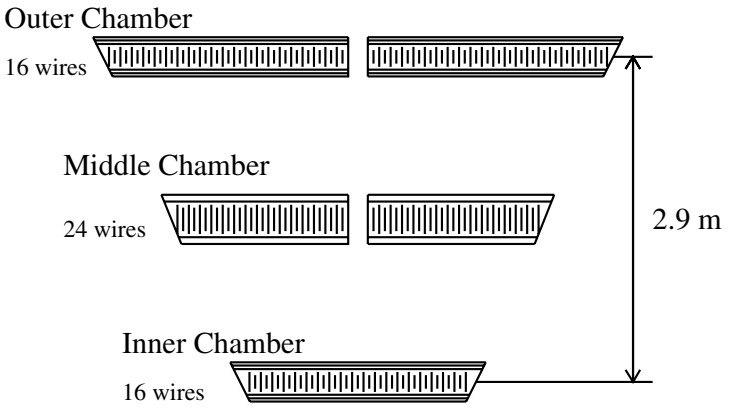

Figure 3.13: Front view of a muon spectrometer octant. The Z-chambers are located on either surface of the inner and outer P-chambers.

chambers" which measure the $r-\phi$ coordinate, and the inner and outer layers each contain "Z-chambers" which measure the $z-$coordinate. The three layers offer a 2.9 m lever arm for momentum analysis. Alignment tolerances of better than 30 μm between layers in the same octant[4] and an $r-\phi$ coordinate measurement with precision around 50 μm in each layer are required in order to achieve the design resolution. The transverse momentum measurement from the P-chambers is combined with the θ measurement from the Z-chambers to construct the 3-momentum of the track.

The muon spectrometer covers the polar range[5] $|\cos\theta| < 0.8$ Tracks in the range $|\cos\theta| > 0.71$, however, can only form hits in the inner two chambers.

3.2.7 Luminosity Monitor

The luminosity monitor is used to detect low angle $e^+e^- \rightarrow e^+e^-(\gamma)$ events and measure the scattering angles of the electrons and positrons. At low angles this

[4]Tracks with momentum higher than 3 GeV are confined to a single octant, so alignment between octants is not critical

[5]Portions of forward-backward muon chamber system have also been installed for the 1994 data-taking period.

reaction has a large cross section and is dominated by t-channel photon exchange, a well understood QED process. The measured rate is then compared to theoretical calculations to deduce the luminosity.

The luminosity monitor consists of two BGO electromagnetic calorimeters, two sets of proportional wire chambers, and two Silicon Luminosity Monitors (SLUM's) situated symmetrically on either side of the interaction point. Each calorimeter consists of an azimuthally symmetric array of 304 BGO crystals covering the range $24.9 < \cos\theta < 69.9$ mrad. The energy resolution of the calorimeters is about 2% at 45 GeV and the angular resolution is is 0.4 mrad in θ and 0.5° in ϕ. The SLUM's each consist of three layers of single-sided sensors, two of which provide the r-coordinate while the remaining layer determines ϕ. Each sensor layer consists of 16 wafers with strip pitches varying from 500 μm to 1750 μm. The combined BGO, wire chamber, and SLUM systems provide a luminosity measurement precise to 0.16%.

3.2.8 Trigger

The LEP beam crossing period is 22 μs in 4×4 bunch mode and 11 μs in 8×8 mode. About 100 ms is required to fully digitize all L3 subdetector signals and write an event to tape. The L3 trigger system performs a rapid analysis of the response of the various subdetectors at each beam crossing in order to determine whether a candidate e^+e^- event was produced. The goal is to minimize dead time that results from writing information from crossings with no detected particles, or from background events due to, for example, beam-gas interactions or cosmic rays. The trigger system is divided into three levels of increasing complexity. Each of the three levels applies several selection criteria which are logically OR'ed to produce a trigger.

Level-1 Trigger

Level-1 is based on five separate triggers; these come from the calorimetry, the luminosity monitor, the scintillation counters, the muon chambers, and the TEC. A positive result from any of the five causes the fine digitization to commence for analysis by the subsequent levels. Level-1 produces a typical trigger rate of less than 8 Hz.

Calorimeter Trigger: This trigger is designed to select events which deposit energy in the electromagnetic or hadronic calorimeters, such as $e^+e^-, \tau^+\tau^-$,

hadronic events, and $\nu\bar{\nu}\gamma$. The inputs consist of the analog sums of groups of BGO crystals and hadron calorimeter towers; barrel and endcap BGO crystals are grouped into $32\phi \times 16\theta$ blocks and hadron calorimeter towers are grouped into 16×11 blocks for layers less than about one absorption length and 16×13 blocks for deeper layers. The event is accepted if the BGO energy exceeds 25 GeV in the barrel and endcaps or 8 GeV in the barrel alone, or the total calorimetric energy exceeds 25 GeV in the barrel and endcaps or 15 GeV in the barrel alone. The $\theta - \phi$ projections are also used to search for clusters. The cluster threshold is 6 GeV, or 2.5 GeV for clusters in spatial coincidence with a track from the TEC trigger. The main source of background for this trigger is electronic noise, and the trigger rate is typically 1 to 2 Hz.

Scintillator Trigger: The scintillator system is used in level-1 to trigger on high multiplicity events. Events with at least 5 hits spread over 90° are selected. The trigger rate is typically 0.1 Hz. This trigger is practically background free.

Muon Trigger: The muon trigger selects events with at least one penetrating charged particle. Events are selected if hits in the muon chambers can be formed into a track with transverse momentum greater than 1 GeV. At least 2 P-layers and 3 Z-layers are required. Cosmic muons are rejected by requiring one good scintillator hit within 15 ns of the beam crossing. A 1 Hz trigger rate is typical.

Luminosity Trigger: Signal processing for this trigger is similar to that for the calorimeter trigger. An event is selected if any of the following criteria are met: two back-to-back depositions with $\geq$ 15 GeV, total energy on one side $\geq$ 25 GeV and on the other $\geq$ 5 GeV, or total energy on either side $\geq$ 30 GeV. A typical trigger rate is 1.5 Hz for normal beam conditions.

TEC Trigger: The TEC trigger selects events with charged tracks. Tracks are required to have a transverse momentum of more than 150 MeV, and an event is selected if at least two tracks are found with acolinearity less than 60°. The TEC trigger rate is generally around 1 Hz, but can increase by several Hz during bad beam conditions.

Level-2 Trigger

Level-2 attempts to reject background events selected by level-1. At this level, more time can be spent analyzing an event without incurring additional deadtime, and furthermore signals from different subdetectors can be correlated. Level-2 is effective in removing calorimeter triggers due to electronic noise, and TEC triggers due to beam-gas and beam-wall interactions. Events that produce more than one

level-1 trigger are not rejected by level-2. The trigger rate after level-2 is typically less than 6 Hz.

Level-3 Trigger

This level executes a more detailed analysis of events that pass the previous two levels. Results of the fine digitizations are used, so more precise thresholds can be set for the calorimetry, which further reduces electronic noise. Muon triggers are required to fall within more stringent 10 ns scintillator coincidence, thereby reducing background from cosmic muons. Tracks selected by the TEC trigger are correlated with at least 100 MeV of energy in the calorimeters and are checked for quality and for a common vertex. Events that produce more than one level-1 trigger are not rejected by level-3. After Level-3, the overall trigger rate is generally around 3 Hz. From analysis of TEC and energy trigger coincidences, the trigger efficiency for $e^+e^- \to Z \to q\bar{q}$ is found to exceed 99.9% [26].

3.3 Event Reconstruction

The off-line event reconstruction follows several steps. First the information from the online data acquisition system is read and decoded. Next, reconstruction is carried out for each subdetector. Finally, associations are made between the reconstructed objects in different subdetectors to produce the kinematic variables that characterize an event.

Reconstruction is performed for all data written to tape, and reconstructed events are stored in several formats. The Master Data Reconstructed stream (MDRE) is produced from the procedure described below; it contains all the information necessary to repeat the full detector reconstruction. The typical size of an event in MDRE format is about 150 kBytes, compared to about 370 kBytes required for the raw data. Compressed data formats include the Data Summary Unit (DSU), which contains enough information for partial reconstruction of some detector objects. A DSU event typically occupies 22 kBytes.

3.3.1 Subdetector Reconstruction

Muon Spectrometer: Measured drift times for hit wires in each chamber are converted to space points, which are grouped into segments. An attempt is made

to match segments between layers in the spectrometer, and a track is formed if at least two P-segments can be associated. A helix is then fitted to the P-segments together with associated Z-segments, thus providing a measure of the momentum and charge. Finally, the track is extrapolated back to the interaction region and the expected energy loss in the calorimetry is computed based on the assumption that the track is from a minimum ionizing particle. This energy loss is added to the track momentum measured in the spectrometer in order to arrive at the track momentum in the interaction region.

Hadron Calorimeter: Charge collected on the wires of each readout tower is converted to energy deposition using empirically determined constants, thereby forming "hits." A clustering algorithm groups the hits into geometrical clusters, where an energy weighting scheme is used to assign the cluster position.

Scintillators: Times and energy depositions are computed for each scintillator.

Electromagnetic Calorimeter: Local maxima are identified in the array of BGO crystals, forming "bumps." The bump energies are computed, and the bump center-of-gravity is found using all the crystals around the bump with energies above 30 MeV. A shower shape analysis is performed in an attempt to identify energy depositions due to electrons and photons. Contiguous bumps are grouped into geometrical "clusters."

Central Tracking: Measured drift times for hit wires are converted to space points in each sector using calibration constants derived from an off-line analysis. A pattern recognition algorithm associates the points with tracks in the $r-\phi$ plane. A circle is then fitted to tracks yielding the curvature, distance of closest approach to the vertex, and the azimuthal angle for the track. The extrapolated impact point of the track with the Z-chamber in the $r-\phi$ plane is computed and associated with a reconstructed Z-chamber hit. The resulting z-coordinate is used together with the average e^+e^- interaction point to fit a helix to the track[6].

3.3.2 Global Reconstruction

Due to the fine segmentation of the calorimeters, it is possible to construct "Smallest Resolvable Clusters" (SRC's), each of which roughly corresponds to a single final state particle. Initially, tracks in the muon spectrometer are associated with clusters in the hadron calorimeter, bumps in the electromagnetic calorimeter, and

[6]Starting with 1993 data, preliminary SMD reconstruction algorithms have been incorporated into the central tracking reconstruction.

tracks in the TEC. Remaining bumps in the electromagnetic calorimeter and clusters in the hadron calorimeter are then used to construct SRC's. The 3-momentum for each SRC is then computed, where the total energy determines the magnitude and the energy weighted average of the positions of SRC components determines the direction. At this stage, an approximate energy calibration is used. During a second reconstruction pass, SRC's of identified particles can be computed using a more accurate calibration that depends on particle type.

SRC's and muons are used to compute a thrust axis, $\hat{T}$, for each event. The thrust axis is defined as the vector that minimizes the expression,

$$\left| \sum_i \vec{P}_i \cdot \hat{T} \right| \tag{3.1}$$

where $\vec{P}_i$ is the momentum of the i'th particle.

3.4 Detector Simulation

A precision measurement requires detailed understanding of detector response to the process under study. In the τ polarization measurement, for example, it is crucial to understand the effect of the detector on the shape of energy spectra of the τ decay products, since it is these spectra that are used to determine the polarization. Computer simulation plays an important role in analyzing the detector response and estimating backgrounds and systematic errors.

The Monte Carlo event simulation proceeds in three steps. First, an event generator simulates the physics process of interest, and produces a sample of final state particles and their 4-momenta [27]. The simulated events are then propagated through a detailed representation of the L3 detector, which includes simulation of all the tracking and showering in the detector materials, as well as simulation of the response of active regions of the detector [28]. The resulting digitized simulated events are then fed to the offline reconstruction program described above.

Discrepancies between data and Monte Carlo distributions for well understood physics processes can reveal deficiencies in the understanding of detector calibration or energy scale, or can result from incomplete modeling of detector efficiency and resolution in the Monte Carlo itself. Deficiencies in the simulation generally result in underestimation of resolution and detector inefficiencies. To correct for this, we compare the relevant Monte Carlo distributions to data to determine what additional smearing, if any, is necessary. For example, the TEC resolution

in the Monte Carlo sample is compared to the resolution measured from data using dimuon and bhabha events, as described in Chapter 5. Any underestimation observed in the Monte Carlo sample is corrected by introducing additional smearing to all Monte Carlo TEC track curvature measurements. Such after-the-fact correction is generally called "resmearing."

Chapter 4

Selection

The selection of τ decay candidates proceeds in three steps. First a dilepton event sample, which includes e^+e^-, $\mu^+\mu^-$, and $\tau^+\tau^-$ final states, is preselected. The preselection process rejects hadronic Z decays, cosmic muons, two-photon events, and beam-gas interactions. The selected dilepton events are then divided into hemispheres by the plane perpindicular to the event thrust axis, and particle identification algorithms are applied separately in each hemisphere in order to classify the τ decay mode. The particle identification is designed to be relatively independent of the energy of the τ decay products, thus keeping polarization biases to a minimum. Finally, remaining non-τ background is reduced by making cuts based on information in the hemisphere opposite to the selected decay.

The final sample consists of events for which at least one of the hemispheres is identified as one of the five channels described in Chapter 2. A summary of the number of selected events for each channel is given in Table 4.1. The selection efficiencies are estimated from Monte Carlo simulation of $Z \to \tau^+\tau^-$ events [27] including full simulation of the L3 detector response [28]. Backgrounds from non-τ sources are estimated predominantly from data, and crosschecked with Monte Carlo wherever possible. Background from other τ decays is estimated from Monte Carlo, and since this background contains polarization information it is fitted simultaneously with the signal. Details concerning background estimation and fitting can be found in Chapter 6.

This chapter contains descriptions of the preselection, the particle identification, and the final selection.

Channel	1990	1991	1992	1993	total
$\pi^-\nu_\tau$	220	1877	4484	4528	11109
$e^-\bar{\nu}_e\nu_\tau$	385	2448	5285	5568	13686
$\mu^-\bar{\nu}_\mu\nu_\tau$	558	2791	5646	5348	14343
$\rho^-\nu_\tau$	503	4138	8502	8617	21760
$a_1^-\nu_\tau$	-	569	1234	1102	2905
$Z \to q\bar{q}$	416000		678000	658000	1784000

Table 4.1: Number of τ decays selected for each channel.

4.1 Dilepton Preselection

$Z \to \tau^+\tau^-$ events are characterized by low track multiplicity and large boost of the τ decay products. τ's decay to one, three, or five charged particles, and, as a result of the large boost, angles between tracks in the same hemisphere are typically small. $Z \to$ hadrons decays, on the other hand, generally produce many tracks separated by larger angles. Figure 4.1 shows for comparsion a $Z \to \tau^+\tau^-$ candidate and a $Z \to$ hadrons candidate.

In accordance with these characteristics, the following cuts are used to reject $Z \to$ hadrons:

1. No more than 6 TEC tracks in an event.
2. No more than 5 TEC tracks in either hemisphere.
3. The maximum azimuthal angle between the thrust axis and any TEC track must be less than 20°.
4. Fewer than 20 BGO clusters.

It is estimated from Monte Carlo that these cuts reject more than 99.9% of $Z \to$ hadrons and less than 2% of dilepton events.

Cosmic muons are rejected using a combination of scintillator timing information and the DCA measurement from the TEC. Figure 4.2(a) shows the DCA distribution for events in which each hemisphere contains one muon chamber track matched to a TEC track. The bump centered at DCA = 0 is from $Z \to \mu^+\mu^-$ decays; its distribution corresponds to the intrinsic DCA resolution of the TEC

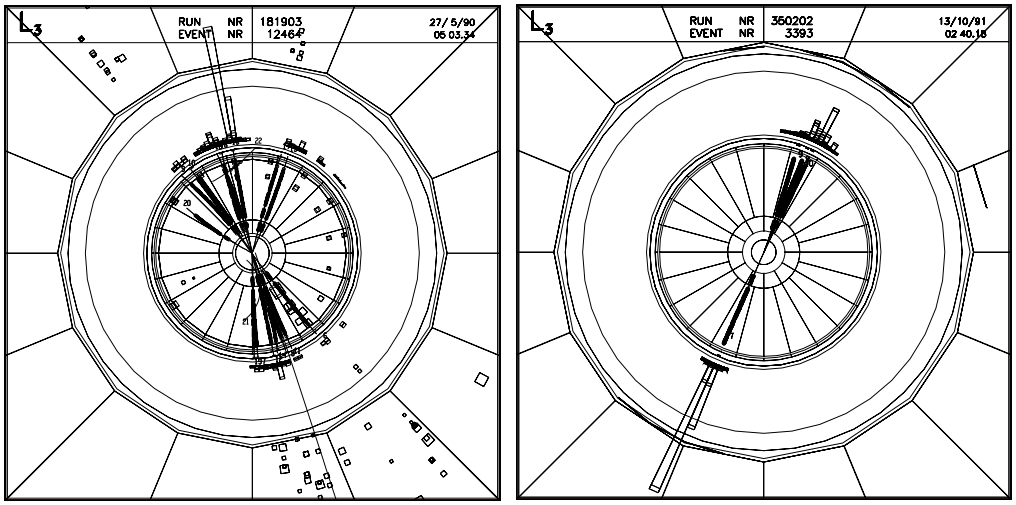

(a) Z $\rightarrow$ hadrons candidate.

(b) Z $\rightarrow \tau^+\tau^-$ candidate.

Figure 4.1: A Z $\rightarrow$ hadrons and Z $\rightarrow \tau^+\tau^-$ candidate.

convoluted with the beamspot profile. The flat sidebands are from cosmic muons, which are distributed evenly in DCA. At least one TEC track is required to satisfy $|\mathrm{DCA}| < 2$ mm in order for the event to be selected. This cut is relaxed for background estimation, as described in Chapter 6. Further cosmic rejection is achieved by requiring the scintillator matched a TEC track to register a hit within 2 ns of the time expected for events originating at the interaction point. Figure 4.2(b) shows the scintillator timing distribution for the same sample used to generate Figure 4.2(a).

The preselection also reduces background from $\mathrm{e^+e^-} \rightarrow \mathrm{e^+e^-}f^+f^-$ (two-photon) events. Typically the final state electrons in these events are scattered at low angles relative to the beam axis, and so remain undetected. In this case the momentum carried by the fermion pair is small, and tends to be directed along the beam axis. Background from events of this type is supressed by requiring acolinearity $< 20°$, at least one TEC track with $P_T > 0.5$ GeV, and by rejecting events that satisfy both of the following criteria:

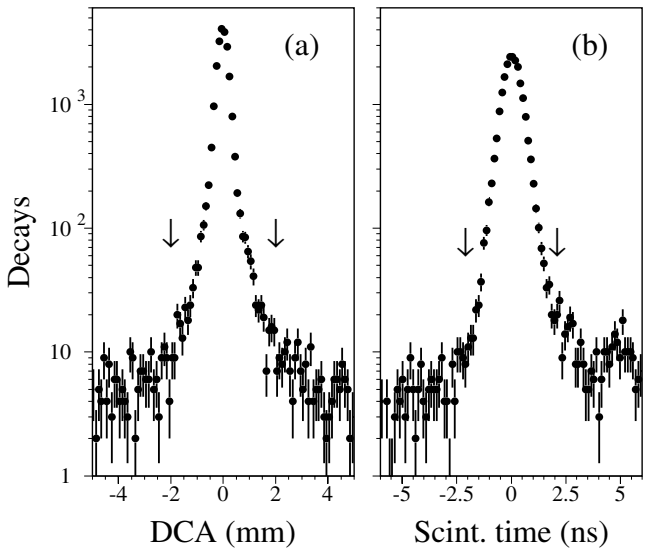

Figure 4.2: (a) DCA distribution from TEC for events with a muon identified in each hemisphere. The arrows show the location of the cuts used to reject cosmic rays. (b) Scintillator timing for the same sample use in (a). The arrows show the cuts used for cosmic rejection.

1. Total calorimetric energy less than 15 GeV.
2. $\left|P_T^{\text{track}-1}\right| - \left|P_T^{\text{track}-2}\right| < 1$ GeV.

Cut 2 is included to avoid rejecting $\tau^+\tau^-$ events with low visible energy, since for these events the momentum on the two sides tends to be unbalanced due to the large energy fraction carried by the neutrinos.

After preselection, the sample contains more than 98% of each of the charged leptonic decay modes of the Z. The background from cosmics, two-photon events, and $Z \rightarrow$ hadrons is estimated to be 5%.

4.2 Particle Identification

Each event that passes preselection is divided into two hemispheres by the plane perpendicular to the event thrust axis. Particle identification is then carried out separately in each of the hemispheres. It is desirable to minimize the use of en-

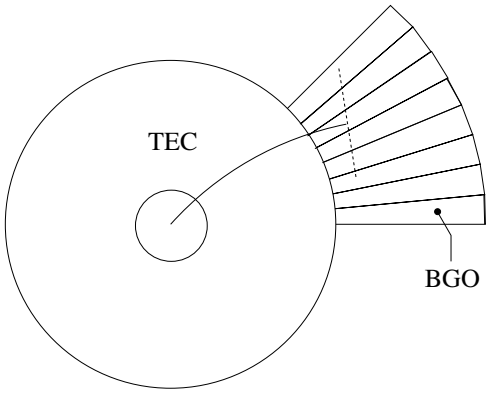

Figure 4.3: Illustration of an electron impacting the BGO showing the plane used for analysis of the transverse shower profile. The representations of the BGO and the TEC are not to scale.

ergy dependent cuts in all phases of the selection, since the energy spectrum is senstitive to polarization. Any energy dependence of the selection efficiency which is not faithfully reproduced by the Monte Carlo can introduce a polarization bias, particularly in regions where the polarization sensitivity is high. We therefore use the spatial relationship between tracks and energy deposition in the calorimeters as well as the geometrical distribution of the the energy deposition to discriminate between particle types. This approach is found to be relatively independent of energy.

The signature for a $\tau^- \rightarrow e^- \bar{\nu}_e \nu_\tau$ decay is a track in the TEC matched to a narrow, symmetric shower in the BGO and little or no energy in the hadron calorimeter. $\tau^- \rightarrow \pi^- \nu_\tau$ decays, in contrast, produce wide and typically asymmetric showers in the BGO as well as energy clusters in the hadron calorimeter. $\tau^- \rightarrow \rho^- \nu_\tau$ decays produce overlapping hadronic and electromagnetic showers in the BGO as well as hadron calorimeter energy. In this case, the center of the electromagnetic shower from the π^0 is displaced from the charged pion track. $\tau^- \rightarrow \mu^- \bar{\nu}_\mu \nu_\tau$ decays are identified by tracks in the muon spectrometer and minimum ionizing signatures in the hadron calorimeter. These distinct signatures form the basis of the selection.

4.2.1 Electromagnetic and hadronic shower profiles

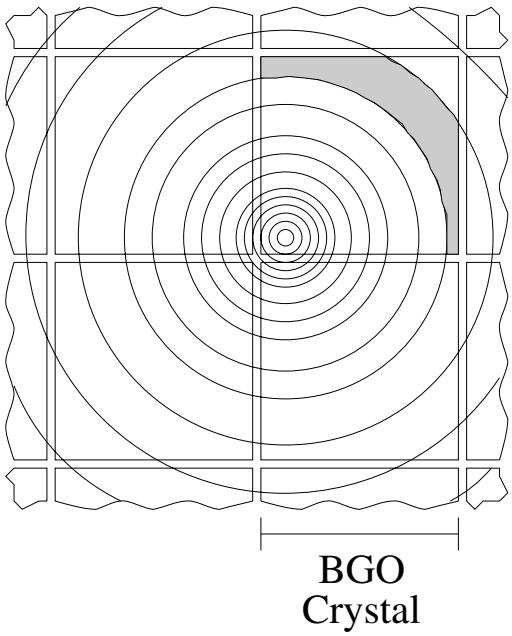

Figure 4.4: Concentric rings used for estimation of expected energy in a BGO crystal from an electromagnetic shower at the one-radiation length plane.

The electron and neutral pion identification algorithms described in subsequent sections rely on the ability to identify electromagnetic showers in the BGO and use their characteristic transverse profile in calculating energies and impact points. Furthermore the reconstruction of neutral pions in the presence of a charged hadron requires separating the BGO energy deposition due to the charged hadron from that of the neutral pion(s) (see section 4.2.3), which in turn requires knowledge of the average hadronic shower profile. To these ends, a method was developed for comparing the observed energy distribution in the BGO with that expected for an electromagnetic or hadronic shower of a given energy impacting the BGO at a given point [37].

The method for calculating the expected transverse energy distribution produced by an electron is outlined in Figures 4.3 and 4.4. The extrapolated electron track defines the center of the electromagnetic shower, and the shower profile is evaluated in the plane perpendicular to the track projected one radiation length

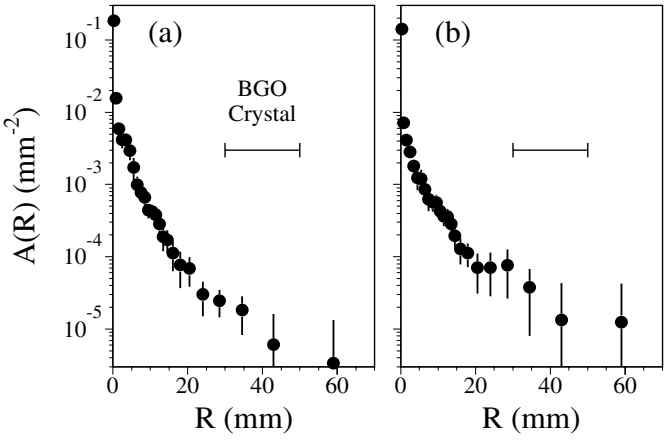

Figure 4.5: (a) Electromagnetic shower profile. The quantity $A(R)$ is the normalized energy density. The length of a side of a BGO crystal's front face is shown for comparison. (b) Hadronic shower profile.

into the BGO, as depicted in Figure 4.3. The expected energy in a crystal is computed by summing the energies in concentric annular regions contained in the crystal and centered at the impact point,

$$Q_i = \sum_j S_j A(R_j) \tag{4.1}$$

where Q_i is the expected fractional energy in the i'th crystal, S_j is the area of the j'th annular region in the crystal, $A(R_j) = \frac{1}{E}\frac{dE}{dS}$ is the fractional energy density for that region, and R_j is the distance from the impact point. This is illustrated in Figure 4.4, in which the shaded region represents, for example, region j in the discussion above.

The form of the radially dependent energy density $A(R_j)$ is characteristic of an electromagnetic shower, and was determined using a sample of bhabha events. For each electron in the bhabha sample, the energy in the 3×3 matrix of BGO crystals surrounding the shower maximum was measured, and the following quantity was computed,

$$F = \sum_j \sum_{i=1}^{9} \left(E_{ij} - \frac{1}{2} E_{\rm beam} Q_{ij} \right)^2 \tag{4.2}$$

where j runs over all the electrons in the sample, E_{ij} is the measured energy in the i'th crystal for the j'th electron, and where the expected normalized energy Q_{ij} is given by,

$$Q_i = \sum_{k=1}^{N_r} A_k S_k \tag{4.3}$$

where again A_k and S_k are the energy densities and areas respectively for the k'th annular region in crystal i. F was then minimized to determine the N_r free parameters A_k, which define the shower profile.

From a test beam study [38], the shower shape was found to be relatively independent of energy above 1 GeV. Figure 4.5(a) shows the transverse electromagnetic shower profile derived from the data.

An average hadronic shower profile was derived from Monte Carlo using the technique outlined above [39]. The result is shown in Figure 4.5(b).

4.2.2 Electron Identification

Electrons characteristically produce narrow, symmetric showers in the BGO calorimeter, and are generally well matched to a track in the TEC. Figure 4.6 shows a comparison of an electron candidate with a pion candidate. In constrast to the electron, the pion produces a wide, asymmetric shower and also deposits energy in the hadron calorimeter behind the shower.

An electromagnetic χ^2, $\chi^2_{\rm EM}$, is constructed to quantify the compatability of the observed shower profile with that expected from an electron (or photon),

$$\chi^2_{\rm EM} = \sum_{i=1}^{9}\sum_{j=1}^{9} \frac{(E_i - Q_i)\,(E_j - Q_j)}{V_{ij}^{-1}} \tag{4.4}$$

where E_i is the energy fraction measured in the i'th crystal, Q_i is the expected energy fraction defined in equation 4.1, and the V_{ij}^{-1} are the elements of the inverse covaraiance matrix. The covariance matrix is measured from the bhabha sample. The sums are taken over the 3×3 matrix of crystals surrounding the shower maximum.

A hemisphere is considered to contain an electron candidate if the following criteria are satisfied:

1. $\chi^2_{\rm EM} < 20$ for 8 degrees of freedom.

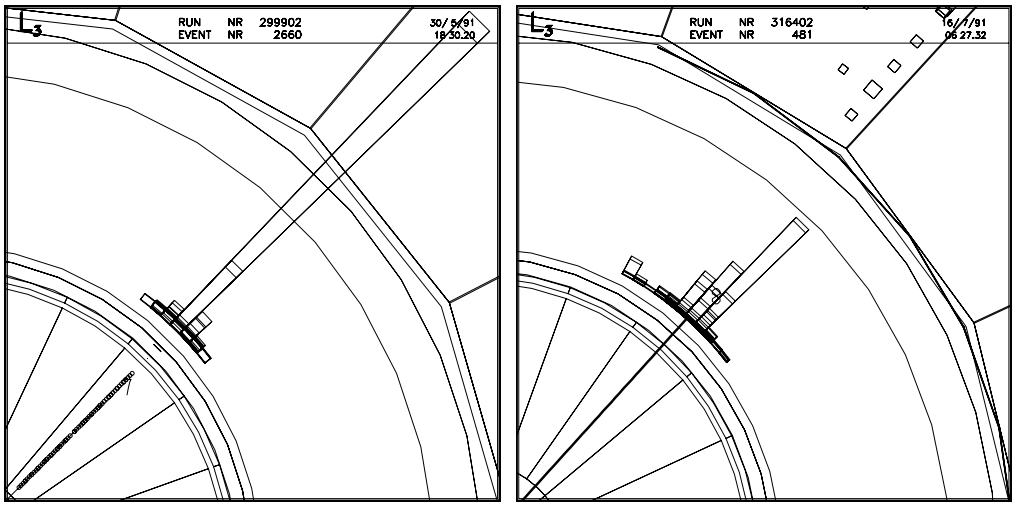

(a) An electron candidate.

(b) A pion candidate.

Figure 4.6: Comparison of electron and pion candidates, showing their characteristic profile in the BGO calorimeter, the relationship between the TEC track and shower maximum, and the energy deposition in the hadron calorimeter.

2. The angle between the track and the center of gravity of the shower must be less than 10 mrad in $r-\phi$ and 20 mrad in z (see Figure 4.7).

3. The probability that the momentum measured by the TEC and the energy observed in the BGO arise from a single particle must exceed 0.0005. This probability is computed in a manner analogous to the method described in section 5.5.

4. The energy deposition in the hadron calorimeter behind the shower must be consistent with the tail of an electromagnetic shower.

All of these cuts reject hadronic τ decays. In cut 2 the different thresholds on the $r-\phi$ and θ cuts reflect the different resolutions associated with the measurement of these two angles.

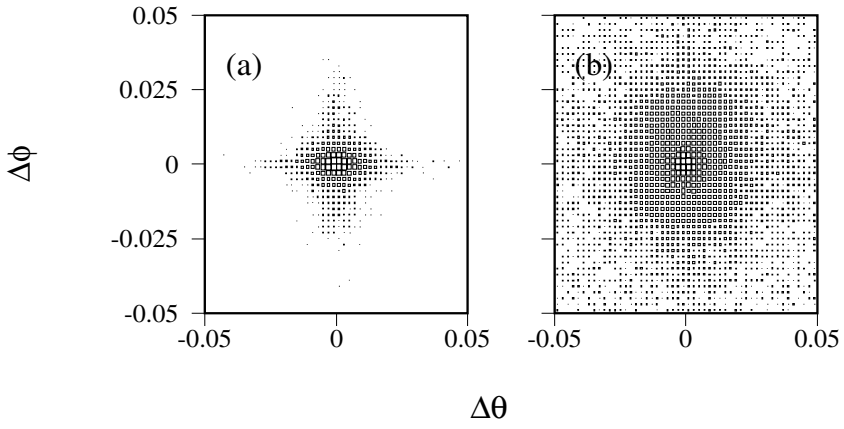

Figure 4.7: θ and ϕ angles between the track and center of gravity of the shower for a) events with electromagnetic energy deposition above 40 GeV in each hemisphere (mostly bhabhas), and b) dilepton events with electromagnetic and muon energy below 40 GeV in each hemisphere.

4.2.3 π^0 identification in hadronic τ decays

The decay modes $\tau^- \to \pi^-\nu_\tau$, $\tau^- \to \rho^-\nu_\tau$, and $\tau^- \to a_1^-\nu_\tau \to 2\pi^0\pi^-$ are distinguished from one another by the number of neutral pions accompanying the charged pion. Furthermore, the kinematic variables used to determine the polarization depend on the energy sharing between the charged and neutral pions. Since the boost from the τ is large, the decay products in these channels are separated by angles in the neighborhood of 40-100 mrad and produce overlapping energy clusters in the BGO. Thus in order to discriminate among the various hadronic decay modes, and to compute the polarization sensitive kinematic variables, it is necessary to separate the contributions to BGO energy deposition from charged hadrons and from photons produced by π^0 decays.

Monte Carlo studies show that the separation between the π^- and nearest photon produced in $\tau^- \to \rho^-\nu_\tau$ decays is typically two BGO crystals (about 90 mrad), and hadronic shower profile analysis indicates that most of the energy from a charged hadron is deposited in the impacted crystal and its nearest neighbors (see Figure 4.5(b)). These observations indicate that separation of hadronic and electromagnetic showers in the BGO is possible. Figure 4.8 shows an event picture with a $\tau^+ \to \rho^+\nu_\tau$ candidate recoiling against a $\tau^- \to \pi^-\nu_\tau$ candidate. The $\tau^+ \to \rho^+\nu_\tau$ hemisphere exhibits several characteristics of a $\rho^+ \to \pi^+\pi^0$ decay, including a

charged track from the π^+ offset from a BGO crystal which registers a large energy deposition, a wide BGO shower shape inconsistent with an electromagnetic profile, and significant energy in the hadron calorimeter.

An algorithm for reconstructing overlapping energy clusters from one charged hadron and several photons has been developed. It incorporates information from the TEC track and the BGO crystals which fall within the 30° half-angle cone around the track:

1. The TEC track is extrapolated to the BGO in order to determine the charged hadron impact point (Figure 4.9(a)).

2. A hadronic shower profile is normalized to the central crystal in the charged hadron cluster, determined in step 1. The contribution from the charged hadron to the energies observed in neighboring crystals is estimated (Figure 4.9(b)).

3. The estimated energy deposition due to the charged hadron is subtracted from the observed energy in crystals around the impact point (Figure 4.9(c)). Remaining local maxima become neutral cluster candidates.

4. The positions and energies of the neutral cluster(s) are defined by fitting the observed energy distributions with electromagnetic shower profiles. Clusters that fit better with the sum of two profiles are split.

5. The fitted shower profiles from step 4 are used to subtract the estimated energy contributions from photons to the observed energy near the charged cluster (Figure 4.9(d)). A new estimate is thus obtained for the energy deposited in the central crystal by the charged hadron.

Steps 2-4 are iterated until all reconstructed particle energies are stable to 1%. Typically tree to four iterations are required.

Figure 4.10 shows the number of neutral clusters reconstructed in the data and in the Monte Carlo one-prong hadronic samples using the algorithm above. This sample includes all hemispheres with no identified electron or muon. Also shown is a breakdown by decay channel of the number of neutral clusters found in the Monte Carlo. As expected, the majority of $\tau^- \to \pi^-\nu_\tau$ decays produce no neutrals, whereas $\tau^- \to \rho^-\nu_\tau$ decays usually produce one or two neutrals. Note however that $\tau^- \to \pi^-\nu_\tau$ decays sometime produce one or more reconstructed neutrals,

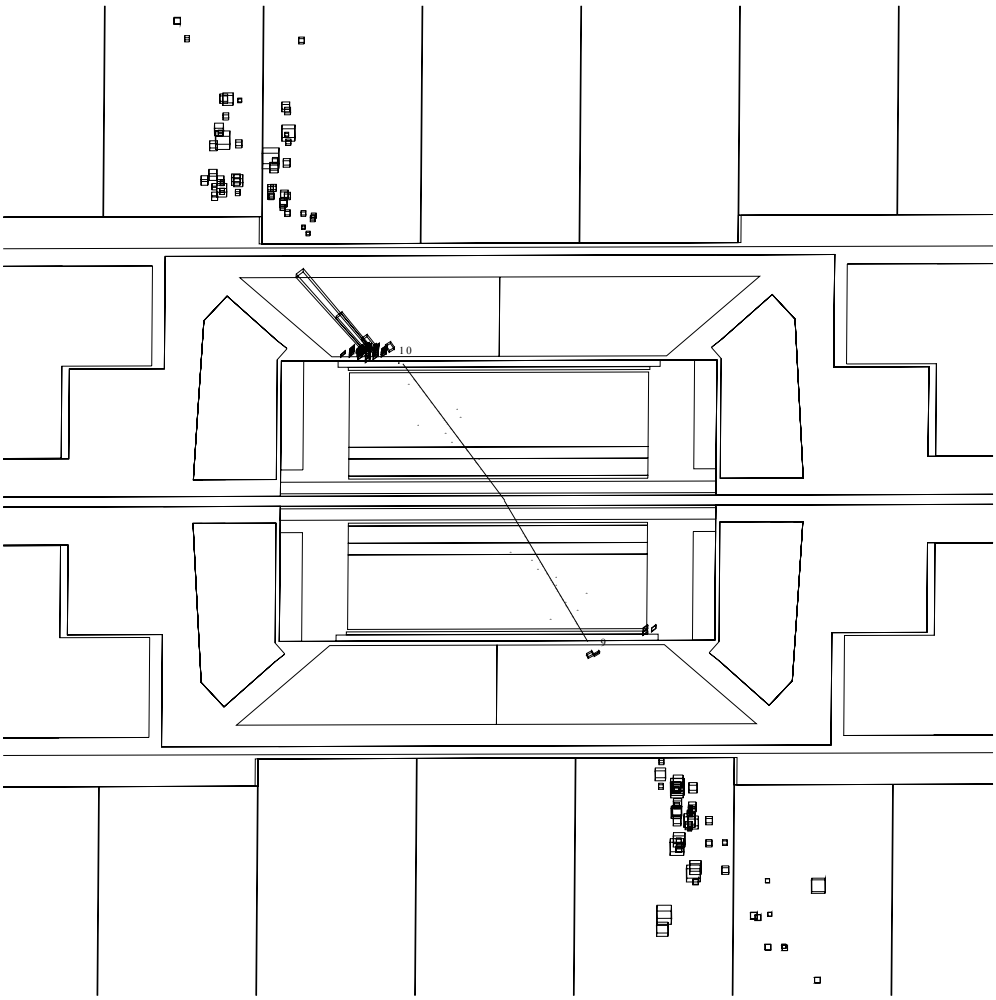

Figure 4.8: Event picture showing a $\tau^- \to \pi^- \nu_\tau$ candidate in the lower hemispere and a $\tau^+ \to \rho^+ \nu_\tau$ candidate in the upper hemisphere.

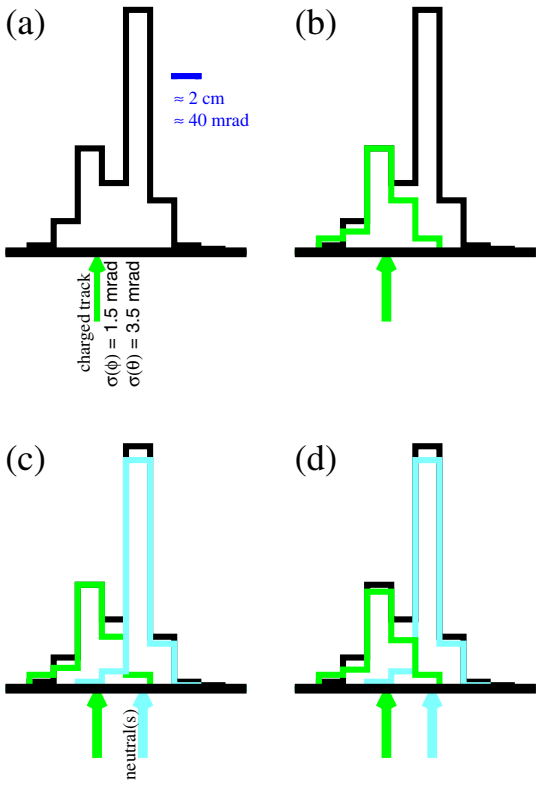

Figure 4.9: Illustration of the procedure used to determine the energies of one charged hadron and several photons from overlapping clusters in the BGO.

and similarly $\tau^- \to \rho^- \nu_\tau$ decays can produce three or more neutrals. Remaining hadronic τ decays are accompanied by more than one π^0 as reflected in the figure.

After charged and neutral clusters are reconstructed, neutral pions are identified. A single neutral cluster forms a π^0 candidate if the cluster energy exceeds 1 GeV and if $\chi^2_{\rm EM} < 20$ for 8 degrees of freedom, or if the invariant mass determined by fitting two electromagnetic shower shapes to the neutral cluster is within 50 MeV of the π^0 mass. Two separate neutral clusters form a π^0 candidate if their invariant mass is within 40 MeV of the π^0 mass. Figure 5.23 shows the reconstructed π^0 invariant mass for data and Monte Carlo.

Next, the energy due to photons and neutral pions is subtracted from the total energy deposition around the track, and the remainder is assigned to the charged

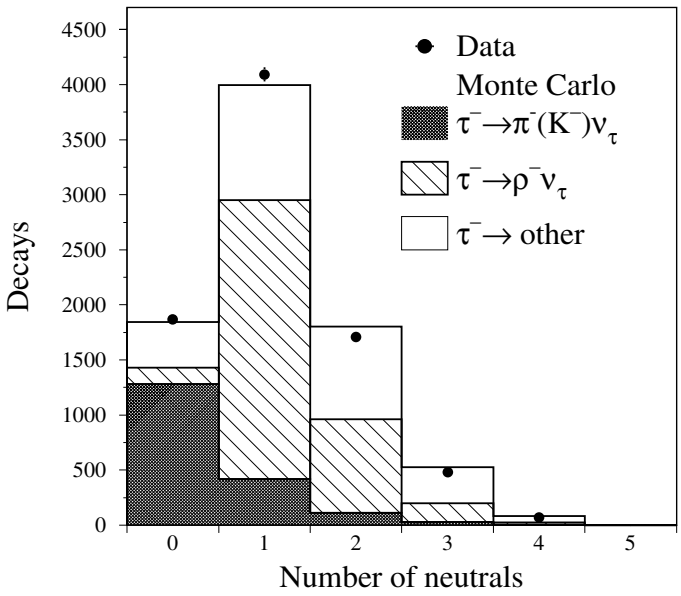

Figure 4.10: Number of neutral clusters reconstructed in data and Monte Carlo. The sample includes all hemispheres with no identified electron or muon. $\tau^- \to$ other includes all the one-prong hadronic τ decays which are not $\tau^- \to \pi^-\nu_\tau$ or $\tau^- \to \rho^-\nu_\tau$.

hadron. This is combined with the energy measured by the hadron calorimeter to determine the total charged hadron energy. Finally, the TEC measurement of the charged hadron momentum is combined with the energy measurement from the calorimeters using the technique described in section 5.5.

4.2.4 Muon identification

Muons are identified based on information either from the muon chambers or from a combination of the TEC and the calorimeters. In the first case, a track in the muon chambers constitutes a muon candidate if it extrapolates to the interaction region. Figure 4.11 illustrates the motivation behind this requirement. The left hemisphere of the event shown in the picture has significant energy deposition in the hadron calorimeter, typical of a hadronic shower; the muon chamber track behind it is a result of incomplete containment of the shower and does not point back to the interaction region. The second method for muon identification exploits

the minimum ionizing signature of muons in the hadron calorimeter; the right hemisphere in Figure 4.11 shows a TEC track (and muon chamber track) matched to a such a minimum ionizing signature. Also note that the muon chamber track points to the event vertex.

The compatability of the energy deposition in the hadron calorimeter with that expected from a muon is quantified in the following way. A straight line is fitted to the energy distribution in the calorimeter, and a list is compiled of all the proportional chambers which the line intersects. The average energy expected from a minimum ionizing particle is computed for each of the chambers in the list. The chambers in the list are then grouped into readout towers so that they can be compared to the pattern of hits in the data, and the number of measured hits on the line, $N_{\rm meas}$, and the number of missed hits, $N_{\rm miss}$, are recorded. The measured energies are used together with the expected energies for a minimum ionizing particle to compute a quantity $\chi^2_{\rm MIP}$,

$$\chi^2_{\rm MIP} = \frac{1}{N_{\rm meas}} \sum_{i=1}^{N_{\rm meas}} \left(\frac{E_{\rm meas} - E_{\rm MIP}}{E_{\rm MIP}} \right)^2 \tag{4.5}$$

where $E_{\rm meas}$ is the measured energy and $E_{\rm MIP}$ is the expected energy deposited by a minimum ionizing particle. The error term on the right hand side of equation 4.5 is set to $E_{\rm MIP}$ since, as described in section 5.5, the calorimetric energy resolution has the form $\sigma_E \propto \sqrt{E}$. Minimum ionizing particles tend to follow a straight trajectory through the hadron calorimeter, so that a large fraction of the cells along the line register hits. Hadrons, on the other hand, interact strongly in the hadron calorimeter absorber plates so energy deposition is spread over a wide area, and consequently the number of hit cells along the line is small. Also $\chi^2_{\rm MIP} \approx 1$ for a minimum ionizing particle, and $\chi^2_{\rm MIP} \gg 1$ for hadronic showers. Figure **??** shows $\chi^2_{\rm MIP}$ for all the preselected dilepton events and for events with muons identified by the muon spectrometer.

A muon candidate must then satisfy either the criteria for identification based on the muon chambers,

1. A reconstructed muon chamber track with at least 2 P segments and 1 Z segment.

2. The track must point to the vertex to within 5σ of the muon chamber DCA resolution. This corresponds to 500 mm in z and 70 mm in $r-\phi$ for tracks with $E_\mu > 20$ GeV. At lower energies, the cut on $r-\phi$ DCA is less stringent.

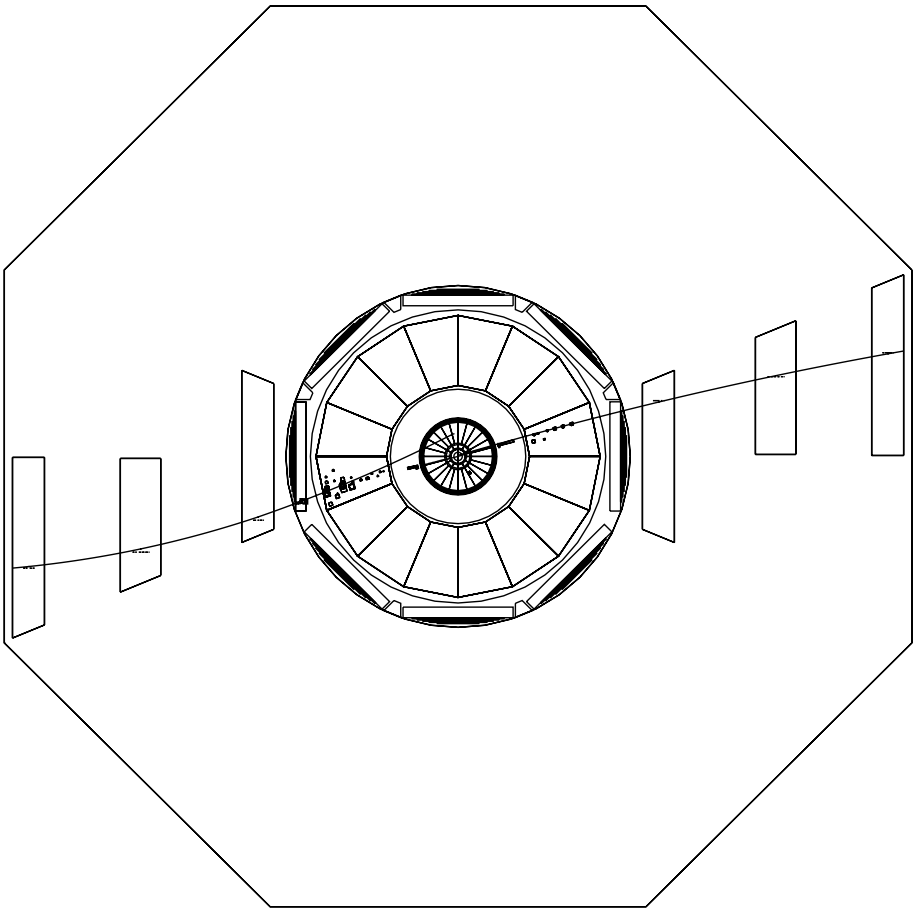

Figure 4.11: A Z $\rightarrow \tau^+\tau^-$ event with a muon candidate in the right hemisphere. The left hemisphere contains a hadronic decay which produced a track in the muon chambers. This track does not extrapolate back to the vertex, indicating it is not produced by a muon.

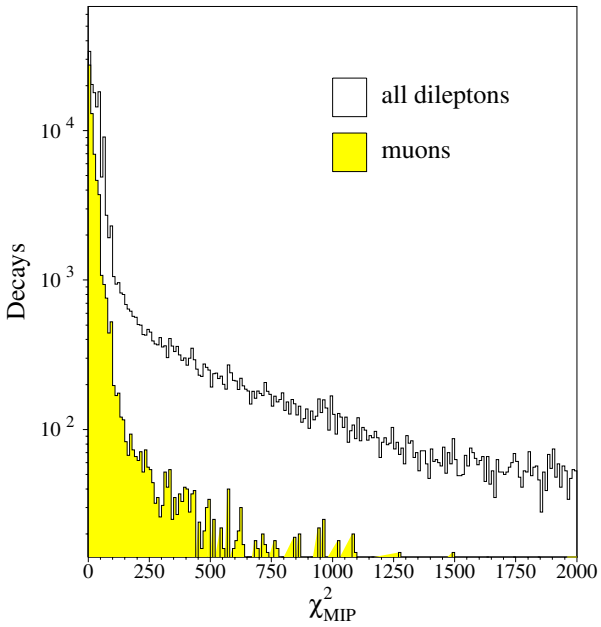

Figure 4.12: χ^2_{MIP} for all hemispheres in the dilepton sample, and for events with tracks in the muon spectrometer.

or the criteria for identification based on the TEC and the calorimeters:

1. a TEC track matched to within 100 mrad in $r-\phi$ and z to the energy deposition in the calorimeters.

2. $\chi^2_{\mathrm{MIP}} < 500$

3. $N_{\mathrm{meas}}/\left(N_{\mathrm{meas}}+N_{\mathrm{miss}}\right) \geq 0.5$

4. Energy in the BGO < 1 GeV (a MIP deposits about 260 MeV in BGO).

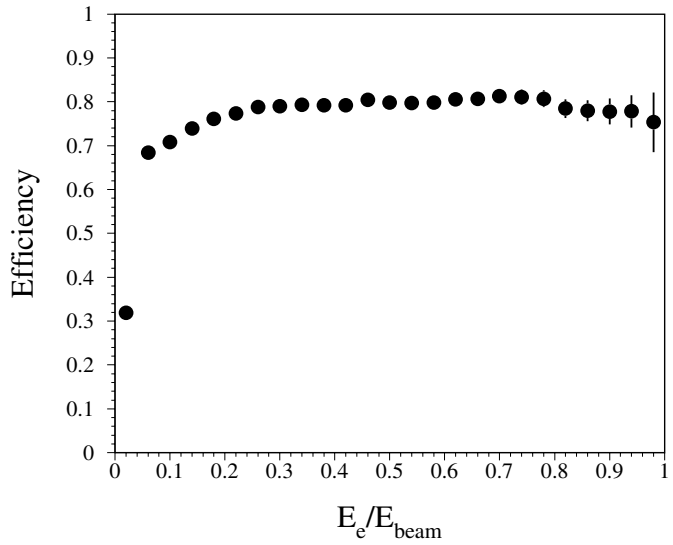

Figure 4.13: Selection efficiency for $\tau^- \to e^- \bar{\nu}_e \nu_\tau$ in the fiducial volume. The decrease in efficiency at low energy is a result of the energy cuts used to reject two-photon background.

4.3 Selection

4.3.1 Selection of $\tau^- \to e^- \bar{\nu}_e \nu_\tau$

Selection of $\tau^- \to e^- \bar{\nu}_e \nu_\tau$ decays is limited to the barrel region of the BGO, $|\cos\theta| < 0.7$. Electron selection was not pursued in the endcaps because the high cross section for $e^+e^- \to e^+e^-$ events in this region presents formidable background problems.

A decay is identified as $\tau^- \to e^- \bar{\nu}_e \nu_\tau$ if it meets the requirements described in section 4.2.2 and if it is not identified as an electron from $Z \to e^+e^-$. Events meeting either the following criteria are considered $Z \to e^+e^-$:

1. An identified electron in each hemisphere and total energy in the BGO $> 80\%$ of the beam energy.

2. An identified electron in the hemisphere opposite to the selected decay with $E_e > 42$ GeV.

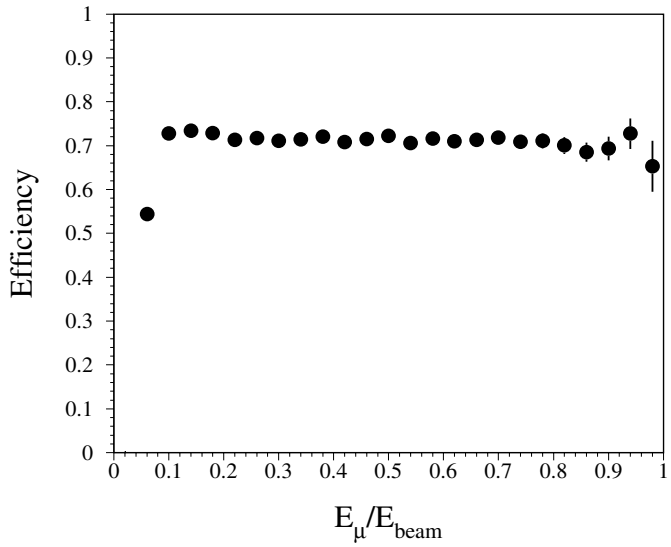

Figure 4.14: Selection efficiency for $\tau^- \to \mu^- \bar{\nu}_\mu \nu_\tau$ in the fiducial volume. The decrease in efficiency at low energies is a result of both the energy cut used to reject two-photon events and energy loss in the calorimeters. The precipitous drop at $E_\mu/E_{\rm beam} \approx 0.04$ is a consequence of the roughly 2 GeV deposited by muons in the calorimeters.

3. An identified electron in the hemisphere opposite to the selected decay whose energy cannot be reliably measured.

Cut 3 rejects events with an electron opposite the selected hemisphere which impacts the BGO in the vicinity of one or more dead crystals or the edge of the fiducial volume.

The selection efficiency for $\tau^- \to e^- \bar{\nu}_e \nu_\tau$ is shown in Figure 4.13. The backgrounds are estimated to be 1.5% from other τ decays, 1.2% from two-photon interactions, and 1.6% from $Z \to e^+e^-$ events[1].

[1]Selection efficiencies quoted here and in subsequent sections correspond to the combined 1991-1993 sample.

4.3.2 Selection of $\tau^- \to \mu^- \bar{\nu}_\mu \nu_\tau$

The $\tau^- \to \mu^- \bar{\nu}_\mu \nu_\tau$ selection requires that both the muon chamber and hadron calorimeter criteria described in section 4.2.4 be fulfilled in the given hemisphere. Dimuons are rejected by cutting events for which any of the following is present:

1. An identified μ opposite to the selected hemisphere with energy $E_\mu > 40$ GeV.
2. An identified μ opposite to the selected hemisphere whose energy is not measured.

Condition 2 can result if the μ opposite to the selected hemisphere does not produce a track in the muon chambers, but is nontheless identified based on TEC and hadron calorimeter information.

Figure 4.14 shows the selection efficiency for $\tau^- \to \mu^- \bar{\nu}_\mu \nu_\tau$. The average efficiency in the fiducial volume is 70%. The background contributions are estimated to be 1.0% from other τ decays, 0.8% from two-photon interactions, 0.3% from cosmics, and 3.1% for $\mathrm{Z} \to \mu^+ \mu^-$ events.

4.3.3 Selection of $\tau^- \to \pi^- \nu_\tau$

Hemispheres which are not identified as $\tau^- \to \mathrm{e}^- \bar{\nu}_\mathrm{e} \nu_\tau$ or $\tau^- \to \mu^- \bar{\nu}_\mu \nu_\tau$ are considered for the $\tau^- \to \pi^- \nu_\tau$ selection. The decay is rejected if either of the following is present:

1. An identified muon or electron opposite to the selected hemisphere with $E_{\mathrm{e},\mu} > 42$ GeV.
2. An identified muon or electron opposite to the selected hemisphere whose energy cannot be reliably measured.

These two cuts reject background from $\mathrm{Z} \to \mu^+ \mu^-$ and $\mathrm{Z} \to \mathrm{e}^+ \mathrm{e}^-$ events in which the electron or muon on the selected side is misidentified as a pion. Decays which survive these cuts are selected if they fulfill the following criteria:

1. The probability that the momentum measured by the TEC and the energy observed in the calorimeters arise from the same particle must exceed 0.003 (see equation 5.6).
2. There are no π^0 or photon candidates with energy $E > 0.5$ GeV in the same hemisphere.

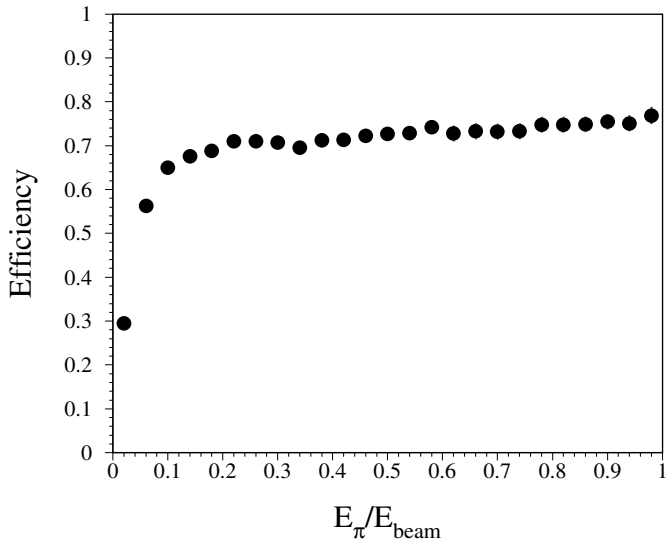

Figure 4.15: Selection efficiency for $\tau^- \to \pi^-\nu_\tau$ in the barrel.

The second cut rejects $\tau^- \to \rho^-\nu_\tau$ and $\tau^- \to a_1^-\nu_\tau$ decays, since fluctuations in the hadron shower from $\tau^- \to \pi^-\nu_\tau$ decays can result in low energy neutral clusters whereas $\tau^- \to \rho^-\nu_\tau$ and $\tau^- \to a_1^-\nu_\tau$ decays typically produce higher energy photon or π^0 candidates.

The barrel selection efficiency for $\tau^- \to \pi^-\nu_\tau$ is 72% and is shown in Figure 4.15. The efficiency in the endcaps is 64%. The background in the barrel is 11.4% from other τ decays, 1.4% from bhabhas, 1.4% from two-photon events, and 0.9% from dimuons. The corresponding backgrounds in the endcaps are 16%, 10%, 1.5% and 5%.

4.3.4 Selection of $\tau^- \to \rho^-\nu_\tau$

Hemispheres which are not identified as $\tau^- \to \mu^-\bar{\nu}_\mu\nu_\tau$ or $\tau^- \to e^-\bar{\nu}_e\nu_\tau$ are considered for the $\tau^- \to \rho^-\nu_\tau$ selection. The cuts for dimuon and bhabha rejection are identical to those used in the case of $\tau^- \to \pi^-\nu_\tau$. A decay then constitutes a $\tau^- \to \rho^-\nu_\tau$ candidate if the following criteria are all fulfilled:

1. The probability that the calorimetric energy assigned to the charged hadron and the momentum measure by the TEC originate from the same particle

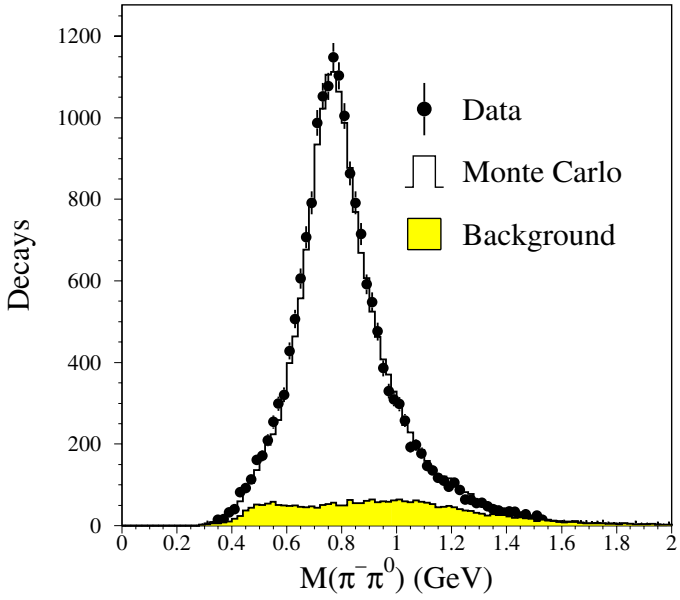

Figure 4.16: Invariant mass of the $\pi^-\pi^0$ system for selected $\tau^- \to \rho^-\nu_\tau$ decays, excluding cut 3 of section 4.3.4.

must exceed 0.001.

2. Exactly 1 π^0 candidate in the selected hemisphere.

3. The invariant mass of the $\pi^-\pi^0$ system must be in the range 0.45-1.20 GeV.

Cut 1 is not as stringent as the corresponding cut for the $\tau^- \to \pi^-\nu_\tau$ channel since for $\tau^- \to \rho^-\nu_\tau$ the calorimetric energy has contributions from the charged and neutral pions whereas the track momentum is a measure of the charged pion momentum alone. The invariant mass of the $\pi^-\pi^0$ system for selected $\tau^- \to \rho^-\nu_\tau$ decays (excluding cut 3) is shown in Figure 4.16. The selection efficiency in the barrel as a function of $\cos\theta^*$ and $\cos\psi^*$ is shown in Figure 4.17. The average efficiency is 70% in the barrel and 51% in the endcaps. Background in the barrel is 10.2% from other τ decays, 0.2% from bhabhas, 0.5% from dimuons. The corresponding figures in the endcaps are 14.3%, 1.5%, and 1.5%.

4.3.5 Selection of $\tau^- \to a_1^-\nu_\tau$

One-prong $\tau^- \to a_1^-\nu_\tau$ decays are preselected according to the following criteria:

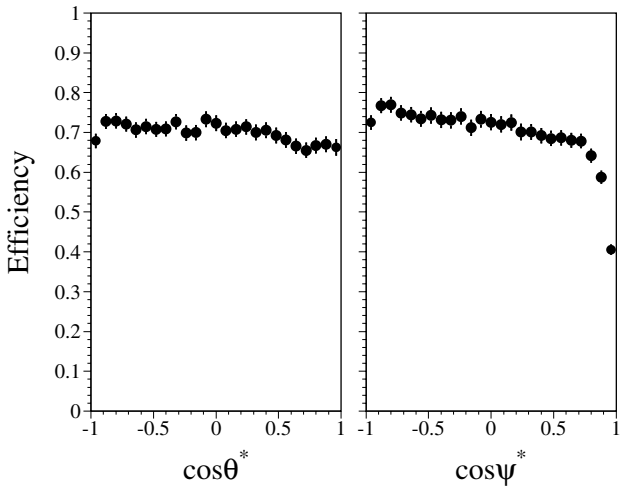

Figure 4.17: Selection efficiency for $\tau^- \to \rho^- \nu_\tau$ as a function of $\cos\theta^*$ and $\cos\psi^*$. These figures correspond to the fiducial region in the barrel. For $\cos\psi^* = 1$ the charged and neutral pions are colinear in the lab frame, and the charged pion has maximal energy. The result is a large hadronic shower in the BGO which fully overlaps with a relatively small electromagnetic shower from the π^0. In this enviroment the effectiveness of the neutral cluster reconstruction algorithm is reduced, and this the source of the efficiency drop as $\cos\psi^*$ approaches 1. There is no similar problem at $\cos\psi^* = -1$ since in this case the π^0 carries maximal energy and the charged pion produces only a small shower in the BGO.

1. Two π^0 candidates present in the selected hemsiphere.

2. If the two π^0 candidates each consists of a single neutral cluster, then the clusters must have an invariant mass inconsistent with the π^0 mass.

3. The probability that the calorimetric energy assigned to the charged hadron and the momentum measure by the TEC originate from a single particle must exceed 0.001.

The preselected sample is then subjected to a neural network selection [48] which further supresses background due to $\tau^- \to \rho^- \nu_\tau$ and $\tau^- \to \pi^-\pi^0\pi^0\pi^0\nu_\tau$ decays. The input to the neural network includes the energies of the charged pion and identified neutral clusters and the invariant masses of their combinations. The

selection efficiency is 33% in the fiducial region. Background from other τ decays is 28%; background from non-τ sources is negligible.

Chapter 5

Resolution and Energy Scale

Since the energy distributions of τ decay products are used to infer the polarization, any uncertainty in the energy is transformed to uncertainty in the polarization. Energy resolution affects primarily the statistical error on the polarization, but may also introduce a polarization bias if it is not properly modeled. Uncertainty in the energy scale also contributes to the systematic error. Systematic uncertainties in the energy scales of the various subdetectors may consist of scale offsets or nonlinearity in detector response. The qualitative effects of energy scale uncertainties on the polarization measurement are outlined in section 2.6.

The transverse momentum resolution for charged particles is especially important for measurement of the forward-backward polarization asymmetry. As discussed in detail in section 2.6.4, a mismeasurement of the charge due to finite resolution in the central tracking causes a misassignment of the polar angle, θ, which in turn distorts the shape of the $\mathcal{P}_\tau(\cos\theta)$ curve. In order to correct for this effect, the momentum resolution must be determined as a function of polarization sensitive variables like momentum and polar angle. Similarly, the accuracy with which the resolution function is known dictates the size of the systematic error associated with this quantity.

In this chapter we describe the techniques used to extract the TEC momentum resolution function from data, and discuss the checks used to verify the energy scales of the different subdetectors.

5.1 TEC resolution

In section 5.1.1 below we describe the general features of the TEC transverse momentum resolution and motivate the choice of variables that enter the resolution parameterization. This is followed by two sections describing the improvement in resolution that can be attained by removing problematic regions near the TEC endflange from consideration and by including the fill vertex in the fit for transverse momentum (sections 5.1.2 and 5.1.3 respectively). Finally the parameterization methods and results are presented in sections 5.1.4 and 5.1.5 for the barrel and endcap regions respectively.

The term "barrel" will be used throughout to describe the region $|\cos\theta| < 0.82$ and "endcap" for the region $|\cos\theta| > 0.82$. The delineation is chosen in this way so that the barrel corresponds to the angular range for which there is muon chamber coverage. This is a convenient distinction for purposes of measuring the TEC resolution, and also approximately corresponds to the polar angle dividing the barrel and endcap elements of the calorimeters.

5.1.1 General features of TEC resolution

The radius of curvature (R), distance of closest approach to a reference point (DCA), and azimuthal angle ϕ at the vertex for a track in the TEC are determined by fitting a circle to the reconstructed space points associated with the track [33], where the space points are computed from the position of the hit anodes and the measured drift times, as described in Chapter 3. These parameters are shown in Figure 5.1.

The curvature and angle ϕ are important for the τ polarization measurement. ϕ is used in matching TEC tracks to energy deposition in the calorimeters, a crucial part of the particle identification schemes described in Chapter 4. The ϕ measurement is also needed for computation of the polarization sensitive quantities used in the $\tau^- \to \rho^-\nu_\tau$ and $\tau^- \to a_1^-\nu_\tau$ channels. The curvature measurement is incorporated in the charged pion energy determination, described in section 5.5, and is used to assign charge in the $\mathcal{P}_\tau(\cos\theta)$ measurement[1].

We now motivate the choice of variables used in parameterizing the resolution. Since the distance from an anode to a point associated with a track is derived from

[1] This is strictly true only for events in which neither τ decays to a muon, since in these cases the charge is assigned by the muon chambers.

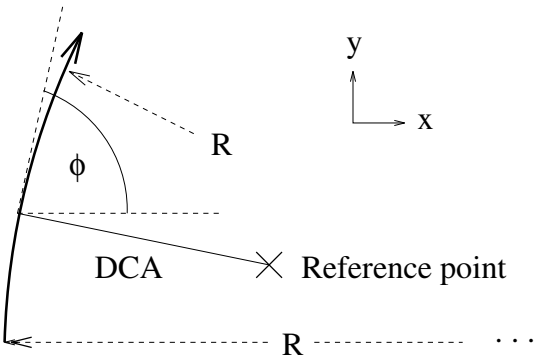

Figure 5.1: Definition of track parameters ϕ, R, and DCA.

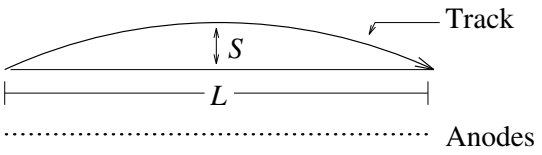

Figure 5.2: Definition of the sagitta S and lever arm L. The picture is not to any particular scale.

a measured drift time, we expect this distance to be normally distributed around its true value. Thus the measured track sagitta, defined in Figure 5.2, is normally distributed. The sagitta is related to transverse momentum by,

$$S \approx \frac{1}{P_T}\left(0.2997 \times 10^{-3}\frac{\mathrm{GeV}}{\mathrm{T-mm}}\right)\frac{BL^2}{8} \tag{5.1}$$

where L is the lever arm, also defined in Figure 5.2, B is the magnetic field parallel to the beam direction, and P_T is the momentum transverse to the beam direction. Equation 5.1 assumes that $S \ll L$ and $S \ll R$, both quite reasonable since, for example, at $P_T = 1$ GeV, $S \approx 1.4$ mm, whereas $R \approx 6.7$ m and L remains fixed

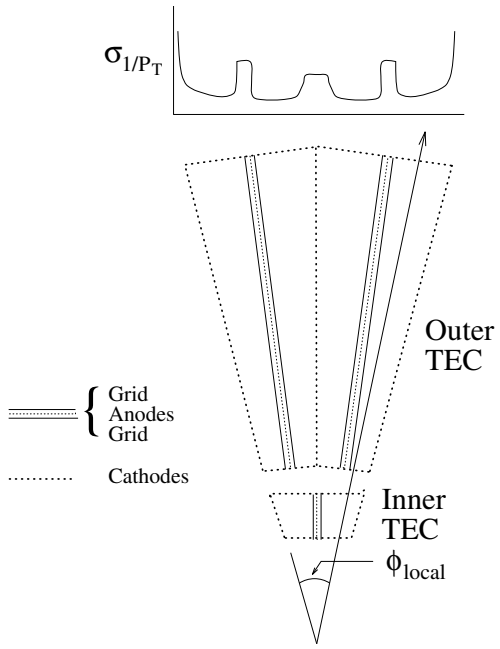

Figure 5.3: Definition of $\phi_{\rm local}$. A qualitative resolution function is shown above the picture of the TEC sector, roughly indicating the relation between resolution and the TEC sector geometry.

at about 270 mm for the barrel. Since the sagitta is normally distributed, so is $1/P_T$, and therefore we shall evaluate the TEC resolution in terms of this quantity. Also note that σ_{1/P_T} depends on some constants multiplied by σ_S, which in turn depends on the TEC single wire resolution. Thus σ_{1/P_T} is independent of P_T.

The TEC resolution depends rather strongly on the azimuthal angle, ϕ; tracks which pass far from the anodes suffer more from diffusion and are therefore measured with poorer spatial resolution than those which pass closer. The resolution in the amplification region is severely degraded due to the high (and nonuniform) electric field and the difficulty involved in determining the drift time to drift distance relation in this region. Resolution also suffers close to the cathode wires on account of nonuniformity in the electric field. Figure 5.3 defines the angle $\phi_{\rm local}$ and shows qualitatively how the resolution σ_{1/P_T} depends on this quantity.

The TEC resolution also depends on the polar angle. Tracks with $|\cos\theta| > 0.75$

fail to form hits on the outermost TEC wires, degrading the resolution in this region. Since the number of missed wires increases with $\cos\theta$, so does the degradation of the resolution.

In addition to θ and ϕ, the TEC resolution depends on the number of hit wires and the span, and in principle should be determined as a function of all the parameters we have mentioned; in practice it is impossible, due to finite statistics, to isolate them all from one another. For purposes of charge determination and correcting for charge confusion, it is sufficient to parameterize the resolution in terms of quantities on which it depends most strongly, and particularly on quantities correlated with polarization, like the polar angle. Other factors on which the resolution depends must be averaged.

The TEC calibration procedure used for the 1991-1993 running periods is described in reference [36]. Tracks from a dimuon sample are used to determine global drift velocities and local corrections for each wire. A linear drift time to drift distance relationship is assumed for approximately the inner two thirds of each outer half-sector; nonlinear terms are added to the relationship for tracks with larger drift times. In the first step, tracks in the outer TEC are fitted from wire 9 to wire 54 using the known transverse momentum and approximate fill vertex location as constraints. On the first pass some ansatz constants are used in the drift time to drift distance relation; generally they come from another calibration. The residuals of inner TEC hits with the extrapolated track are then histogrammed for each of four classes corresponding to the different combinations of inner and outer TEC sectors through which a straight track can pass (see Figure 5.3). Tracks from the four classes are used to construct a χ^2 which reflects the quality of inner-outer TEC sector matching separately for each category, as well as the global quality of the inner-outer matching. The global drift velocity and a constant corresponding to the grid position are then varied to minimize the χ^2. Next, the average residuals are computed as a function of drift time for each wire and each half sector. A line is fitted to each distribution and a correction applied according to its slope. Since the residual distributions for neighboring anodes are not independent, this step is iterated until the corrections are stable.

In the following sections we describe techniques used to optimize and measure the TEC resolution. The main points are summarized below.

- A fiducial volume cut excluding the regions 4 cm away from the TEC end-flanges improves resolution by about 25% in the endcap region.
- Inclusion of the fill vertex in the track fit provides an additional 13 cm of

lever arm and significantly improves resolution in the endcap region, where tracks miss the outermost TEC anodes. In the track fit, the fill vertex is weighted by the LEP beamspot dimensions in quadrature with an isotropic term, $\sigma_{\rm I}$ which accounts for the finite decay length of the τ. The optimal value is found to be $\sigma_{\rm I} = 100\mu$m. There are no observed systematic effects in curvature from including the fill vertex in the fit.

- The TEC resolution is measured in the barrel region using dimuon events. In the drift region, the resolution on transverse momentum (P_T) is found to be $\sigma_{P_T}/P_T^2 \approx 0.015$ GeV^{-1}.
- The resolution in the endcaps, where there is no muon chamber coverage, is estimated using bhabhas by counting the fraction of events for which the TEC measures the same charge for each electron. As a crosscheck, the method is applied in the barrel and compared to the results from the dimuon study, and the results are found to agree. Resolution in the endcaps varies from $\sigma_{P_T}/P_T^2 \approx 0.03$ GeV^{-1} at $|\cos\theta| = 0.83$ to $\sigma_{P_T}/P_T^2 \approx 0.07$ GeV^{-1} at $|\cos\theta| = 0.92$

5.1.2 Resolution near the TEC endflange

In order to study tracks that miss the outer TEC anodes, a sample of dimuons was selected in the range $0.71 < |\cos\theta| < 0.81$. This region is depicted in Figure 5.4. The dimuon selection is described in section 5.1.4. If $|\cos\theta| > 0.82$, tracks can form hits only in the innermost layer of the muon chambers, and this range was not considered. TEC tracks within 35 mrad of an outer anode, 57 mrad of an inner anode, or 10 mrad of a cathode were rejected in order to avoid combining regions with widely differing resolutions (Figure 5.3). The curvature resolution was determined in six bins of $\cos\theta$ from the distribution of $1/P_T^{\rm TEC} - 1/P_T^{\rm MUCH}$. The quantity $P_T^{\rm TEC}$ is the transverse momentum measured by TEC, and $P_T^{\rm MUCH} \equiv qE_{\rm beam}\sin\theta$ where q is the sign of the momentum measured by the muon chambers and $E_{\rm beam}$ is the beam energy. The result, indicated by the filled circles in Figure 5.5, shows degradation of the resolution as $\cos\theta$ increases, as expected. However, note from the figure that $\sigma_{1/P_T} \approx 0.02$ GeV^{-1} at $|\cos\theta| \approx 0.72$, where there are no missed anodes. Since the resolution varies with lever arm according to $\sigma_{1/P_T} \propto 1/L^2$, we expect the resolution at $|\cos\theta| \approx 0.785$, where there are 9 missed anodes, to be about $\sigma \approx 0.028$ GeV^{-1}. This is about 40% lower than the observed value.

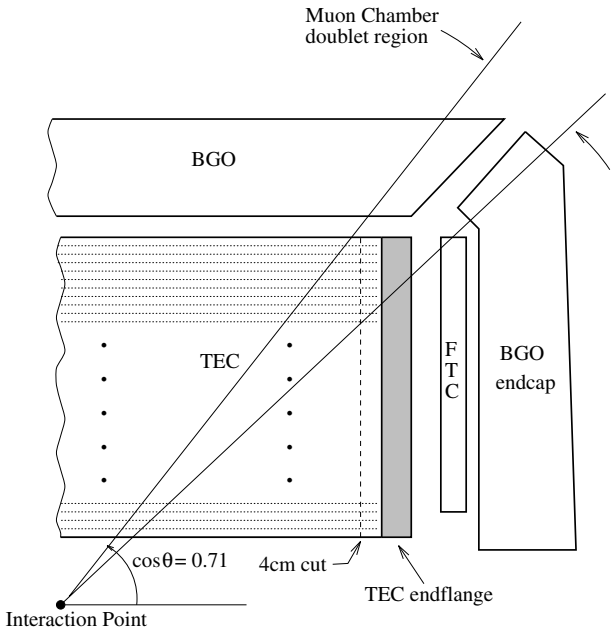

Figure 5.4: The region used to study the TEC resolution for tracks with $|\cos\theta| > 0.71$. Also shown are the TEC endflange and the location of the cut used to improve the resolution (see text). The dotted lines represent the anode wires; there are approximately twice as many anodes per unit length as shown in the figure.

Surprisingly, the removal of a few additional hits from the end of the track actually improves the resolution. For example, if all hits that fall within 4 cm of the endflange are removed from the fit which determines the curvature, then the resolution shown by the open circles in Figure 5.5 is achieved. This behavior is presumably a result of distortion of the electric field in the vicinity of the TEC endflange which alters the drift time to drift distance relation. Such an effect is not accounted for in the TEC calibration and so it adversely affects resolution. Now using the observed resolution at $|\cos\theta| \approx 0.72$ to predict the resolution at $|\cos\theta| \approx 0.78$ based on the number of missed wires plus additional hits removed by the 4 cm cut, we get $\sigma_{1/P_T} = 0.035$, in agreement with the observed value.

The cut on the region near the endflange was varied in order to determine what figure yields the best resolution, and 4 cm is found to be optimal. This corresponds

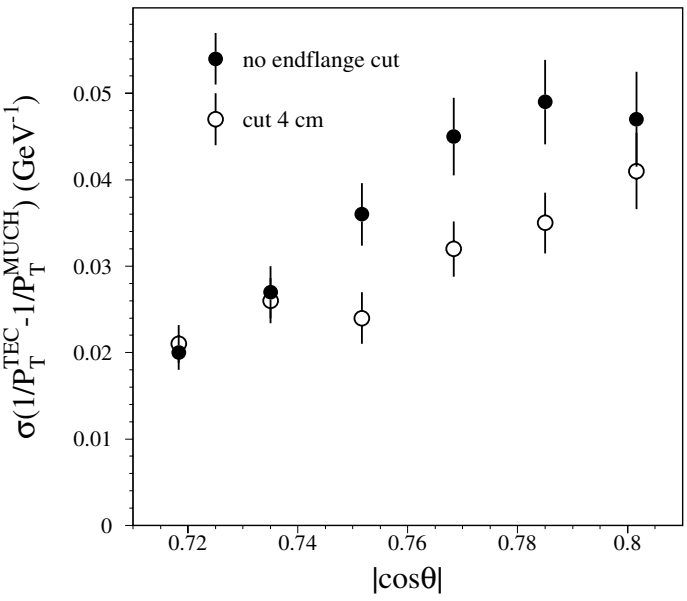

Figure 5.5: The TEC resolution in the region $0.71 < |\cos\theta| < 0.81$. The filled circles show the resolution when all hits on a track are used in the fit to determine the curvature. The open circles show the resolution if all hits within 4 cm of the endflange are removed from the fit.

to removal of approximately the last 6 hits for $\cos\theta = 0.8$ and the last 4 hits for $\cos\theta = 0.9$.

5.1.3 Inclusion of the fill vertex in the determination of P_T

As previously described, track parameters are extracted by fitting a circle to the space points determined from anode positions and drift times. Each point used in the fit is weighted by the spatial resolution for the corresponding anode and drift time. In addition to the points associated with the track, the position of the interaction vertex contains information about the track curvature. It is therefore desirable to include this point in the fit; its inclusion should improve the curvature resolution. The problem is then how to determine the location of the interaction vertex and how to weight this point in the fit.

Since the charged tracks observed in $Z \to \tau^+\tau^-$ events do not originate from a

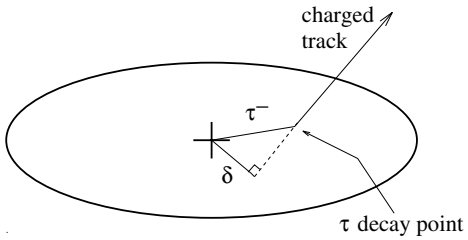

Figure 5.6: Definition of the impact parameter δ. The ellipse represents the beam spot.

common vertex, it is impossible to find the interaction point on an event-by-event basis. Instead, hadronic events from a single fill were grouped into a sample which was treated as if it were a single event; the common vertex extracted from this sample of several thousand tracks is known as the fill vertex. This approach is feasible since the LEP beam centroid is reasonably stable during a fill. The fill vertex was found from the hadron sample by minimizing the weighted sum of the track DCA's in the $r-\phi$ plane.

The probability for an e^+e^- interaction to occur at a given point plane depends on the profile of the LEP beam spot. The weight attached to the fill vertex in the fit must therefore reflect the beam spot dimensions.

The first step in finding the beam spot dimensions is determination of the intrinsic impact parameter resolution for the TEC. This was extracted from a sample of bhabha and dimuon events. Since the dileptons are produced at the same point and are nearly back-to-back, the distribution of the perpendicular distance between the tracks near the vertex, known as the miss distance, is a convolution of the impact parameter errors for the individual tracks, $\sigma_d^2 = \sigma_{\rm track1}^2 + \sigma_{\rm track2}^2$. Determination of the impact parameter resolution by this method has the advantages that it is independent of the beam centroid, and there is virtually no contribution to the resolution from multiple scattering since the lepton energies are high.

The next step is determination of the horizontal and vertical widths, $\sigma_{\rm H}$ and $\sigma_{\rm V}$, that characterize the gaussian shape of the beam spot in the $r-\phi$ plane. These were determined using the dimuon and bhabha samples by measuring the DCA resolution in bins of ϕ. This resolution function can be expressed in terms of σ_d

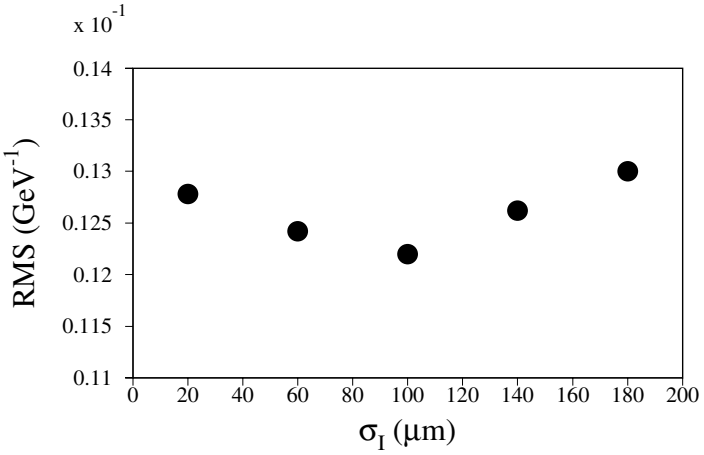

Figure 5.7: RMS for the distribution $1/P_T^{\rm smeared} - 1/P_T^{\rm generated}$ at several values of $\sigma_{\rm I}^2$. Each point corresponds to 100000 simulated tracks.

and the beam spot dimensions as follows,

$$\sigma^2_{\rm DCA}(\phi) = \sigma_d^2 + \sigma^2_{\rm H}\sin^2\phi + \sigma^2_{\rm V}\cos^2\phi \tag{5.2}$$

where the all the angles ϕ are folded onto the region $0 \leq \phi < \pi$. The dimensions $\sigma_{\rm H}$ and $\sigma_{\rm V}$ were found from a fit to equation 5.2. The beam spot dimensions for 1991-1993 are summarized in table 5.1. A detailed description of the methods outlined above is given in reference [35].

Running Period	$\sigma_{\rm H}$	$\sigma_{\rm V}$
1991	$157 \pm 3\mu$m	$23 \pm 10\mu$m
1992	$116 \pm 3\mu$m	$24 \pm 10\mu$m
1993	$157 \pm 3\mu$m	$35 \pm 10\mu$m

Table 5.1: Beam spot dimensions.

For tracks which originate at the e^+e^- vertex, an appropriate weighting for the fill vertex is $\sigma^2_{\rm B} = \sigma^2_{\rm H}\sin^2\phi + \sigma^2_{\rm V}\cos^2\phi$. In the case of $\tau^+\tau^-$ pairs, however, the tracks do not originate at the interaction vertex on account of the finite lifetime of

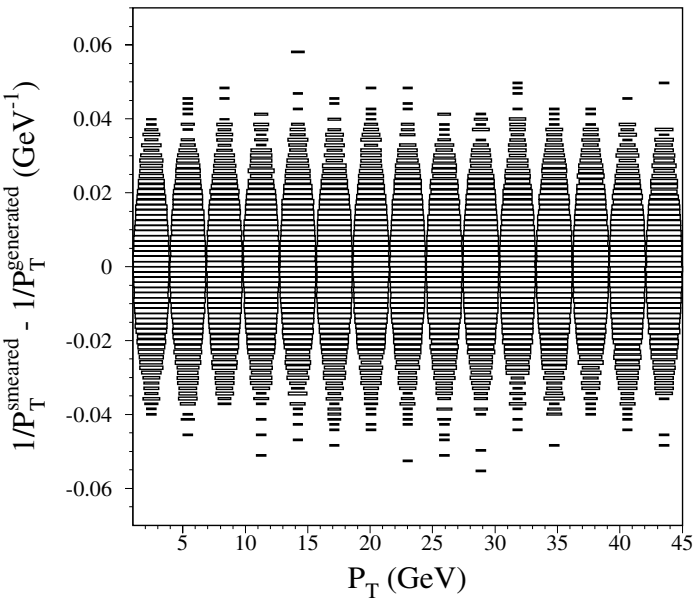

Figure 5.8: $1/P_T^{\text{smeared}} - 1/P_T^{\text{generated}}$ in bins of P_T. The area of each rectangle is proportional to the logarithm of the number of entries in the bin. The fill vertex weighting used $\sigma_{\text{I}} = 100\ \mu m$ in quadrature with the ϕ-dependent beam spot weight.

the τ, and the weighting must be adjusted to reflect this. Since the distribution of τ decay vertices is isotropic in ϕ, it is natural to append an isotropic term to the expression for σ_{B}:

$$\sigma_{\text{B}}^2 = \sigma_{\text{H}}^2 \sin^2\phi + \sigma_{\text{V}}^2 \cos^2\phi + \sigma_{\text{I}}^2 \tag{5.3}$$

The value of σ_{I} should reflect the size of the τ impact parameter (see Figure 5.6).

In order to determine the optimal value for σ_{I}, and to check for possible biases, the effects of including variously weighted fill vertices in the fit were simulated. The circle fitting algorithm was applied to simulated TEC tracks with an additional vertex hit, which was chosen at random from the distribution of the beam spot convoluted with the mean τ impact parameter. The impact parameter distribution was derived from Monte Carlo simulation which included all of the τ decay modes used in the polarization analysis.

Figure 5.7 shows the RMS for the distribution of $1/P_T^{\text{smeared}} - 1/P_T^{\text{generated}}$ for simulated tracks with a vertex point weighted according to equation 5.3. Evidently

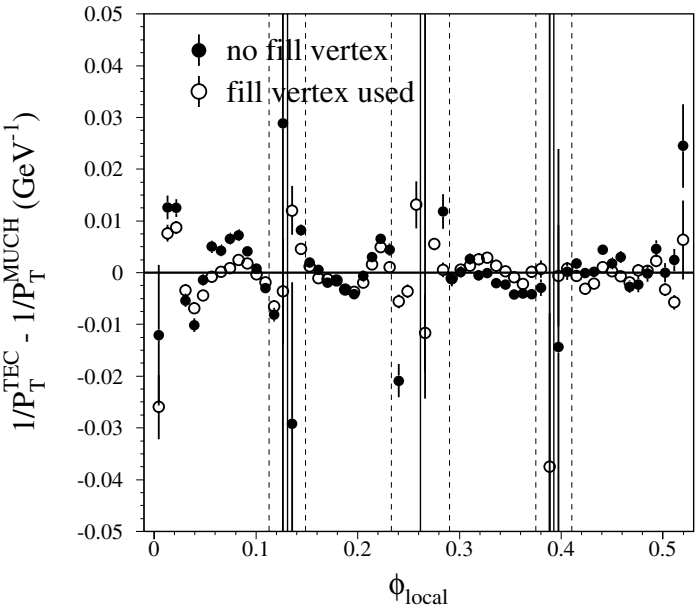

Figure 5.9: $1/P_T^{\rm TEC} - 1/P_T^{\rm MUCH}$ as a function $\phi_{\rm local}$ determined from a sample of dimuon data. Results are shown with and without inclusion of the fill vertex in the track fit. The solid vertical lines show the position of TEC anodes and the dashed lines indicate the approximate angle subtended by the amplification region. The data for this plot was taken from the 1992 sample.

an isotropic weight $\sigma_{\rm I} \approx 100\ \mu m$ is optimal for equation 5.3. This is not especially surprising since the mean impact parameter for τ's is 120 μm, quite close to the empirically determined optimal value for $\sigma_{\rm I}$.

In order to check for a possible energy bias introduced by the weighting scheme, the $1/P_T^{\rm smeared} - 1/P_T^{\rm generated}$ distribution was checked in various ranges of P_T. The simulation was used for this check, providing a very high statistics sample free from systematic effects that can result from TEC inefficiencies and calibration techniques and which can make it difficult to isolate real effects of the fill vertex. The results, shown in Figure 5.8 for the case $\sigma_{\rm I}$ =100 μm, exhibit no discernable bias in the curvature central value or asymmetry in the distribution of tails. This check was carried out with various values of $\sigma_{\rm I}$. While underweighting or overweighting the fill vertex adversely affects the resolution (Figure 5.7), there is no

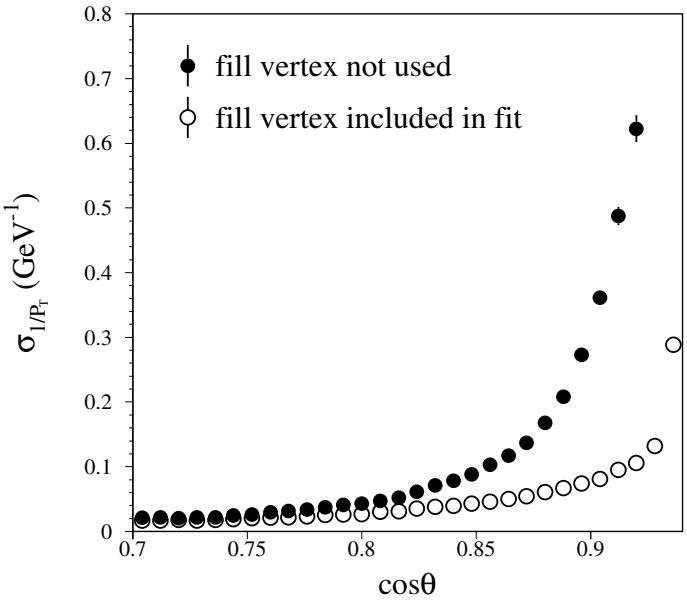

Figure 5.10: Resolution with and without inclusion of the fill vertex in the fit. The discontinuous step in resolution evident from the last point occurs at the angle for which no hits are formed in the outer TEC. The fill vertex is weighted with $\sigma_{\rm I} = 100\mu$m. The data use for this plot is from the 1992 running period.

statistically significant effect on the central value. The same checks were made separately for negatively and positively charged τ's and for tracks at various polar angles. The track fit is more sensitive to the fill vertex weight at forward angles, so any bias should be more pronounced there. These checks are summarized in Table 5.2.

The fill vertex weighting scheme was also checked with data by comparing the curvature measured by TEC with the known curvature for a sample of dimuons (see sections 5.1.2 and 5.1.4). The results, shown in Figure 5.9, indicate some systematic shifts in the measured curvature as a function of $\phi_{\rm local}$. These systematic shifts are present whether or not the fill vertex is used, and are predominantly a relic of the calibration. The 1992 sample exhibits the largest systematic effect for reasons described in the next section. Although there are local systematic shifts in curvature, the average shift is nearly 0, and as a result there is no net asymmetry

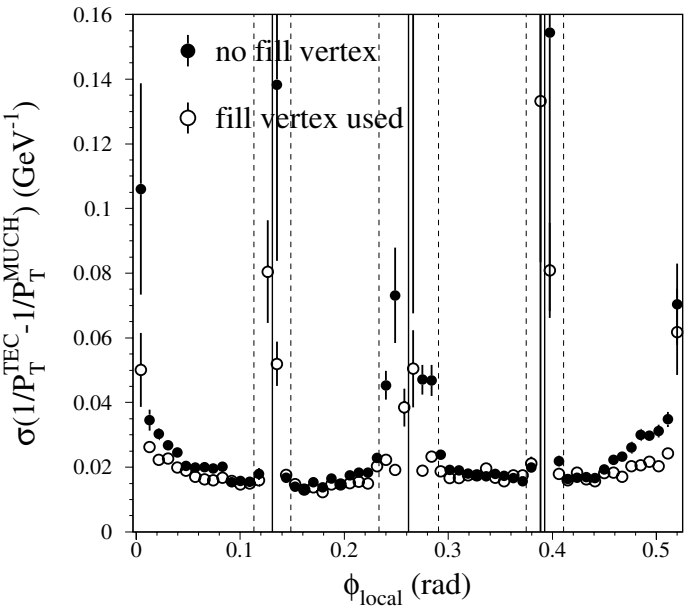

Figure 5.11: TEC resolution in the barrel as a function of $\phi_{\rm local}$. The solid dots show the resolution achieved without using the fill vertex; the open dots show the resolution with the fill vertex included in the track fit. The positions of the anodes are indicated by solid lines, and the the approximate angles subtended by the amplification regions are indicated by dashed lines. Inner cathodes are located at $\phi_{\rm local} = 0$ and 0.523.

σ_I (μm)	$N_{\rm last}$	$\left\langle \Delta^+_{1/P_T} \right\rangle \times 10^5$ (GeV^{-1})	$\left\langle \Delta^-_{1/P_T} \right\rangle \times 10^5$ (GeV^{-1})	RMS$^+$ (GeV^{-1})	RMS$^-$ (GeV^{-1})
0	62	-1.2 ± 5.5	3.1 ± 5.4	0.0127	0.0125
100	62	-1.9 ± 5.5	5.6 ± 5.5	0.0122	0.0121
200	62	3.1 ± 5.9	5.7 ± 5.8	0.0131	0.0130
100	34	-12 ± 11	-9 ± 15	0.0340	0.0340
100	21	-19 ± 29	2 ± 29	0.0650	0.0626
100	14	46 ± 41	-8 ± 42	0.0896	0.0833
100	10	13 ± 55	90 ± 55	0.1190	0.1186

Table 5.2: Checks of the fill vertex weighting scheme. σ_I is the isotropic part of the fill vertex weight, defined in equation 5.3. $\left\langle \Delta^+_{1/P_T} \right\rangle$ and $\left\langle \Delta^-_{1/P_T} \right\rangle$ are the mean values of $1/P_T^{\rm smeared} - 1/P_T^{\rm generated}$ for positively and negatively charged τ's, respectively. RMS$^+$ and RMS$^-$ are the corresponding RMS spreads for the distributions. $N_{\rm last}$ is the number of the last hit wire.

in the TEC charge measurement. Notice that inclusion of the fill vertex does not introduce an additional bias, but rather improves the situation somewhat.

The θ-dependence of the resolution with and without the fill vertex, as estimated by the simulation, is shown in Figure 5.10. There is some improvement in the barrel region, but far more dramatic is the improvement at forward angles. The fill vertex is some 13 cm away from the first TEC anode; this provides more than a twofold increase in lever arm at the most forward angles used in the polarization analysis. The open circles in Figure 5.10 roughly reflect the expected quadratic improvement with this extra lever arm.

Figure 5.11 shows the measured resolution in the barrel as a function of $\phi_{\rm local}$ with and without using the fill vertex in the track fit. Notice that there is little improvement in the regions of TEC which already exhibit good resolution, but that improvement in the vicinity of the cathodes and amplification regions is significant. Figure 5.12 shows the charge separation observed in the endcap for a sample of Bhabha events with and without using the fill vertex in the track fit. As expected from Figure 5.10, there is pronounced improvement for the case in which the fill vertex is used.

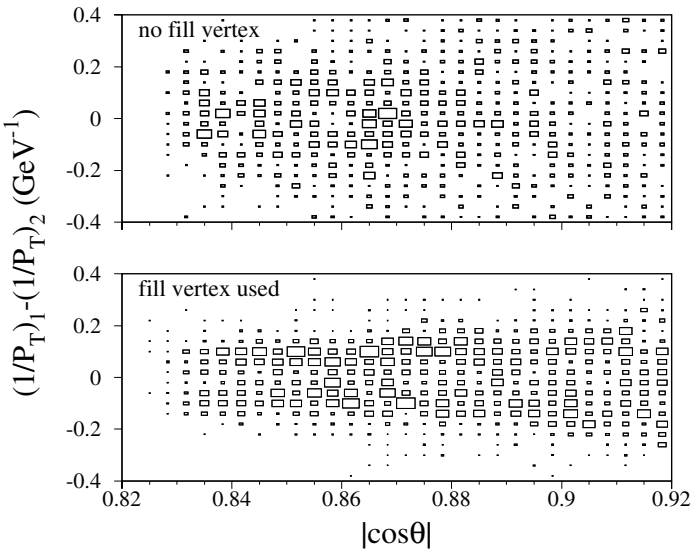

Figure 5.12: Difference in curvature between the pairs of tracks in bhabha events as measured by TEC with and without using fill vertex information. The angular range shown corresponds to the endcap region used in the polarization measurement. Since bhabhas in this angular range have P_T in the neighborhood of 20 GeV, a plot of curvature difference should in principle show two peaks at about $2 \times 1/20 \approx 0.1$ GeV^{-1}. Significantly improved charge separation is seen in the plot in which the fill vertex is included in the track fit.

5.1.4 TEC resolution in the barrel

The TEC resolution in the region $|\cos\theta| < 0.82$ was measured using a sample of dimuons. Dimuon events provide a source of charged tracks with known energy $E_\mu = E_{\rm beam}$ and charge determined unambiguously by the muon chambers. The charge confusion is negligible since the muon chamber resolution at 45 GeV is about 2.5% for triplets and 20% for doublets (see section 5.3). The TEC resolution can thus be determined by comparing the curvature measured by the TEC with the curvature computed from $E_{\rm beam}$, the polar angle, and the muon chamber charge measurement, as outlined in section 5.1.2. Since the curvature resolution is virtually independent of the curvature itself, the resolution determined at $E = 45$ GeV is valid over all energy ranges.

Dimuons were selected using the following criteria:

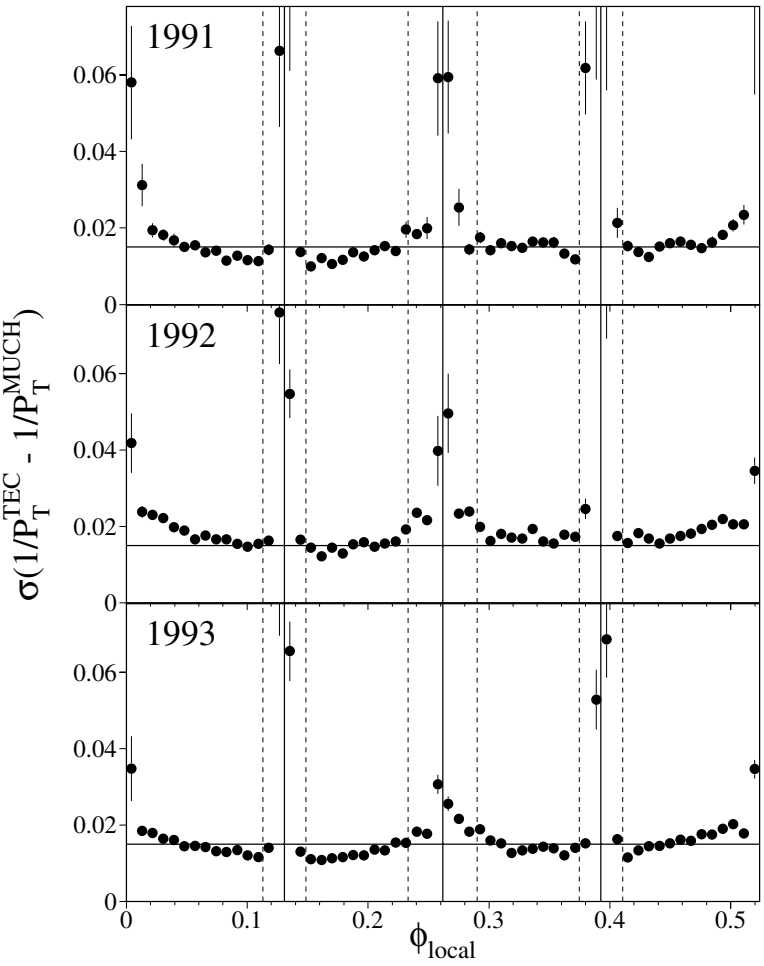

Figure 5.13: TEC resolution in the barrel as a function of $\phi_{\rm local}$ for 1991-1993. The line at $\sigma_{1/P_T} = 0.015$ is the average resolution expected from Monte Carlo simulation, and is included for comparison among the three figures. The solid vertical lines give the anode positions and the dashed line indicate the approximate angle subtended by the amplification region.

1. Each side contains a muon identified using the techniques described in section 4.2.4.

2. $P_\mu > 30$ GeV on each side.

As mentioned in section 5.1.1, the TEC resolution demonstrates a strong dependence on the azimuthal angle. Therefore σ_{1/P_T} was measured in bins of $\phi_{\rm local}$, where $\phi_{\rm local}$ spans one inner TEC sector (Figure 5.3). The results of the measurement are shown in Figure 5.13 for each of the 1991-1993 data taking periods. The resolution for 1991 and 1993 are comparable. The resolution for 1992 is somewhat worse. This is predominantly due to the fact that during the 1992 running period, the TEC gas pressure drifted away from its nominal value, an effect which was not discovered until the end of the run. A correction for the pressure drift was applied in the calibration scheme, improving the resolution. Some residual effect remains, however, due mostly to uncertainty in pressure drift as a function of time [36].

At angles above $|\cos\theta| > 0.75$, the resolution deteriorates due to the loss of hits on the outermost anodes (Figure 5.5). The onset of this effect can be seen in the barrel region (where there is still muon chamber coverage). Figure 5.14 shows the resolution as a function of $|\cos\theta|$, averaged over ϕ. The same sample was used as for the measurement of the resolution as a function of ϕ, except that the following additional fiducial volume cuts were employed:

- $\phi > 30$ mrad away from inner anode plane
- $\phi > 15$ mrad away from outer anode plane
- $\phi > 10$ mrad away from outer cathode plane

These cuts remove the regions with inferior resolution, ensuring that the distribution of $1/P_T^{\rm TEC} - 1/P_T^{\rm MUCH}$ can be reasonably characterized by a single σ.

5.1.5 TEC resolution in the endcaps

There is no muon chamber coverage[2] above $|\cos\theta| > 0.82$, so the TEC is the only subdetector that provides charge measurement in this region. Since there is no endcap data sample with superior charge and energy measurement with which the

[2]This is true prior to the 1994 running period. For the 1994 run, part of a forward-backward muon system was installed.

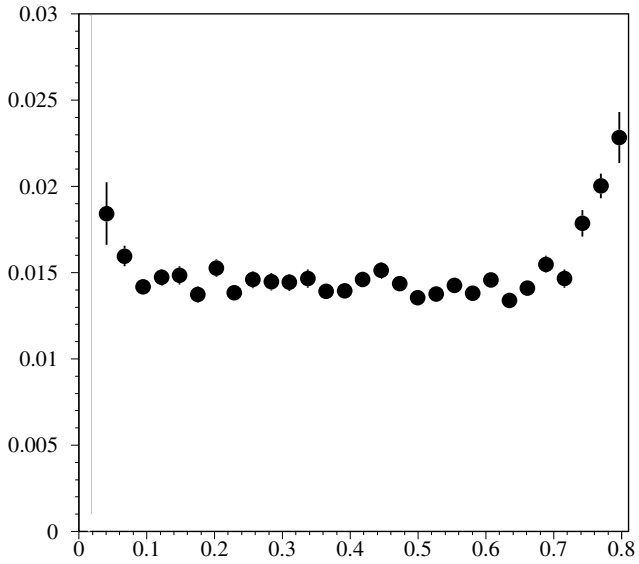

Figure 5.14: TEC resolution as a function of $|\cos\theta|$ in the barrel region for the 1993 data sample.

TEC measurement can be compared, the resolution cannot be determined using the methods described in section 5.1.4. An alternative approach was therefore followed in which the resolution is inferred from the observed charge confusion in bhabha events, exploiting the fact that for normally distributed curvature, charge confusion and curvature resolution are related by the error function.

Ideally, the first step in the method should involve mapping the charge confusion as a function of all the parameters, $\vec{\alpha}$, on which it depends. $\vec{\alpha}$ should include, for example, ϕ, P_T, $\cos\theta$, number of hits, and span. Unfortunately statistics limits the intricacy with which these parameters can be isolated from one another. Since the two back-to-back electrons in a bhabha event see regions of TEC with similar resolutions, and since their energies are the same (neglecting radiation), the charge confusion probability is approximately the same for the two tracks produced. Thus the charge confusion, ϵ, is given in each bin of $\vec{\alpha}$ by

$$N'(\vec{\alpha}) = 2N(\vec{\alpha})\epsilon(\vec{\alpha})(1-\epsilon(\vec{\alpha})) \tag{5.4}$$

where $N'(\vec{\alpha})$ is the number of events with track parameters $\vec{\alpha}$ for which the charges

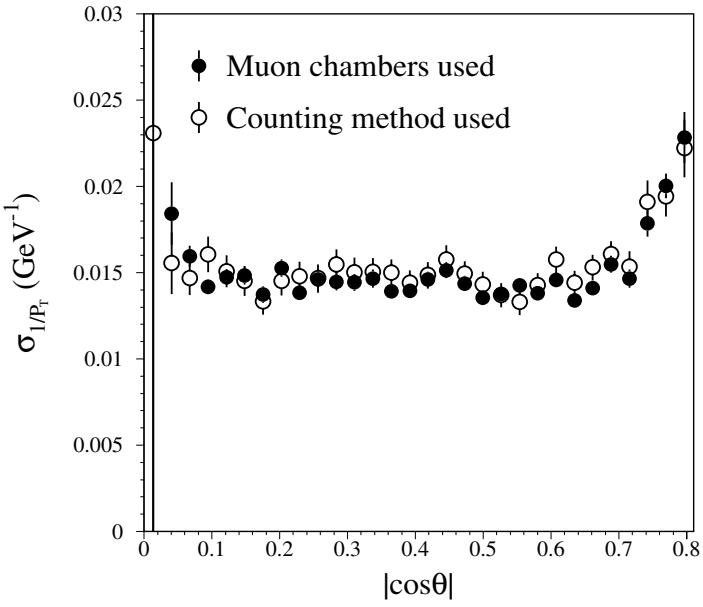

Figure 5.15: Comparison of barrel resolution vs. $\cos\theta$ derived using the muon chamber measurements compared to resolution inferred from the measured charge confusion ("counting method"), which uses charge information from the TEC alone. This figure corresponds to the 1993 data sample.

on the two sides are measured by TEC to be the same, and $N(\vec{\alpha})$ is the total number of events. The resolution in each $\vec{\alpha}$ bin can then be estimated from the measured charge confusion and the absolute value of the track curvature, which for bhabhas is known from BGO information. If one assumes the curvature measured by the TEC is normally distributed around the true curvature in some reasonably narrow range of $\vec{\alpha}$, then the charge confusion is

$$\begin{aligned} \epsilon(\vec{\alpha}) &= \int_{-\infty}^{0} \frac{1}{\sqrt{2\pi}\sigma'(\vec{\alpha})} e^{-(\mathcal{C}-|\mathcal{C}_0|)^2/2\sigma'^2(\vec{\alpha})} d\mathcal{C} \\ &= 2\left[1 - \mathrm{erf}\left(|\mathcal{C}_0|\,/\sqrt{2}\sigma'(\vec{\alpha})\right)\right] \end{aligned} \tag{5.5}$$

where $\mathcal{C}_0$ is the curvature, and $\sigma'(\vec{\alpha})$ is the estimate of the resolution.

The sample of Bhabha events used to estimate endcap resolution was selected according to the following criteria:

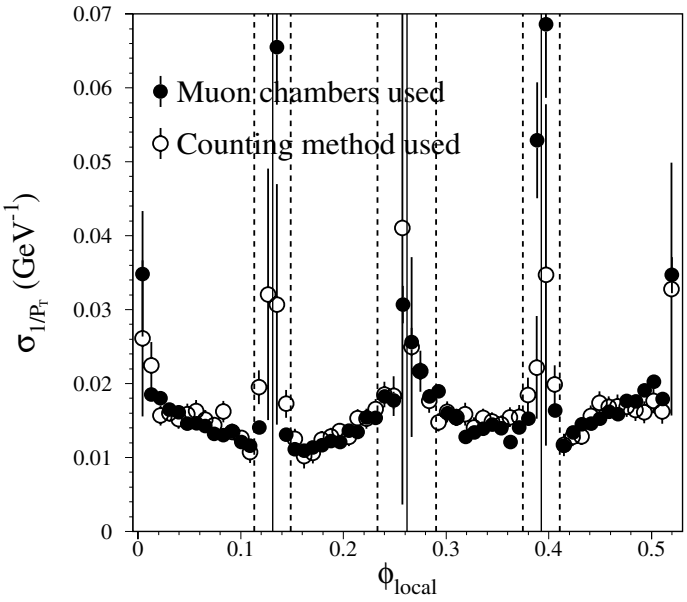

Figure 5.16: Comparison of barrel resolution vs. $\phi_{\rm local}$ as determined using muon chamber information and using the counting method. The figure corresponds to the 1993 data sample.

1. Electron identified in each hemisphere using the techniques described in section 4.2.2.

2. Electron energies both between 40 GeV $< E_e <$ 50 GeV

3. Acoplanarity $<$ 2 mrad

4. Hits on at least 65% of the TEC anodes on which it is possible to form hits

The electromagnetic χ^2 is described in chapter 4. The acoplanarity cut reduces contamination from radiative bhabhas.

The validity of the resolution estimation hinges largely on the validity of equation 5.5, and specifically on the underlying assumption that the measured curvature is normally distributed around the true curvature. To check this assumption for a realistic average over parameters from $\vec{\alpha}$, the methods outlined above (referred

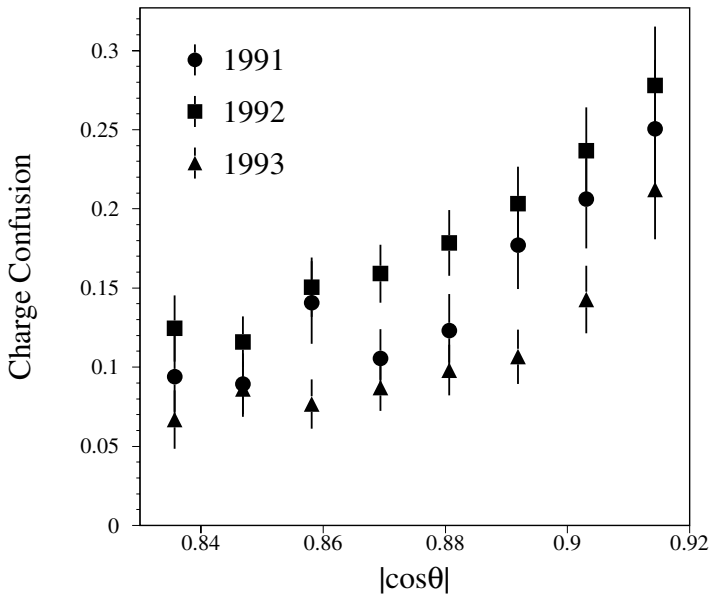

Figure 5.17: Charge confusion in the endcap region as a function of $\cos\theta$ for the 1991-1993 data samples.

to hereafter as the "counting" method) were applied to a data sample in the barrel and then compared with the results derived from the barrel dimuon sample. Figure 5.15 shows a comparison of the results obtained for σ_{1/P_T} vs. $|\cos\theta|$ using the the methods described here and in section 5.1.4. For this comparison, the fiducial volume cuts that remove the regions near the anodes and cathodes were applied, but otherwise an average was taken over all other angles ϕ and track quality parameters. A similar comparison was made in bins of $\phi_{\rm local}$ to check that the structure derived from the dimuon sample is also evident if the counting method is used. The results are shown in Figure 5.16. Note that the agreement is reasonable throughout the drift region, but is poorer in the grid regions where the data sample is small due to reduced efficiency, and where the charge confusion is large. For the measurement shown in Figure 5.16, the sample was further subdivided into bins of P_T and the weighted average was taken. This is necessary since the charge confusion depends on P_T, which varies from about 32 to 45 GeV for bhabhas in the barrel region.

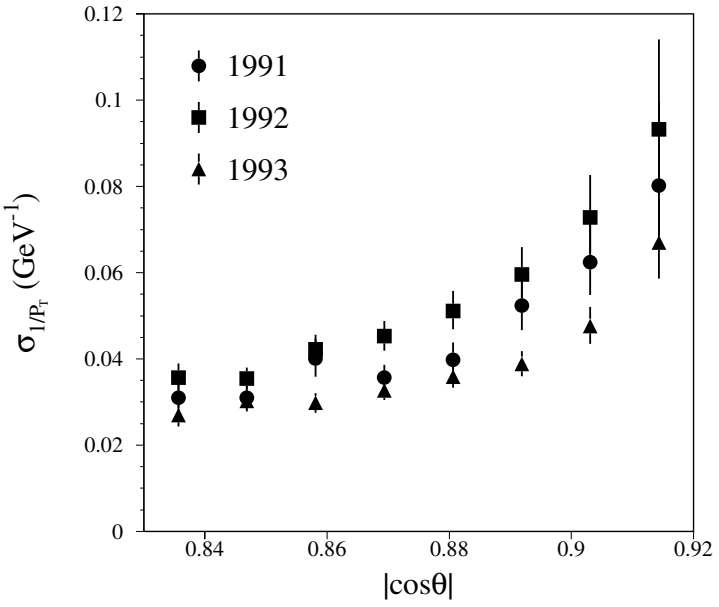

Figure 5.18: Endcap resolution as a function of $\cos\theta$. The error bars reflect the statistical uncertainty on the charge confusion measurement.

Since the resolution in the endcaps depends strongly on $\cos\theta$ and since the τ polarization itself is also $\cos\theta$-dependent, it is most important that θ be included in the parameters $\vec{\alpha}$. The endcap charge confusion measured in bins of $\cos\theta$ using equation 5.4 is shown in Figure 5.17. As explained in section 5.1.4, the 1993 data sample exhibits the best resolution and thus the lowest charge confusion. Charge confusion is most severe for the 1992 sample. The resolution estimated from the measured charge confusion using equation 5.5 is shown in Figure 5.18. Again, the fiducial volume cuts that remove the cathode and grid regions were employed. The binning was chosen so that each $\cos\theta$ bin spans about the same range of number of hit wires as is spanned for a bin in Figure 5.15. In the case of Figure 5.18, the range of hit wires is a geometrical effect, whereas for Figure 5.15 it is a result of hit efficiency. Hit efficiency refers to the fraction of anodes along a track that register hits.

Due to limited statistics, it is not possible to separate the θ and ϕ structures of the endcap resolution with much precision. Therefore it was assumed that

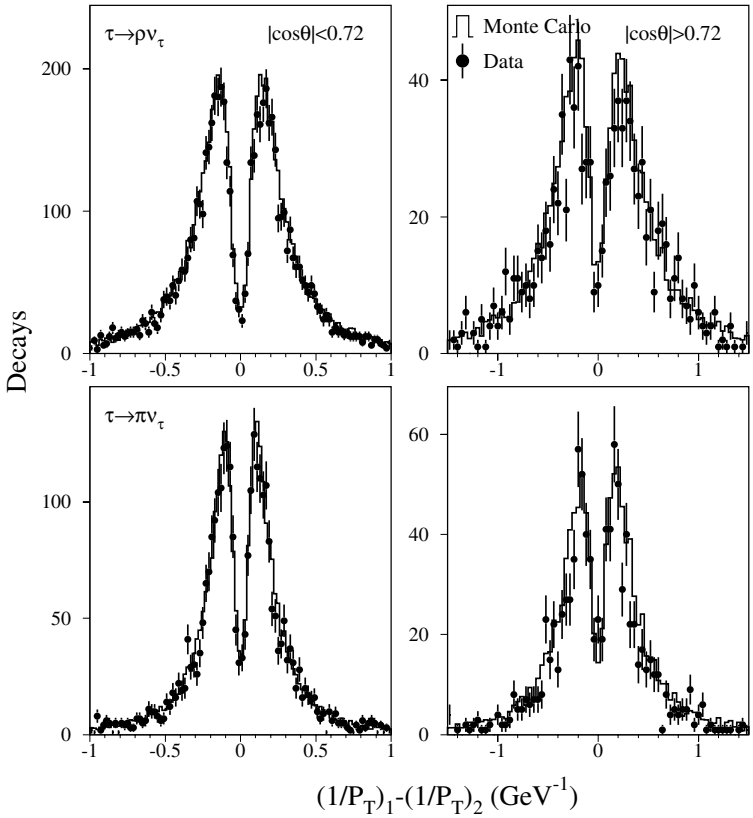

Figure 5.19: Charge separation in the barrel and endcap regions for selected $\tau^- \to \rho^-\nu_\tau$ and $\tau^- \to \pi^-\nu_\tau$ events. The upper two plots show the curvature difference for charged pions in the barrel and endcap regions for events in which at least one hemisphere is selected as a $\tau^- \to \rho^-\nu_\tau$ decay. The lower two plots are for selected $\tau^- \to \pi^-\nu_\tau$ decays.

the details of the ϕ-dependence measured in the barrel apply equally well to the endcap and can be scaled by the measured average θ-dependent resolution. The full detector Monte Carlo was resmeared according to the resulting resolution function. Figure 5.19 shows a comparison of the charge separation produced in the Monte Carlo as a result of this resmearing with the charge separation in observed in data for selected $\tau^- \to \rho^-\nu_\tau$ and $\tau^- \to \pi^-\nu_\tau$ decays. The charge separation is somewhat better for $\tau^- \to \rho^-\nu_\tau$ decays because the energy spectrum for the charged pion is less energetic than in the case of $\tau^- \to \pi^-\nu_\tau$. It is useful to perform a check for these decay modes since thus far they are the two channels used for polarization analysis in the endcaps. The $\tau^- \to \rho^-\nu_\tau$ and $\tau^- \to \pi^-\nu_\tau$ selections are described in Chapter 4.

5.2 TEC momentum scale

The TEC momentum scale was verified at 45 GeV using $Z \to \mu^+\mu^-$ decays. The distribution of $\Delta_{1/P_T} = 1/P_T^{\rm TEC} - 1/P_T^{\rm MUCH}$ shown in Figure 5.9 can be used to estimate the accuracy of the momentum scale if one notes that $E_{\rm beam}/P^{\rm TEC} = 1 + \Delta_{1/P_T} E_{\rm beam} \sin\theta$. A weighted average of Δ_{1/P_T} for all the open circles in Figure 5.9 gives $\mu = (1.8 \pm 1.2) \times 10^{-4}$ GeV^{-1}. Assuming then a curvature shift $\Delta_{1/P_T} = 2.0 \times 10^{-4}$ GeV^{-1} and taking $\langle \sin\theta \rangle = 0.91$ yields a shift in the average TEC momentum scale of roughly 1.3%. This is an important check, because a substantial shift in the TEC momentum scale can be problematic for both the charged pion energy measurement and the charge determination.

The effect on charge determination can be understood in the following way. Let the true track curvature be denoted $\mathcal{C}^{\rm true}$ and the curvature measured by the TEC $\mathcal{C}^{\rm TEC}$. Suppose a positive momentum scale shift is observed, such that $\left\langle \Delta_{1/P_T} \right\rangle > 0$. For this to occur, it must be the case that for positively charged tracks $\left\langle \mathcal{C}^{\rm TEC} \right\rangle > \langle \mathcal{C}^{\rm true} \rangle$. On the other hand negatively charged tracks must have $\left\langle \left| \mathcal{C}^{\rm TEC} \right| \right\rangle < \langle |\mathcal{C}^{\rm true}| \rangle$ in order to contribute to the $\left\langle \Delta_{1/P_T} \right\rangle$ shift in the same sense as positively charged tracks. So for positively charged tracks, the charge confusion is less than it would be for the case $\left\langle \Delta_{1/P_T} \right\rangle = 0$, because $\left\langle \mathcal{C}^{\rm TEC} \right\rangle$ is shifted in the positive direction. For negatively charged tracks, the charge confusion is greater than for the case $\left\langle \Delta_{1/P_T} \right\rangle = 0$, again because $\left\langle \mathcal{C}^{\rm TEC} \right\rangle$ is shifted in the positive direction. As a result, for $\left\langle \Delta_{1/P_T} \right\rangle > 0$ a greater number of negatively charged tracks is observed in TEC than positively charged tracks. Such a phenomenon is

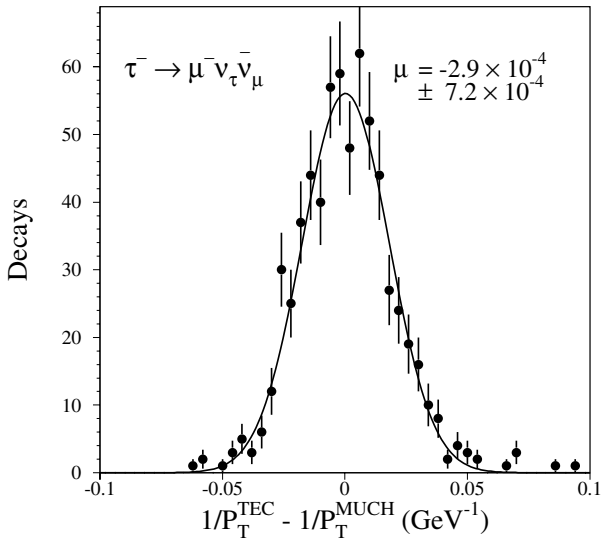

Figure 5.20: $1/P_T^{\rm TEC} - 1/P_T^{\rm MUCH}$ for selected $\tau^- \to \mu^- \bar{\nu}_\mu \nu_\tau$ decays, where $1/P_T^{\rm MUCH}$ is the inverse transverse momentum measured by the muon chambers. Muons with $E_\mu < 20$ GeV were used. The acceleration and cathode regions of TEC were excluded. The mean value from a gaussian fit to the distribution is given in the figure.

particularly hazardous to the $\mathcal{P}_\tau(\cos\theta)$ measurement, since the track charge is used attach a sign to $\cos\theta$. Fortunately a significant shift in $\left\langle \Delta_{1/P_T} \right\rangle$ is not observed in the data. We can estimate the consequences of a 1% momentum scale shift on the charge confusion asymmetry using equation 5.5. In the case of $P_T = 45$ GeV and $\sigma_{1/P_T} = 0.018$ GeV^{-1}, for example, the asymmetry in charge confusion is about 4% of the charge confusion itself.

At low energies, the TEC momentum scale was checked using muons and electrons from $\tau^- \to \mu^- \bar{\nu}_\mu \nu_\tau$ and $\tau^- \to {\rm e}^- \bar{\nu}_{\rm e} \nu_\tau$ decays. A comparison of the muon curvature measured by the TEC and by the muon chambers for $\tau^- \to \mu^- \bar{\nu}_\mu \nu_\tau$ decays is shown in Figure 5.20. The average muon energy for decays used in the figure is approximately 10 GeV. The energy shift corresponding to the uncertainty on the central value of $1/P_T^{\rm TEC} - 1/P_T^{\rm MUCH}$ shown in the figure is about

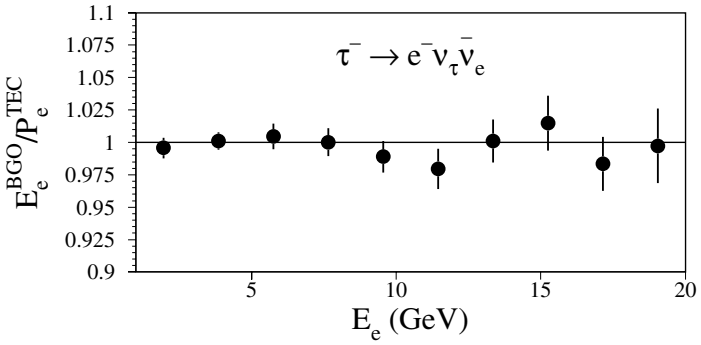

Figure 5.21: E_e^{BGO}/P_e^{TEC} as a function of electron energy for $\tau^- \to e^- \bar{\nu}_e \nu_\tau$ decays.

0.8%. A comparison of the electron energies measured by the BGO and the corresponding momenta measured by the TEC is shown in Figure 5.21. The average $E_e^{BGO}/P_e^{TEC} = 0.998 \pm 0.004$

5.3 Resolution and energy scale for the muon spectrometer

The muon chamber resolution at high energies was determined using $Z \to \mu^+\mu^-$ events. Due to chamber inefficiencies and limited acceptance, not all tracks form hits in all three layers of the detector. For muons that produce hits in all three layers ("triplets"), the momentum is determined from the track sagitta. For the cases in which only two hits are formed ("doublets"), the momentum is computed from the difference of slopes in the two layers. The resolution for doublets is considerably worse than for triplets, as shown in Figure 5.22. The resolution is extrapolated to low energies using Monte Carlo to simulate the effects of multiple scattering in the calorimeters. This energy dependence is shown in Figure 5.25.

The accuracy of the muon momentum scale is estimated to be 0.2% at 45 GeV from a study of $Z \to \mu^+\mu^-$ decays, for which the muon energy is known from the beam energy. The momentum scale at low energies is dominated by energy loss in the calorimeters; a severe shift in this scale can be detected by comparison of the TEC and muon chamber momentum measurements for $\tau^- \to \mu^- \bar{\nu}_\mu \nu_\tau$ decays, which is shown in Figure 5.20.

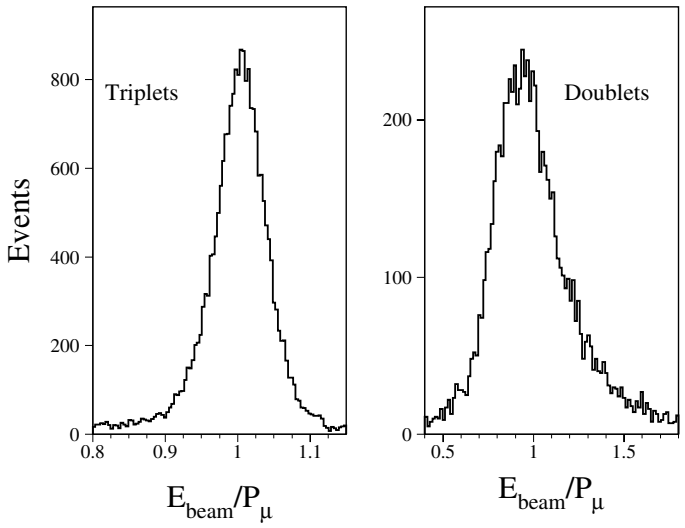

Figure 5.22: Muon chamber resolution for doublet and triplet tracks at $P_\mu \approx 45$GeV from a sample of $Z \to \mu^+\mu^-$ events. The resolution is about 2.5% for triplets and 20% for doublets. Note the scale difference on the two plots.

5.4 Resolution and energy scale for the BGO

The BGO is used to determine the electron energy for the $\tau^- \to e^-\bar{\nu}_e\nu_\tau$ channel and the π^0 energy for the $\tau^- \to \rho^-\nu_\tau$ and $\tau^- \to a_1^-\nu_\tau$ channels. Furthermore, BGO energy depositions from charged hadrons are combined with the hadron calorimeter measurement to determine charged hadron energies in the $\tau^- \to \rho^-\nu_\tau$, $\tau^- \to \pi^-\nu_\tau$, and $\tau^- \to a_1^-\nu_\tau$ channels. Thus the BGO resolution and energy scale for electrons and photons, and the combined calorimeter energy scale for charged hadrons are important.

The BGO energy scale for electrons and photons was checked at 45 GeV using a sample of $Z \to e^+e^-$ events, and the accuracy is estimated to be 0.1%. At low energies, the position of the π^0 peak was used to check the absolute scale, and it is estimated to be accurate to 1% at 1 GeV. Figure 5.23 shows the invariant mass for the photons produced in $\tau^- \to \rho^-\nu_\tau$ decays. The $\tau^- \to \rho^-\nu_\tau$ selection is described in Chapter 4. The BGO resolution as a function of energy for electrons and photons is plotted in Figure 5.25.

The absolute energy scales of the BGO and hadron calorimeter for hadrons are known to about 1.5% from the position of the ρ invariant mass peak, shown in

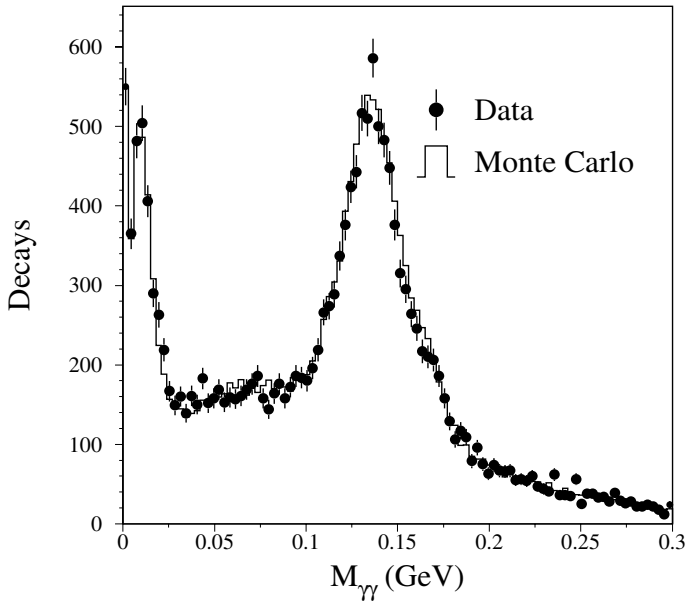

Figure 5.23: The invariant mass of $\gamma\gamma$ pairs in selected $\tau^- \to \rho^-\nu_\tau$ candidates together with the Monte Carlo prediction.

Figure 4.16.

5.5 Charged pion measurement

The calorimeters offer better energy resolution than the TEC for charged pions above about 10 GeV. On the other hand, the TEC momentum resolution is superior below 10 GeV. For this reason, the measurement of charged pion energies employs a combination of measurements from the central tracking and the calorimeters.

A calorimetric calibration has been developed using a test beam sample of over 10^6 charged pions. It is necessary to resort to test beam data since there is no sample of isolated charged pions of known energy available from Z decays. An approximate calorimetric energy resolution is found to be $\sigma_{E_{\pi^\pm}} \approx 55\%/\sqrt{E_{\pi^\pm}} + 8\%$. The calibration procedure is described in detail in reference [32].

The procedure for combining the calorimetric energy measurement with the momentum measurement from TEC consists of maximizing the probability, P_{combined},

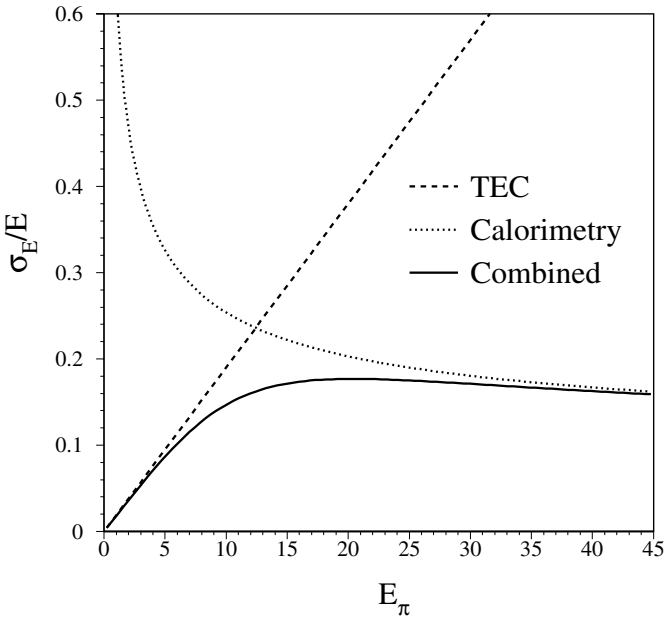

Figure 5.24: The resolution attained for charged pion energy measurement by combining measurements from the TEC and the calorimetry.

that the two measurements arise from the same underlying energy, ϵ:

$$\begin{aligned} P_{\text{combined}} &= P(E_C;\epsilon,\sigma_C(\epsilon))P(1/P_T;\epsilon,\sigma_{1/P_T}) \qquad (5.6)\\ &= \frac{1}{\sqrt{2\pi}\sigma_C^2(\epsilon)}\exp\left(-\frac{(E_C-\epsilon)^2}{2\sigma_C^2(\epsilon)}\right)\frac{1}{\sqrt{2\pi}\sigma_{1/P_T}^2}\exp\left(-\frac{(1/P_T-1/\epsilon\sin\theta)^2}{2\sigma_{1/P_T}^2}\right) \end{aligned}$$

where E_C is the measured energy in the calorimeters, $1/P_T$ is the inverse transverse momentum measured by the TEC, and $\sigma_C(\epsilon)$ and σ_{1/P_T} are the errors on these quantities. Both $\sigma_C(\epsilon)$ and σ_{1/P_T} depend on the polar and azimuthal angles. The dependence of σ_{1/P_T} on θ and ϕ has been described in detail above. The form $\sigma_C(\epsilon)$ was derived from the test beam study. Equation 5.6 can also be used to check the compatability between a TEC track and energy deposition in the calorimeters.

Figure 5.24 illustrates the effect of combining the TEC and the calorimeters to measure charged pion energies.

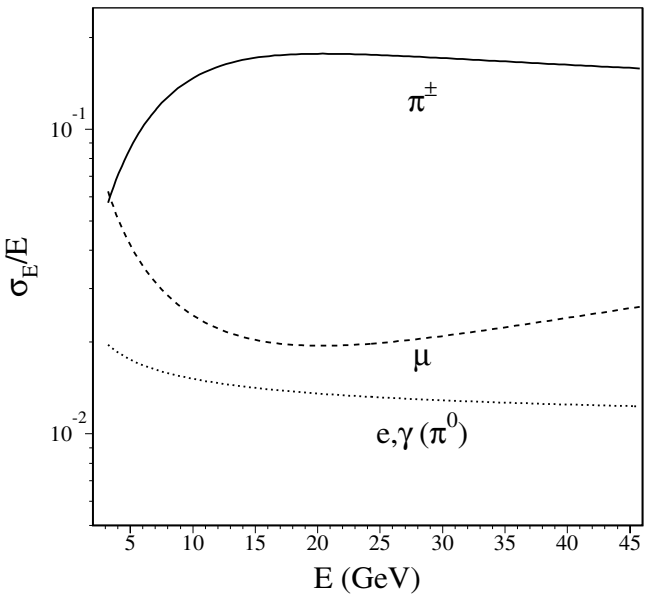

Figure 5.25: Resolutions as a function of energy for electrons, photons, muons, and charged pions.

5.6 Summary of detector resolution

Figure 5.25 gives a summary of the resolutions attained for electrons, photons, muons, and charged pions.

Chapter 6

Measurement of τ Polarization

In this chapter we present the results of the τ polarization measurement. The goal is determination of $\mathcal{A}_\tau$ and $\mathcal{A}_e$, the quantities directly related to the weak neutral couplings as discussed in Chapter 1. Extraction of these quantities from the data proceeds in two phases.

First, the polarization $\mathcal{P}_\tau$ is determined separately for each channel in each of nine $\cos\theta$ bins. The $\cos\theta$ bins are chosen such that they all contain approximately the same number of decays. Table 6.1 gives the angular range and acceptance fraction for each bin. The general principles of the fitting method used to determine $\mathcal{P}_\tau$ in each bin are described in sections 6.1.1 and 6.1.2. The polar angle θ is assigned by the thrust axis and event charge, as discussed in section 6.1.3. A fitting technique which corrects for the effects of charge confusion is outlined in section 6.1.4. In section 6.2 we describe the fitting in each channel, including details concerning background estimation and a summary of systematic errors.

Next, the individual channel results are corrected for radiative effects (section 6.3.1) and combined bin-by-bin in $\cos\theta$. At this point we account for the statistical correlation when both τ's in an event are selected for the polarization measurement; the method is described in section 6.3.2. Finally, the fit for $\mathcal{A}_\tau$ and $\mathcal{A}_e$ and the propagation of errors into the final result is described in section 6.3.3.

	$\cos\theta$ low	$\cos\theta$ high	Acceptance fraction
Endcap	-0.92	-0.72	0.109
Barrel	-0.72	-0.55	0.092
	-0.55	-0.35	0.109
	-0.35	-0.12	0.125
	-0.12	0.12	0.130
	0.12	0.35	0.125
	0.35	0.55	0.109
	0.55	0.72	0.092
Endcap	0.72	0.92	0.109

Table 6.1: Sizes of the $\cos\theta$ regions used to determine $\mathcal{P}_\tau(\cos\theta)$.

6.1 Fitting method

6.1.1 General principles

The τ polarization may be determined by fitting the observed decay spectra to the analytic distributions described in Chapter 2. This requires that the analytic distributions be corrected for detector effects like acceptance and resolution. Estimation of these effects invariably relies to some extent on the Monte Carlo simulation of the detector response. Alternatively, we can directly compare the τ decay distributions generated by the Monte Carlo simulation to the observed data distributions. In this approach the polarization is determined by finding the linear combination of $h = +1$, $h = -1$, and background Monte Carlo distributions which best fits the data.

The second approach, often called "reweighting," is used in this analysis. It is useful to outline the method first for the simple case of a one-dimensional binned maximum likelihood fit with infinite Monte Carlo statistics. The polarization sensitive distribution is then written in terms of the $h = +1$, $h = -1$, and background contributions as follows,

$$N_i = r_+ m_{i+} + r_- m_{i-} + r_B m_{iB} \tag{6.1}$$

where m_{i-} and m_{i+} are the number of $h = -1$ and $h = +1$ Monte Carlo entries

in the i'th bin and m_{iB} is the number of background entries. r_+, r_-, and r_B determine the relative contributions from these distributions; these are what we want to know. The role of the polarization is more evident if we write r_+ and r_- in terms $\mathcal{P}_\tau$ and the overall normalization between data and Monte Carlo,

$$\begin{aligned} r_+ &= r\frac{1+\mathcal{P}_\tau}{1+\mathcal{P}_\tau^{\rm MC}} \\ r_- &= r\frac{1-\mathcal{P}_\tau}{1-\mathcal{P}_\tau^{\rm MC}} \end{aligned} \tag{6.2}$$

where $\mathcal{P}_\tau^{\rm MC}$ is the polarization in the Monte Carlo. Since background from other τ decay channels depends on the polarization, it is included in m_+ and m_-, and is thus varied simultaneously with the signal during the fit. Background from non-τ sources does not depend on polarization, so it is varied separately[1].

Since we have assumed an infinite Monte Carlo sample, we can construct a likelihood function assuming Poisson statistics in each data bin and no fluctuations in the Monte Carlo,

$$\mathcal{L} = \prod_i \frac{e^{-\nu_i}{\nu_i}^{n_i}}{n_i!} \tag{6.3}$$

where n_i is the number of events observed in the i'th data bin, and ν_i is the expected numbers of events in that bin, as computed using equation 6.1. The fitting procedure then consists of varying $\mathcal{P}_\tau$, r, and r_B in equations 6.1 and 6.2 until the maximum of $\mathcal{L}$ is found[2]. This can be done using the MINUIT minimization package [41].

6.1.2 Fitting with limited Monte Carlo statistics

The Monte Carlo sample for this analysis is in fact about eight times larger than the data sample, so fluctuations in the m_+, m_-, and background distributions are not negligible and must be taken into account. Here we describe two approaches to constructing a suitable likelihood function.

Assuming Poisson statistics, the probability to observe n_i data events in the

[1] In practice the handling of the non-τ background distribution(s) depends on the channel being analyzed. This is discussed in subsequent sections.

[2] In practice the negative log-likelihood function, $-\ln\mathcal{L}$, is minimized.

i'th bin given the expected number of events ν_i is,

$$P_i^{\text{data}} = \frac{e^{-\nu_i}{\nu_i}^{n_i}}{n_i!} \tag{6.4}$$

The expected number of data events in a bin is related to the expected number of Monte Carlo events in that bin by,

$$\nu_i = \sum_{j=1}^{M} \mu_{ij} r_j \tag{6.5}$$

where the index j runs over the M different Monte Carlo and background sources and r_j determines the relative contribution from source j. Now we account for fluctuations in the Monte Carlo. The probability to observe m_{ij} events in bin i from Monte Carlo source j is,

$$P_i^{\text{MC}} = \frac{e^{-\mu_{ij}}(\mu_{ij})^{m_{ij}}}{m_{ij}!} \tag{6.6}$$

where again μ_{ij} is the expected number of Monte Carlo events in bin i from source j. The combined probability for the observed number of entries in data and Monte Carlo is then,

$$P_i = \frac{e^{\nu_i}{\nu_i}^{n_i}}{n_i!} \prod_{j=1}^{M} \frac{e^{-\mu_{ij}}(\mu_{ij})^{m_{ij}}}{m_{ij}!} \tag{6.7}$$

This is the probability we would like to use to construct a likelihood function.

As before, the goal is to determine the unknown factors r_j. Unfortunately the expected values μ_{ij} are also unknown (not to mention uninteresting). For N bins in the distribution, this leaves $M \times (N+1)$ unknown parameters and a formidable minimization problem.

In the first approach to making this problem tractable, we integrate over the unknown μ_{ij},

$$b_i = \int \cdots \int P_i d\mu_{i1} \ldots d\mu_{iM} \tag{6.8}$$

where the ν_i in the expression for P_i are replaced with the sum in equation 6.5. The integration can be performed analytically, and the result is given in reference [42]. The likelihood function to be maximized is then $\mathcal{L} = \prod_{i=1}^{N} b_i$.

Another approach has been proposed in reference [43], in which the authors have noted that the expected Monte Carlo values can be expressed,

$$\mu_{ij} = \frac{m_{ij}}{1 + r_j t_i} \tag{6.9}$$

where the t_i can be determined by solving the N independent equations,

$$\sum_{j}^{M} \frac{r_j m_{ij}}{1 + r_j t_i} = \frac{n_i}{1 - t_i} \tag{6.10}$$

In this case, the likelihood function $\mathcal{L} = \prod_{i=1}^{N} P_i$ is maximized, where at each step in the maximization process the μ_{ij} are computed by solving equations 6.10 and using equation 6.9.

As a test, these likelihoods have been used to fit samples created by a fast detector simulation which generates the distributions of polarization sensitive variables for each τ decay channel. The central values and errors from the fit were then compared to the generated central values and the spread of the of fitted values to check for bias and accurate error estimation. The central values and errors are found to be correct for samples with statistics comparable to those used in fitting the actual data and real detector Monte Carlo samples.

6.1.3 Charge identification

$\mathcal{P}_\tau(\cos\theta)$ is obtained by measuring the polarization in nine regions of $\cos\theta$. The angle θ is defined by the thrust axis of the event signed according to the event charge, where the event charge is the charge of the τ traveling into the $\cos\theta > 0$ hemisphere. For events with at least one $\tau^- \to \mu^- \bar{\nu}_\mu \nu_\tau$ decay, the event charge is assigned unambiguously by the muon chambers. For events with no identified muons but exactly one track in each hemisphere, the charge defined by the sign of the difference of curvatures weighted by resolutions for the two TEC tracks,

$$q \equiv \text{sign}\left(\frac{\mathcal{C}_1}{\delta\mathcal{C}_1} - \frac{\mathcal{C}_2}{\delta\mathcal{C}_2}\right) \tag{6.11}$$

where q is the charge, $\mathcal{C} = 1/P_T$ is proportional to the track curvature, and $\delta\mathcal{C}$ is the curvature resolution, measured using the techniques described in Chapter 5. By definition the thrust axis points in the direction of the hemisphere in which $\mathcal{C}_1$ lies, so that the quantity $q\cos\theta_{\text{thrust}}$ is always the charge in the $\cos\theta > 0$

hemisphere. For all remaining events, the charge is not defined and these are used for the measurement of the average polarization only.

Table 6.2 lists the charge confusion for various values of P_T and resolution, and shows the substantial improvement that results when both sides of an event are used.

Region	σ_{1/P_T} (GeV^{-1})	P_T side 1 (GeV)	P_T side 2 (GeV)	ϵ side 1	ϵ side 2	ϵ_q
Barrel	0.018	45	45	10.9%	10.9%	4.1%
		45	25	10.9%	1.3%	0.7%
		25	25	1.3%	1.3%	0.1%
	Average τ decay spectrum					1.2%
Endcap	0.06	20	20	20.3%	20.3%	12.0%
		20	15	20.3%	13.4%	8.5%
		20	10	20.3%	4.8%	3.9%
	Average τ decay spectrum					3.0%

Table 6.2: Charge confusion for various resolutions and transverse momenta. ϵ_q is the charge confusion when both sides of an event are used to determine the charge (equation 6.11). $\sigma_{1/P_T} = 0.018$ is the average resolution in the barrel and $\sigma_{1/P_T} = 0.06$ is roughly the average for the endcaps. The entries following the "Average τ decay spectrum" label give the charge confusion determined from Monte Carlo using the measured TEC resolution for an average τ decay energy spectrum.

6.1.4 Fitting with charge confusion

As described in detail in Chapter 2, charge confusion changes the shape of the $\mathcal{P}_\tau(\cos\theta)$ curve. This effect can be corrected in the fitting method. The technique essentially consists of applying the reweighting scheme described in section 6.1.1 in each $\cos\theta$ bin, except that the Monte Carlo distributions are weighted not only by the polarization but by charge confusion as well. This adds a layer of complexity to the fitting algorithm. Suppose, for example, we are trying to fit the polarization in a bin centered at $+\cos\theta$. Since the P_T distribution depends on the polarization, the

charge confusion also depends on polarization, so that the probability for events to migrate out of this bin and into the bin at $-\cos\theta$ is a function of the polarization in the $+\cos\theta$ bin. Similarly, the probability for events to migrate *into* the $+\cos\theta$ bin depends on the polarization in the $-\cos\theta$ bin. Therefore the polarizations in the $+\cos\theta$ and $-\cos\theta$ bins must be varied simultaneously in the fitting procedure. So extending the one-dimensional fit equations 6.1 and 6.2 to account for charge confusion leads to

$$\begin{aligned} N_i^{\theta+} &= r^{\theta+}\frac{1+\mathcal{P}_\tau^{\theta+}}{1+\mathcal{P}_\tau^{\mathrm{MC}}}m_{i+}^{\theta}\left(1-\epsilon_{i+}^{\theta+}\right) + r^{\theta+}\frac{1-\mathcal{P}_\tau^{\theta+}}{1-\mathcal{P}_\tau^{\mathrm{MC}}}m_{i-}^{\theta}\left(1-\epsilon_{i-}^{\theta+}\right) \\ &+ r^{\theta-}\frac{1+\mathcal{P}_\tau^{\theta-}}{1+\mathcal{P}_\tau^{\mathrm{MC}}}m_{i+}^{\theta}\left(\epsilon_{i+}^{\theta-}\right) + r^{\theta-}\frac{1-\mathcal{P}_\tau^{\theta-}}{1-\mathcal{P}_\tau^{\mathrm{MC}}}m_{i-}^{\theta}\left(\epsilon_{i-}^{\theta-}\right) \\ &+ \text{background} \end{aligned} \tag{6.12}$$

for the bin centered at $+\cos\theta$ and an analogous equation for the bin at $-\cos\theta$. The $\theta+$ and $\theta-$ superscripts indicate the $+\cos\theta$ and $-\cos\theta$ bins respectively, the ϵ terms give the charge confusion probability, and the r's are the normalization between data and Monte Carlo. The meaning of the subscripts is the same as in section 6.1.1. For example, $\epsilon_{i+}^{\theta+}$ is the charge confusion probability in energy bin i of the $+\cos\theta$ bin for the $h=+1$ decay spectrum. The first line of equation 6.12 is the usual reweighting of positive and negative helicity Monte Carlo spectra adjusted according to the migration of events out of the $+\cos\theta$ bin. The second line gives the contribution to the $+\cos\theta$ bin from events that migrate out of the $-\cos\theta$ bin. The helicity dependence of the ϵ terms is a result of the way charge is assigned; the charge confusion probability depends on the P_T distribution in the recoil hemisphere through equation 6.11. Note also that there is no sign on the θ superscript for the Monte Carlo distributions m_{i+} and m_{i-}. This is because we do not assign charge in the Monte Carlo, but instead combine the distributions for $+\cos\theta$ and $-\cos\theta$ into the m_{i+}^{θ} and m_{i-}^{θ}. Effects of charge confusion enter explicitly through the ϵ terms. Since the Monte Carlo distributions are combined in this way, we have $\mathcal{P}_\tau^{\mathrm{MC}\,\theta-} = \mathcal{P}_\tau^{\mathrm{MC}\,\theta+} = \mathcal{P}_\tau^{\mathrm{MC}}$, where $\mathcal{P}_\tau^{\mathrm{MC}}$ is just the average polarization used for generating the Monte Carlo.

To summarize, we account for charge confusion effects by simultaneously fitting bins centered at $+\cos\theta$ and $-\cos\theta$ using equation 6.12 and a corresponding equation for the $-\cos\theta$ bin. Each fit then contains twice as many parameters as does the fit described in section 6.1.1. The result of each fit is a pair for $\mathcal{P}_\tau$ values which are corrected for charge confusion. The Monte Carlo and background

normalizations also emerge in pairs from the fit. The method can be extended to higher dimensional fits, like those used for the $\tau^- \to \rho^-\nu_\tau$ and $\tau^- \to a_1^-\nu_\tau$ channels, by appending additional indices to the terms in equation 6.12.

The ϵ terms in equation 6.12 are determined for each channel, helicity, and $\cos\theta$ bin using a combination of Monte Carlo, the measured TEC resolution (Chapter 5), and the charge assignment method described in section 6.1.3. First the charge assignment is made for the channel of interest using the polarization sensitive variables, $\vec{\eta}$, observed in the selected hemisphere recoiling against an average $\vec{\eta}$ spectrum in the opposite hemisphere. This is done separately for each helicity. The result is compared to the true charge for the selected hemisphere, and thus the charge confusion probability is obtained as a function of $\vec{\eta}$. The correct P_T, θ, and ϕ dependence of the charge confusion is assured since the Monte Carlo spectra are resmeared according to the measured resolution, described in Chapter 5. The weights inserted into equation 6.11 come from the measured resolution function.

Figure 6.1 shows the estimated charge confusion as a function of $\vec{\eta}$ for the $\tau^- \to \rho^-\nu_\tau$ and $\tau^- \to \pi^-\nu_\tau$ channels in two bins of $\cos\theta$. The $|\cos\theta| < 0.12$ bin exhibits the largest charge confusion in the barrel, since in for a given P, P_T is highest in this region. The $0.72 < |\cos\theta| < 0.92$ range corresponds to the endcap, and therefore has considerably higher charge confusion. The upper two plots (a and b) correspond to the $\tau^- \to \pi^-\nu_\tau$ channel. The $h = +1$ distribution suffers slightly worse charge confusion than $h = -1$ because the $h = +1$ recoil spectrum is more energetic. Figure 6.1(c and d) show charge confusion as a function of $\cos\theta^*$ and $\cos\psi^*$ for the $\tau^- \to \rho^-\nu_\tau$ channel. Recalling that $\cos\theta^* \sim E_{\pi^-} + E_{\pi^0}$ and $\cos\psi^* \sim (E_{\pi^-} - E_{\pi^0})/E_\rho$, we see the charged pion energy is highest for $\cos\theta^* = 1$ and $\cos\psi^* = 1$. This observation is borne out in the figure, where the charge confusion is found to be highest in this region.

6.1.5 Uncertainty on charge confusion estimates

The accuracy of the charge confusion estimates described in the previous section depend on the accuracy with which the resolution of the central tracker is known. A systematic uncertainty on the resolution function results in a systematic uncertainty on the charge confusion, and a corresponding uncertainty in the correction for charge confusion.

Figure 6.2(b) shows the effect on charge confusion from varying the $\phi_{\rm local}$ dependence of the resolution function by it statistical error for the angular range $0.12 < |\cos\theta| < 0.35$. This amounts to roughly a 1% relative shift in the resolu-

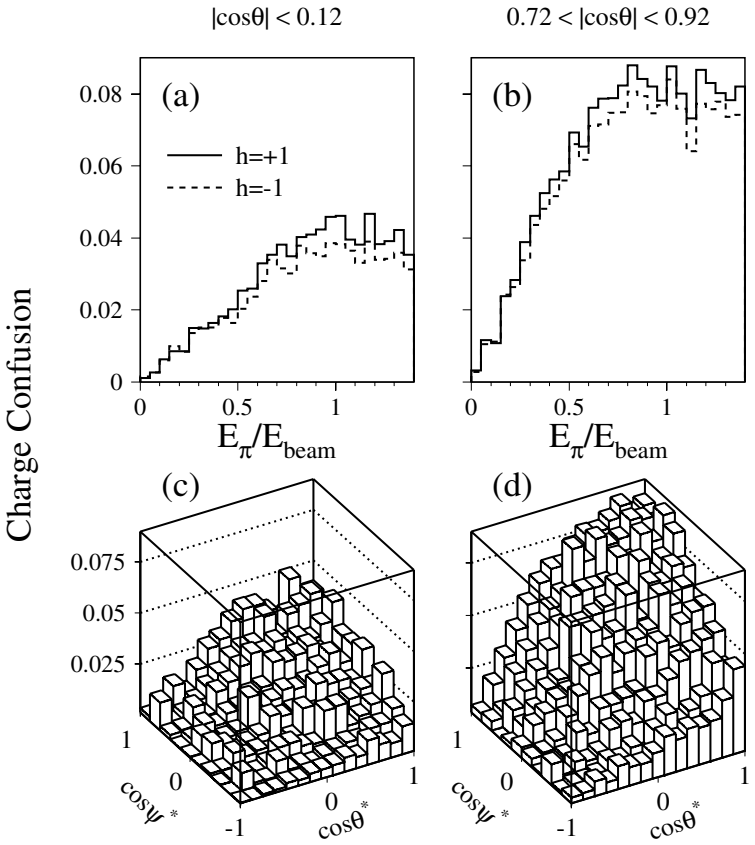

Figure 6.1: (a) and (b) show the charge confusion in the $\tau^- \to \pi^-\nu_\tau$ channel as a function of $x = E_\pi/E_{\rm beam}$ for two $\cos\theta$ bins. (c) and (d) show charge confusion in the $\tau^- \to \rho^-\nu_\tau$ channel as a function of $\cos\theta^*$ and $\cos\psi^*$.

tion.

The two helicity states are averaged for this figure. Also shown is the charge confusion that results if no additional smearing is applied to the results of the full detector simulation. This corresponds to about a 25% relative decrease in the measured resolution.

There are several sources of uncertainty in the θ dependence of the endcap resolution function which do not exist for the ϕ dependence. As discussed in section 5.1.5, the method used to determine resolution in the endcaps relies on the assumption that curvature resolution is normally distributed for some range of ϕ and track quality parameters. Furthermore, equation 5.4, which relates the charge

confusion probability to the number of events for which TEC measures the same charge on each side, is strictly valid only if the two tracks have the same curvature and if they traverse regions of the TEC with identical resolution. For example, contamination from radiative bhabhas can compromise the validity of equation 5.4. In addition, each $\cos\theta$ bin in which the resolution is estimated necessarily spans some range of anodes, so that the extracted resolution is in fact an average over this range. This also implies that the curvature resolution in a given $\cos\theta$ bin is in principle characterized by a sum of gaussian distributions, one for each anode.

The effects of these uncertainty sources were studied by varying the size of the $\cos\theta$ intervals, using several techniques to estimate $\mathcal{C}_0$ in equation 5.5, varying the fiducial volume cuts that remove regions of TEC with inferior resolution, and by varying the cut on acoplanarity. By far the largest effect comes from altering the acoplanarity cut. To estimate the size of the effect, we remove the acoplanarity cut completely, generate a new resolution curve, and insert it into the simulation. This new curve represents roughly a 10% relative increase in the measured resolution function. We cannot tighten the acoplanarity cut significantly since loss of statistics becomes pronounced as we approach the intrinsic ϕ resolution of TEC, which is a bit less than 1 mrad. Figure 6.2(a) shows the result of removing the acoplanarity cut used to generate the endcap resolution curve, as well as the effect of removing additional smearing altogether, which produces roughly a 25% change from the measured resolution.

6.1.6 Fit error

According to the central limit theorem, the likelihood function $\mathcal{L}$ will follow a gaussian distribution for sufficiently large statistics, so the log-likelihood function will have the form $\ln\mathcal{L} = -\ln\left(\sqrt{2\pi}\sigma\right) - (x-\langle x\rangle)^2/2\sigma^2$. Thus a 1σ shift in the central value $\langle x\rangle$ corresponds to a change of 0.5 in $\ln\mathcal{L}$. We therefore take the fit error to be the change in the polarization which decreases the log-likelihood function by 0.5.

The effect of limited Monte Carlo statics is built in to the fitting methods described in section 6.1.2. We can separate the data and Monte Carlo contributions to the total error by observing,

$$\begin{aligned} \sigma^2_{\text{total}} &= \sigma^2_{\text{data}} + \sigma^2_{\text{MC}} \\ &\approx (1+r)\,\sigma^2_{\text{MC}} \end{aligned} \tag{6.13}$$

where r is the ratio of data to Monte Carlo.

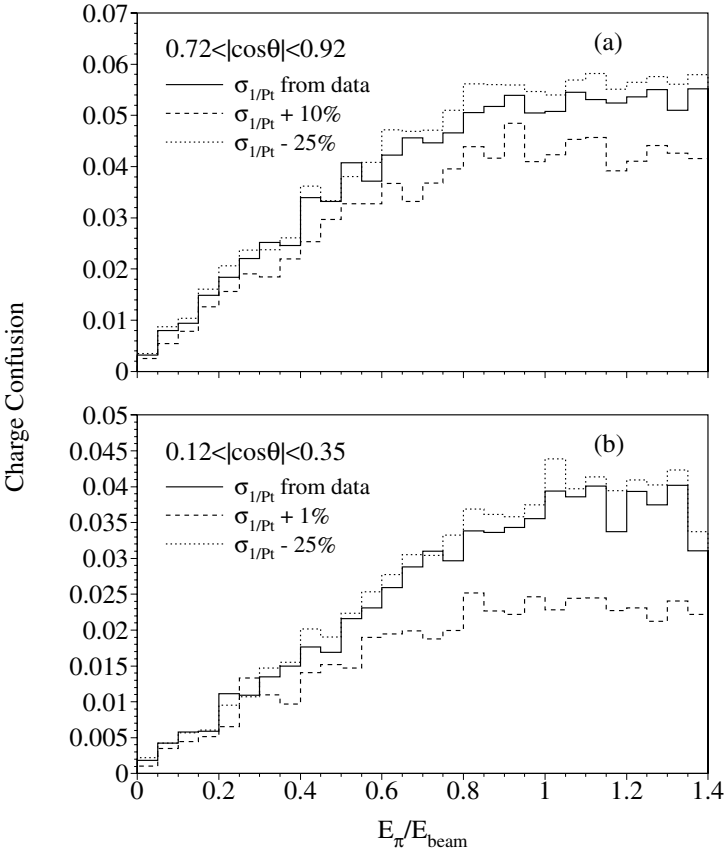

Figure 6.2: a) Charge confusion as a function of energy for pions averaged over both endcaps and both τ helicity states. The solid line shows the charge confusion estimated using the TEC resolution derived from data, and the dashed and dotted lines indicate the sensitivity of charge confusion to uncertainties in the resolution. $\sigma_{1/P_T} + 10\%$ corresponds to the resolution curve produced if no acoplanarity cut is used (roughly a 10% increase in the resolution). $\sigma_{1/P_T} - 25\%$ corresponds to the the resolution curve when no additional smearing is applied to the results of the Monte Carlo simulation. b) Charge confusion for pions in the range $0.12 < |\cos\theta| < 0.35$. $\sigma_{1/P_T} + 1\%$ corresponds to the resolution curve with an average value shifted by about 1% from the measured resolution. $\sigma_{1/P_T} - 25\%$ corresponds to the resolution curve when no additional smearing is applied to the Monte Carlo results.

6.2 Measurement of $\mathcal{P}_\tau$

Below we present the results of the $\mathcal{P}_\tau$ measurements for each of the five decay channels described in Chapter 2. A description of the fitting procedure, background estimation, and systematic errors is given. Systematic errors associated with the selection, background, and calibration are estimated by varying the most important selection cuts, the background contamination, and the energy scales of relevant subdetectors. The corresponding change in $\mathcal{P}_\tau$ represents the systematic error. These systematic errors are estimated using a fast detector simulation[3] which includes effects of acceptance, background, and energy scales. The fast simulation provides high statistics samples which make it possible to disentangle statistical fluctuations from real systematic effects. We also discuss the systematic errors associated with charge confusion and theory where relevant. All systematics are evaluated separately for each $\cos\theta$ bin.

6.2.1 Measurement of $\mathcal{P}_\tau$ from $\tau^- \to \mu^- \bar{\nu}_\mu \nu_\tau$

The muon transverse momentum is determined from the muon chamber measurement corrected for energy loss in the calorimeters. The muon energy is then computed using the measured polar angle. The $\mathcal{P}_\tau$ fits are performed in the region $|\cos\theta| < 0.81$, which corresponds to the acceptance of the muon chambers. Triplets can form only for $|\cos\theta| < 0.71$.

The shape of the dimuon background is estimated from data by selecting hemispheres which pass all the $\tau^- \to \mu^- \bar{\nu}_\mu \nu_\tau$ cuts except the cut which rejects hemispheres with $E_\mu > 40$ GeV on the opposite side. Instead the opposite hemisphere is required to contain an identified muon with energy measured by the muon chambers to be 40 GeV $< E_\mu <$ 50 GeV. The small contribution to the background shape from hemispheres with a high energy muon from $\tau^- \to \mu^- \bar{\nu}_\mu \nu_\tau$ on the opposite side is subtracted using Monte Carlo. A three-parameter fit is then performed in the region $0.05 < E_\mu / E_{\rm beam} < 1.1$ with $\mathcal{P}_\tau$, r, and the normalization for dimuon background as free parameters. The dimuon background normalization is then fixed to the fitted value, and a two-parameter fit is performed in the region $0.05 < E_\mu < 0.95$. In each of these steps, the background from other τ decays is varied simultaneously with the polarization. As a crosscheck, dimuon Monte Carlo

[3]This is in contrast to the full detector Monte Carlo, which produces the samples used for determining the polarization and statistical error.

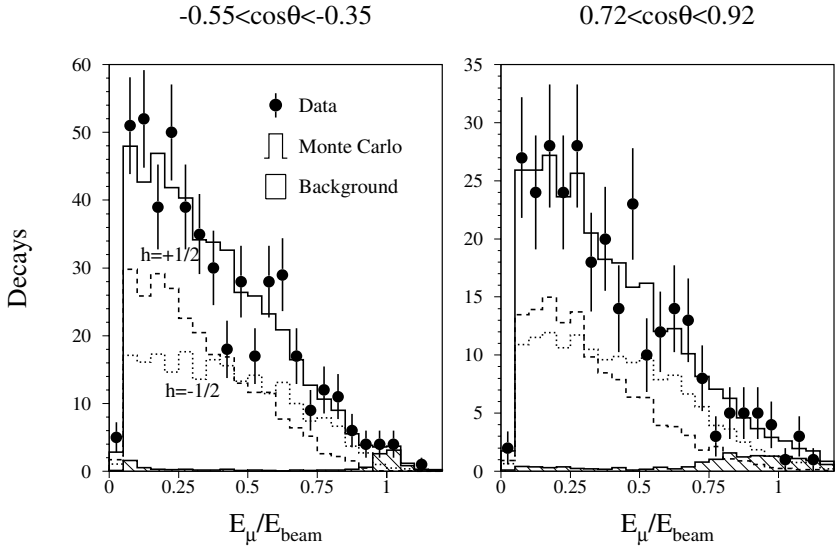

Figure 6.3: $\mathcal{P}_\tau$ measured in two ranges of $\cos\theta$. The data is from the 1993 sample.

events are also used to determine the dimuon background shape, and the results are found to be consistent.

The shape of the background from cosmic muons is estimated by selecting hemispheres which pass all the $\tau^- \to \mu^- \bar{\nu}_\mu \nu_\tau$ cuts except for the DCA cut, which is replaced by 5 mm < DCA < 15 mm. The normalization for the cosmic background is estimated by scaling the number of events observed in this DCA interval to the DCA interval used for the final $\tau^- \to \mu^- \bar{\nu}_\mu \nu_\tau$ selection. This approach is legitimate since the distribution of cosmics is uniform in DCA. The normalization for cosmic background is fixed in the fit.

The shape of the two-photon background is estimated by selecting hemispheres which pass all the $\tau^- \to \mu^- \bar{\nu}_\mu \nu_\tau$ cuts except for the acolinearity cut, which is replaced by $20° <$ acolinearity $< 80°$. Events that lie in this region are attributed to two-photon interactions. The normalization is estimated by scaling the observed number of events in this acolinearity interval to the interval used for the final $\tau^- \to \mu^- \bar{\nu}_\mu \nu_\tau$ selection. The normalization for two-photon background is fixed in the fit.

The muon chamber efficiency in the full detector Monte Carlo is checked against data, and an underestimation of the doublet to triplet ratio is observed. This is

corrected in each $\cos\theta$ bin by introducing additional momentum smearing to the appropriate number of randomly chosen triplet tracks. As described in Chapter 5, the resolution for doublets is considerably worse than for triplets. Figure 6.3 shows as an example the result of the polarization fit in two bins of $\cos\theta$, one of which lies in the triplet region of the muon chambers while the other corresponds to the doublet region $0.72 < \cos\theta < 0.92$. The wider distribution of the dimuon background in the doublet region is a result of the poorer resolution in this region.

Systematic errors associated with non-τ background are estimated by varying the normalizations on the various background contributions by their statistical uncertainties. This is done separately in each $\cos\theta$ bin. Typical uncertainty in background normalization is $10\% - 20\%$. The error from uncertainty in the background shape is negligible compared with the error due to uncertainty in the normalization. The systematic error due to uncertainty in background from other τ decay modes is estimated by varying the branching fractions of the background sources within their errors, as determined by other L3 measurements [44]. In the $\tau^- \to \mu^-\bar{\nu}_\mu\nu_\tau$ channel, most of the τ background comes from $\tau^- \to \pi^-\nu_\tau$ decays in which the hadronic shower is not completely contained in the calorimeters and produces a track in the muon chambers. The quadrature sum of the polarization errors arising from these various background sources gives the systematic error attached to background uncertainty.

The systematic error from uncertainty in the muon chamber momentum scale is estimated by varying this scale within the uncertainty derived from the dimuon study described in Chapter 5 and within the uncertainty on energy loss in the calorimeters, which is the dominant effect at low energies. The quadrature sum of the largest resulting polarization errors is the systematic error associated with energy scale.

The average polarization measured in the $\tau^- \to \mu^-\bar{\nu}_\mu\nu_\tau$ channel is $\mathcal{A}_\tau = 0.170 \pm .045$ where the error includes data and Monte Carlo statistics[4]. A fit to the angular dependence give $\mathcal{A}_e = 0.222 \pm .064$. The systematic errors for one $\cos\theta$ bin are summarized in Table 6.3. Figure 6.4 shows the average energy spectrum together with the best fit Monte Carlo distribution, the $h = +1/2$ and $h = -1/2$ contributions, and the non-τ background. Also shown in this figure is the $\mathcal{P}_\tau(\cos\theta)$ curve for $\tau^- \to \mu^-\bar{\nu}_\mu\nu_\tau$.

[4]This result and all subsequent individual channel results include radiative corrections. The correction is discussed in section 6.3.1.

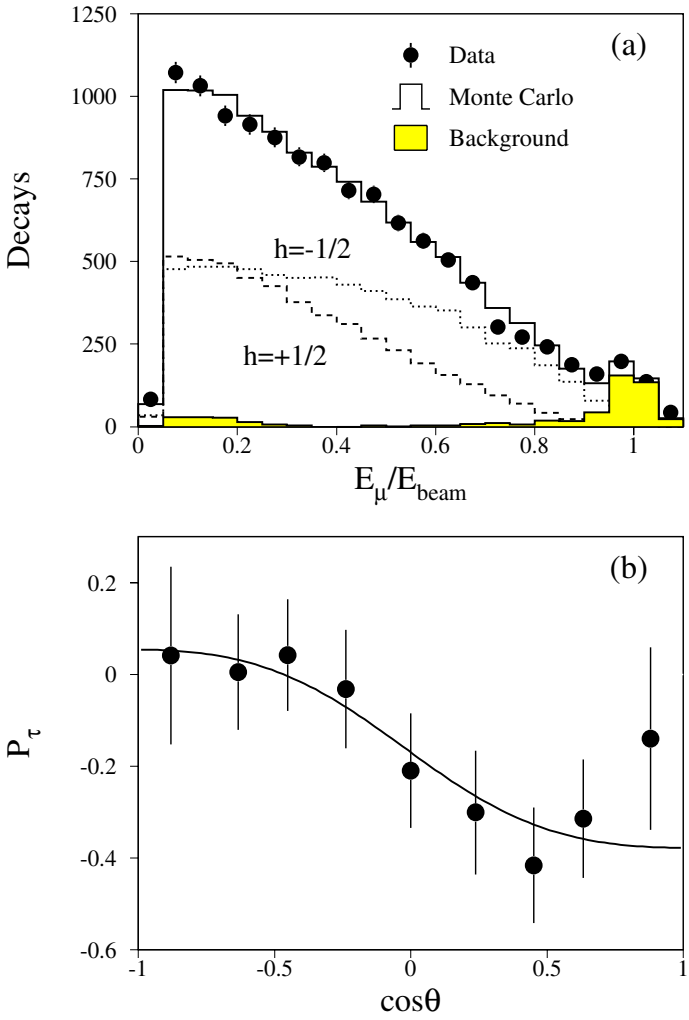

Figure 6.4: a) The average $E_\mu/E_{\rm beam}$ spectrum for $\tau^- \to \mu^- \bar{\nu}_\mu \nu_\tau$ decays showing the Monte Carlo best fit, the contribution from each helicity, and the non-τ background. b) $\mathcal{P}_\tau(\cos\theta)$ distribution together with the fitted curve for $\mathcal{A}_\tau$ and $\mathcal{A}_{\rm e}$. The error bars in this plot correspond to data and Monte Carlo statistics.

Source	$\Delta\mathcal{P}_\tau$
Background	0.022
Calibration	0.016
Selection	0.006

Table 6.3: Summary of systematic errors on $\mathcal{P}_\tau$ measured for the $\tau^- \to \mu^-\bar{\nu}_\mu\nu_\tau$ channel in the angular range $-0.72 < \cos\theta < -0.55$.

6.2.2 Measurement of $\mathcal{P}_\tau$ from $\tau^- \to e^-\bar{\nu}_e\nu_\tau$

Because of the high bhabha background in the endcap region, the measurement in this channel performed only in the range $\cos\theta < 0.7$. The electron energy determined from the BGO shower is the polarization sensitive variable.

The shape of the bhabha background is estimated from data by selecting hemispheres which pass all the $\tau^- \to e^-\bar{\nu}_e\nu_\tau$ cuts except the cut which rejects hemispheres with an identified electron on the opposite side whose energy exceeds 42 GeV. Instead the opposite hemisphere is required to contain an identified electron with energy $E_e > 42$ GeV. A three-parameter is performed in the region $0 < E_e/E_{\rm beam} < 1.1$ with $\mathcal{P}_\tau$, r, and the normalization for the bhabha background as free parameters. The bhabha background normalization is then fixed to the fitted value, and a two-parameter fit is performed in the region $0 < E_e/E_{\rm beam} < 0.92$. Background from other τ decays is varied simultaneously with the polarization.

The shape of the two-photon background is determined using a procedure analogous to that used for the $\tau^- \to \mu^-\bar{\nu}_\mu\nu_\tau$ channel.

Systematic errors associated with the non-τ background are estimated by varying the background contributions by the statistical uncertainty on their normalizations. Background from other τ decays is varied according to the uncertainty on the branching fractions of the background sources. The quadrature sum of the largest polarization change resulting from these variations in the background sources represents the systematic error associated with background.

The accuracy of the BGO energy scale is estimated at high energies from a study of bhabha events and at low energies from the position of the π^0 peak, as discussed in Chapter 5. The systematic error from calibration is evaluated assuming the worst case combination of high and low energy scale shifts, with a

linear interpolation between the two extremes[5].

To a good approximation, the net effect of charge confusion on the fitted polarization in a given channel is proportional the product of the average charge confusion for events containing that decay channel and the difference of polarizations is oppositely signed $\cos\theta$ bins. The principles that underlie this are discussed in section 2.6.4. Based on observations discussed in section 6.1.5, we conservatively take the uncertainty on charge confusion to be half the charge confusion itself. Using this uncertainty and the polarization difference in oppositely signed $\cos\theta$ bins gives an estimate of the uncertainty in the correction for charge confusion.

The results of the polarization fit in the $\tau^- \to e^-\bar{\nu}_e\nu_\tau$ channel are $\mathcal{A}_\tau = .114 \pm .049$ and $\mathcal{A}_e = 0.253 \pm .074$, where the error includes data and Monte Carlo statistics. Table 6.4 summarizes the systematic errors for one $\cos\theta$ bin. Figure 6.5 shows the average energy spectrum and the $\mathcal{P}_\tau(\cos\theta)$ distribution.

Source	$\Delta\mathcal{P}_\tau$
Background	0.017
Calibration	0.014
Selection	0.010
Charge Confusion	0.002

Table 6.4: Summary of systematic errors on $\mathcal{P}_\tau$ measured for the $\tau^- \to e^-\bar{\nu}_e\nu_\tau$ channel in the angular range $-0.72 < \cos\theta < -0.55$.

6.2.3 Measurement of $\mathcal{P}_\tau$ from $\tau^- \to \pi^-\nu_\tau$

The pion energy is calculated using a combination of the tracking and calorimeters, as described in section 5.5. The polarization is determined from a two-parameter fit in the range $0.044 < E_\pi < 1.32$ with $\mathcal{P}_\tau$ and r as free parameters. Background from other τ decays is varied simultaneously with the polarization. The energy spectrum is histogrammed using wider bins at high energies than at low energies in order to reduce the effects of resolution. The individual bin sizes are chosen to follow the charged pion energy resolution, shown in in Figure 5.25.

[5]This produces a larger change in $\mathcal{P}_\tau$ than a logarithmic dependence.

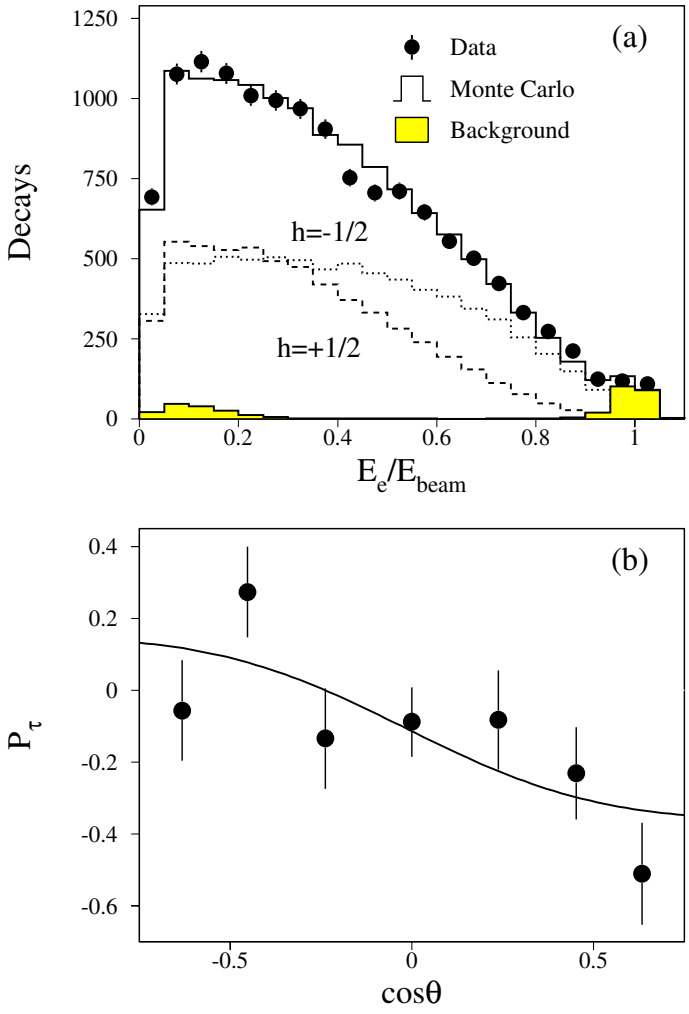

Figure 6.5: a) The average $E_e/E_{\rm beam}$ spectrum for $\tau^- \to {\rm e}^-\bar{\nu}_{\rm e}\nu_\tau$ decays showing the Monte Carlo best fit, the contribution from each helicity, and the non-τ background. b) $\mathcal{P}_\tau(\cos\theta)$ distribution together with the fitted curve for $\mathcal{A}_\tau$ and $\mathcal{A}_{\rm e}$. The error bars correspond to data and Monte Carlo statistics.

The dimuon background shape is estimated by selecting hemispheres which pass all of the $\tau^- \to \pi^-\nu_\tau$ selection criteria except the cut which rejects events with an identified muon on the opposite side whose energy exceeds 42 GeV. Instead the opposite hemisphere is required to contain an identified muon with $E_\mu > 42$ GeV. The small contribution to the background shape from events with a $\tau^- \to \mu^-\bar{\nu}_\mu\nu_\tau$ decay on the opposite side is subtracted using the Monte Carlo $Z \to \tau^+\tau^-$ sample. The dimuon background normalization is taken as the fraction of entries in an independently selected $Z \to \mu^+\mu^-$ spectrum with $E_\mu < 42$ GeV.

Estimation of the bhabha background is analogous to the dimuon background estimation. Two-photon and cosmic background are estimated in the same way as for the $\tau^- \to \mu^-\bar{\nu}_\mu\nu_\tau$ and $\tau^- \to e^-\bar{\nu}_e\nu_\tau$ modes. The normalizations for dimuon, bhabha, two-photon, and cosmic background are fixed in the polarization fit.

The systematic error associated with background from other τ decays is determined by varying the branching fractions for $\tau^- \to \rho^-\nu_\tau$ and $\tau^- \to a_1^-\nu_\tau$ by their uncertainties. The systematic error from non-τ background sources is estimated by varying the normalization for these sources within their statistical uncertainty.

The estimation of the systematic error on the correction for charge confusion is is analogous to the estimation in the $\tau^- \to e^-\bar{\nu}_e\nu_\tau$ channel.

Systematic error associated with calibration arises from uncertainty in the energy scale of the calorimeters for charged hadrons and uncertainty in TEC momentum scale, which affects the pion energy measurement at low energies. The accuracy of the TEC scale at low momentum is estimated low energy electrons and $\tau^- \to \mu^-\bar{\nu}_\mu\nu_\tau$ decays, and the energy scales of the BGO and hadron calorimeter for hadrons are known from the position of the ρ invariant mass peak. This is discussed in Chapter 5. The TEC and calorimetry scales are varied within their errors and the quadrature sum of the largest changes in the fitted polarization is taken as the systematic error. There is also a small polarization uncertainty in this channel associated with structure dependent radiation [47] which we quote as theory error.

The results of the polarization fit in the $\tau^- \to \rho^-\nu_\tau$ channel are $\mathcal{A}_\tau = .155 \pm .017$ and $\mathcal{A}_e = 0.151 \pm .027$, where the error includes data and Monte Carlo statistics. Table 6.5 summarizes the systematic errors for one $\cos\theta$ bin. Figure 6.6 shows the average energy spectrum and the $\mathcal{P}_\tau(\cos\theta)$ distribution.

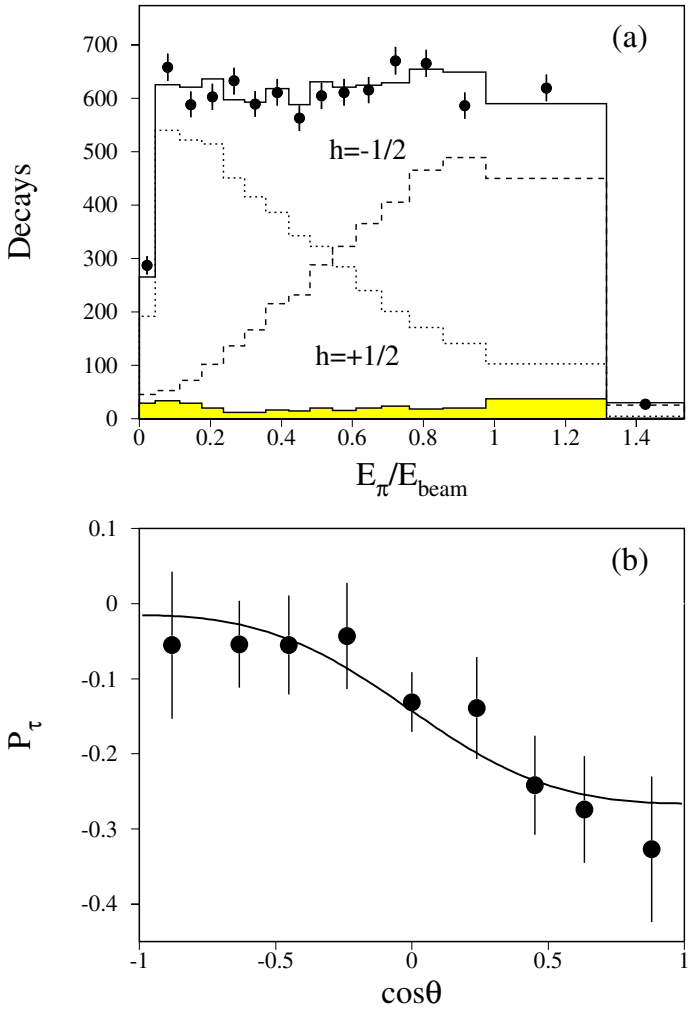

Figure 6.6: a) The average $E_\pi/E_{\rm beam}$ spectrum for $\tau^- \to \pi^-\nu_\tau$ decays showing the Monte Carlo best fit, the contribution from each helicity, and the non-τ background. Nonequidistant binning is used to reduce the effect of resolution at high energies. b) $\mathcal{P}_\tau(\cos\theta)$ distribution together with the fitted curve for $\mathcal{A}_\tau$ and $\mathcal{A}_{\rm e}$. The error bars correspond to data and Monte Carlo statistics.

Source	$\Delta\mathcal{P}_\tau$
Background	0.008
Calibration	0.026
Selection	0.007
Charge Confusion	0.003
Theory	0.002

Table 6.5: Summary of systematic errors on $\mathcal{P}_\tau$ measured for the $\tau^- \to \pi^-\nu_\tau$ channel in the angular range $-0.72 < \cos\theta < -0.55$.

6.2.4 Measurement of $\mathcal{P}_\tau$ from $\tau^- \to \rho^-\nu_\tau$

The polarization sensitive quantities $\cos\theta^*$ and $\cos\psi^*$ are computed from the measured energies and momenta of the charged and neutral pions. The charged and neutral pion energies are determined from the neutral reconstruction algorithm described in section 4.2.3. A two-parameter fit is performed using a 10×15 matrix in the parameter space of $\cos\theta^*$ and $\cos\psi^*$, with $\mathcal{P}_\tau$ and r as the free parameters. Background from other τ decays is varied simultaneously with the polarization.

The procedure for estimating non-τ background is analogous to that used for the $\tau^- \to \pi^-\nu_\tau$ channel. The associated systematic error is determined by varying this background within the uncertainty on the normalization. Most of the τ background comes from 1-prong $\tau^- \to a_1^-\nu_\tau$ decays. The systematic error associated with uncertainty in this contribution is estimated by varying the $\tau^- \to a_1^-\nu_\tau$ branching ratio within its error.

Systematics from calibration are similar to those in the $\tau^- \to \pi^-\nu_\tau$ channel, except that uncertainty in the BGO scale for the π^0 energy measurement is taken into account. The results of the polarization fits in the $\tau^- \to \rho^-\nu_\tau$ channel are $\mathcal{A}_\tau = 0.155 \pm 0.017$ and $\mathcal{A}_e = 0.151 \pm 0.027$. Figure 6.7 shows the $\cos\psi^*$ distribution in several bins of $\cos\theta^*$. The ranges $\cos\theta^*$ are chosen to bring out the features of the $\cos\psi^*$ distributions that provide sensitivity to the τ polarization. Table 6.6 summarizes the systematic errors for one $\cos\theta$ bin. Figure 6.8 shows the angular dependence of the polarization in the $\tau^- \to \rho^-\nu_\tau$ channel.

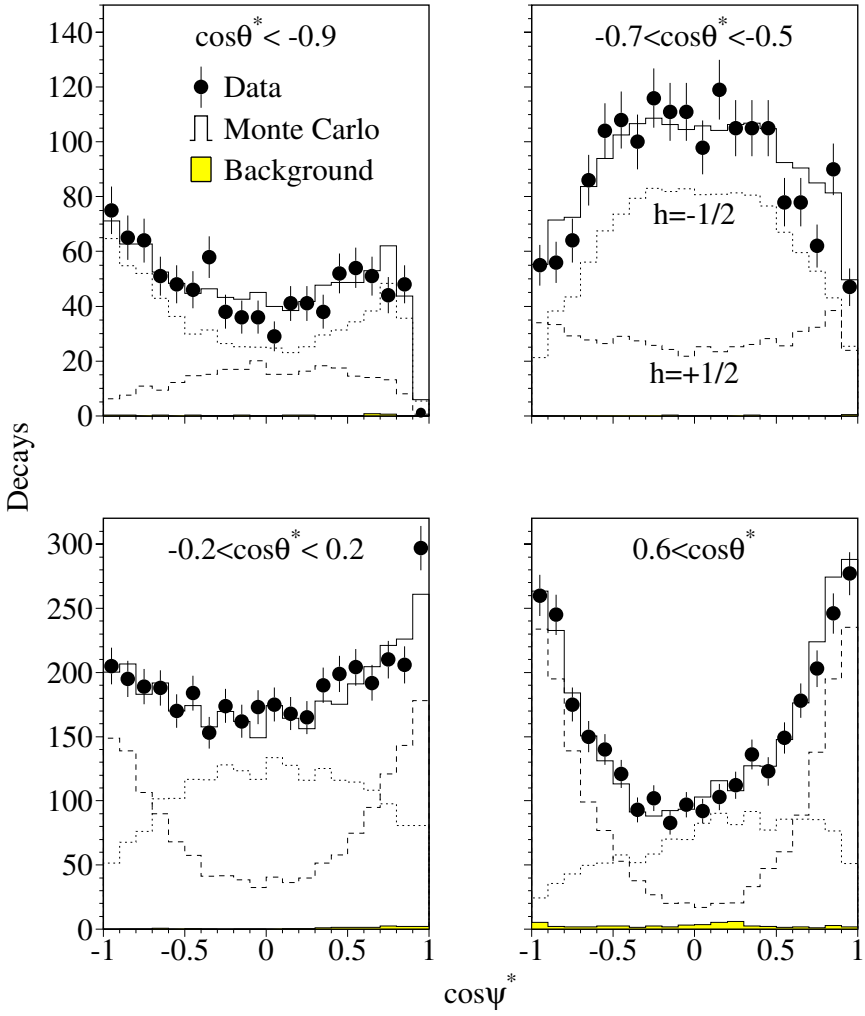

Figure 6.7: The spectra for $\tau^- \to \rho^- \nu_\tau$ decays as a function ofcos ψ^* in four ranges of cos θ^*.

Source	$\Delta\mathcal{P}_\tau$
Background	0.004
Calibration	0.014
Selection	0.008
Charge Confusion	0.002

Table 6.6: Summary of systematic errors on $\mathcal{P}_\tau$ measured for the $\tau^- \to \rho^-\nu_\tau$ channel in the angular range $-0.72 < \cos\theta < -0.55$.

6.2.5 Measurement of $\mathcal{P}_\tau$ from $\tau^- \to a_1^-\nu_\tau$

For the polarization measurement in this channel we combine six polarization sensitive observables which correspond to three angles and three invariant masses, into a single parameter, ω_{a_1}, as described in section 2.4. A two parameter fit is performed for $-1 < \omega_{a_1} < 1$ with $\mathcal{P}_\tau$ and r as the free parameters. Background from other τ decays is varied simultaneously with the polarization.

Non-τ background is negligible for this channel. The systematic error associated with background from $\tau^- \to \rho^-\nu_\tau$ and nonresonant decays is estimated by varying the corresponding branching fractions within their errors.

A study of the hadronic structure functions of the a_1 has been performed [48] to discriminate between various theoretical models [49]. The L3 data are in qualitative agreement with the model proposed by Kühn and Mirkes, which is therefore used in the analysis. Uncertainty associated with this model dependence is quoted as theory error.

The results of the polarization fits in the $\tau^- \to a_1^-\nu_\tau$ channel are $\mathcal{A}_\tau = 0.254 \pm 0.128$ and $\mathcal{A}_e = 0.240 \pm 0.211$. Table 6.7 summarizes the systematic errors for one $\cos\theta$ bin. Figure 6.9 shows the average energy spectrum and the $\mathcal{P}_\tau(\cos\theta)$ distribution.

6.3 Determination of $\mathcal{A}_\tau$ and $\mathcal{A}_e$

We now outline how the individual channel measurements described above are corrected for radiative effects and combined into a single $\mathcal{P}_\tau(\cos\theta)$ distribution from which $\mathcal{A}_\tau$ and $\mathcal{A}_e$ are determined.

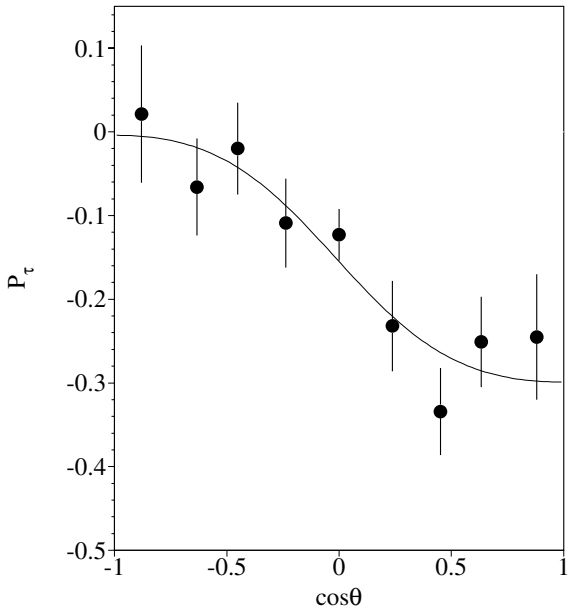

Figure 6.8: $\mathcal{P}_\tau(\cos\theta)$ for the $\tau^- \to \rho^-\nu_\tau$ channel.

6.3.1 Radiative corrections

The individual channel results described above do not take into account the effects of initial and final state radiation, γ-exchange, and γ-Z interference. Since equation 1.32 neglects radiative corrections, it is necessary to correct the $\mathcal{P}_\tau(\cos\theta)$ distribution for these effects before fitting for $\mathcal{A}_\tau$ and $\mathcal{A}_e$. The corrections are calculated for each $\cos\theta$ bin using the analytical program ZFITTER [45], which takes into account initial and final state radiation and their interference to $\mathcal{O}(\alpha^2)$, as well as the contributions from γ-exchange and γ-Z interference. As these corrections show a strong $\sqrt{s}$ dependence, they are computed at each $\sqrt{s}$ point and averaged weighted by the integrated luminosity at these points. A detailed description of this procedure is given in reference [46].

The results for $\mathcal{A}_\tau$ and $\mathcal{A}_e$ extracted from the corrected $\mathcal{P}_\tau(\cos\theta)$ distributions are summarized in Figure 6.10.

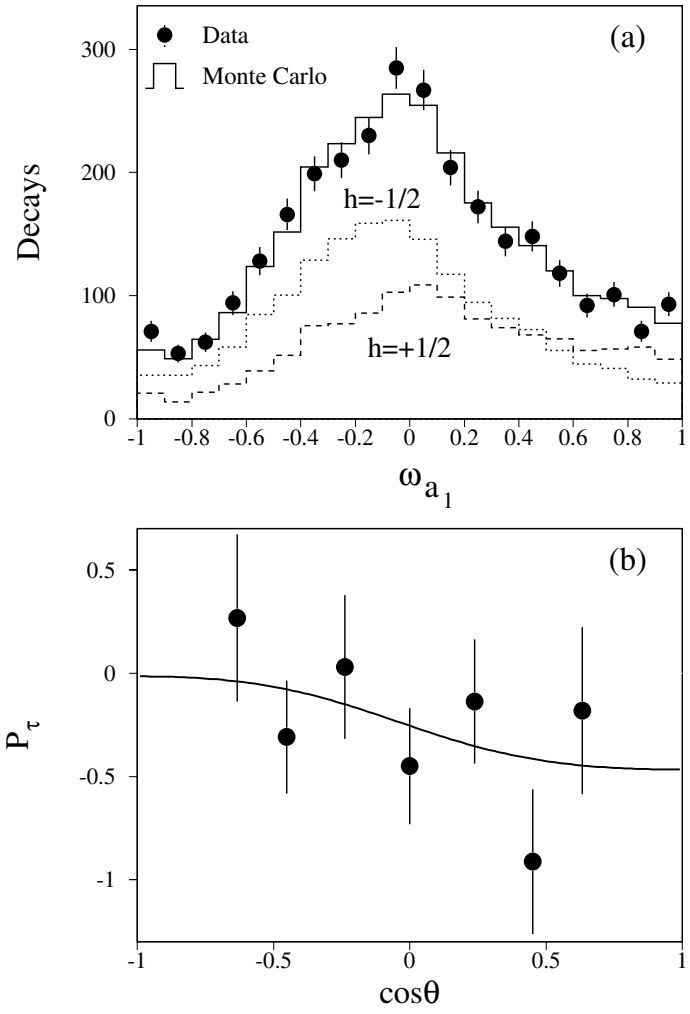

Figure 6.9: a) The average ω_{a_1} spectrum for $\tau^- \to a_1$ decays showing the Monte Carlo best fit, the contribution from each helicity, and the non-τ background. b) $\mathcal{P}_\tau(\cos\theta)$ distribution together with the fitted curve for $\mathcal{A}_\tau$ and $\mathcal{A}_e$. The error bars correspond to data and Monte Carlo statistics.

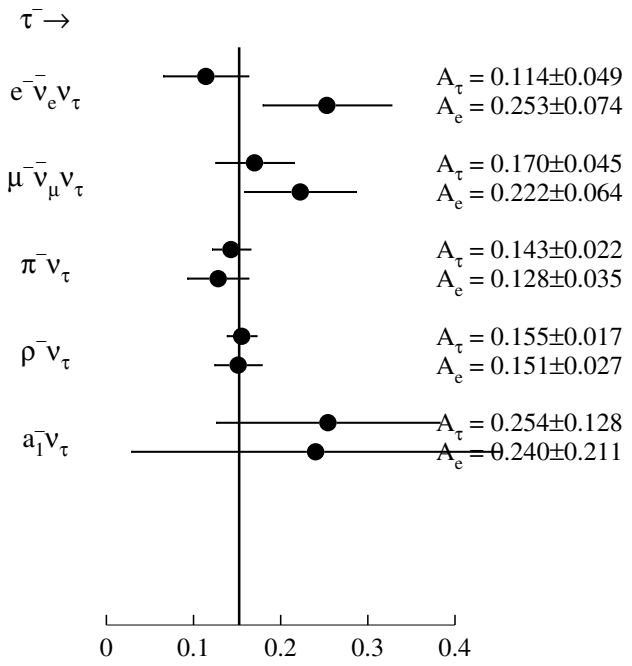

Figure 6.10: $\mathcal{A}_\tau$ and $\mathcal{A}_e$ for each channel. The errors correspond to data and Monte Carlo statistics and do not take into account the statistical correlation when both τ's in an event are selected for the polarization measurement. The vertical line shows the value for the combined result with the assumption of $e - \tau$ universality (see section 6.3.3).

Source	$\Delta\mathcal{P}_\tau$
Background	0.010
Calibration	0.020
Selection	0.020
Charge Confusion	0.002
Theory	0.015

Table 6.7: Summary of systematic errors on $\mathcal{P}_\tau$ measured for the $\tau^- \to a_1^-\nu_\tau$ channel in the angular range $-0.72 < \cos\theta < -0.55$.

6.3.2 Combination of individual channel results and statistical correlations

In the results presented so far, we have assumed that the decay spectra for the two τ's produced in a $Z \to \tau^+\tau^-$ event are statistically independent. This is not true since helicity conservation in the high energy limit requires that the two τ helicities be opposite. Since the τ helicities in a given event are fully correlated, the τ decay spectra on the two sides are also correlated. Consider for example an event with a $\tau^- \to \pi^-\nu_\tau$ decay in each hemisphere. If the pion energy on one side is high, the energy on the opposite side tends to be high as well. Thus simply combining all the hemispheres to produce an average spectrum and inserting this into the fitting procedures described above leads to an underestimation of the statistical error. We account for this in the bin-by-bin combination of the individual channel results.

Ultimately we have to compute a correlated weighted average for events in which both sides are used in the polarization measurement. The required formula can be motivated using the maximum likelihood technique. For the case of two observables with with correlation coefficient ρ, the probability to measure values x_1 and x_2 follows the binormal distribution,

$$\begin{aligned} P(x_1,x_2) &= \mathcal{N}\exp\left\{-\frac{1}{2\,(1-\rho^2)}\left[\left(\frac{x_1-\mu}{\sigma_{x_1}}\right)^2+\left(\frac{x_2-\mu}{\sigma_{x_2}}\right)^2\right.\right. \\ &- \left.\left. 2\rho\left(\frac{x_1-\mu}{\sigma_{x_1}}\right)\left(\frac{x_2-\mu}{\sigma_{x_2}}\right)\right]\right\} \end{aligned} \tag{6.14}$$

where $\mathcal{N}$ is the normalization and μ is the expected value for the two measurements. In our case, μ is the expected value for $\mathcal{P}_\tau$ and x_1 and x_2 are the polarization values measured in the two hemispheres of a $Z \to \tau^+\tau^-$ decay. We use $P(x_1, x_2)$ to construct the negative log-likelihood function, $-\ln \mathcal{L} = -\ln P(x_1, x_2)$, then minimize it to find an estimator for μ. The result is,

$$\mu = \left(\frac{1}{\sigma_{x_1}^2} + \frac{1}{\sigma_{x_2}^2} - \frac{2\rho}{\sigma_{x_1}\sigma_{x_2}} \right)^{-1} \left[\frac{x_1}{\sigma_{x_1}^2} + \frac{x_2}{\sigma_{x_2}^2} - \frac{\rho}{\sigma_{x_1}\sigma_{x_2}} (x_1 + x_2) \right] \tag{6.15}$$

The combined error from the two observations is,

$$\frac{1}{\sigma^2} = \left\langle -\frac{\partial^2 \mathcal{L}}{\partial \mu^2} \right\rangle = \frac{1}{1-\rho^2} \left(\frac{1}{\sigma_{x_1}^2} + \frac{1}{\sigma_{x_2}^2} - \frac{2\rho}{\sigma_{x_1}\sigma_{x_2}} \right) \tag{6.16}$$

Equations 6.14 and 6.16 can be used to combine the central values and errors in the polarization measurement for one specific channel recoiling against another specific channel. Take the case of $\tau^- \to \pi^-\nu_\tau$ decays recoiling against $\tau^- \to e^-\bar{\nu}_e\nu_\tau$ decays. In this case σ_{x_1} is the error on the polarization derived from the pion spectrum for events with an electron in the opposite hemisphere; we estimate this as $\sigma_{x_1} \approx \sigma_\pi/\sqrt{B_e\epsilon_e}$ where σ_π is the error on the polarization measurement using all $\tau^- \to \pi^-\nu_\tau$ decays, B_e is the branching ratio for $\tau^- \to e^-\bar{\nu}_e\nu_\tau$, and ϵ_e is the electron selection efficiency for the $\cos\theta$ bin in question. Similarly $\sigma_{x_2} \approx \sigma_e/\sqrt{B_\pi\epsilon_\pi}$.

More generally, the combined error for channel i against channel j is,

$$\frac{1}{\sigma_{i-j}^2} = \frac{1}{1-\rho_{i-j}^2} \left(\frac{B_j\epsilon_j}{\sigma_i^2} + \frac{B_i\epsilon_i}{\sigma_j^2} - \frac{2\rho_{i-j}}{\sigma_{x_i}\sigma_{x_j}} \right) \tag{6.17}$$

where ρ_{i-j} is the correlation coefficient for events containing channel i in one hemisphere and channel j in the other. In the case of events with a decay from channel i on one side and an undefined decay on the opposite side, an error $\sigma_i/\sqrt{1 - 2B_i\epsilon_i - \sum_j B_j\epsilon_j}$ is assigned; there is no correlation term in this case.

The various σ_{i-j} share no common events, so they can be combined without correlation terms,

$$\frac{1}{\sigma^2} = \sum_{i=1}^{N_{\text{chnl}}} \sum_{j=i}^{N_{\text{chnl}}} \frac{1}{\sigma_{i-j}} \tag{6.18}$$

where N_{chnl} is the number of channels and includes the cases where one side is not defined, as described above.

The correlation matrix ρ_{i-j} is estimated using a fast detector simulation which includes the effects of resolution and acceptance. The error matrix E_{ij} can be determined from N simulated measurements according to,

$$E_{ij} = \frac{1}{N}\sum_{k=1}^{N}\left(\mathcal{P}_{\tau k}^{\ i} - \left\langle \mathcal{P}_\tau^{\ i}\right\rangle\right)\left(\mathcal{P}_{\tau k}^{\ j} - \left\langle \mathcal{P}_\tau^{\ j}\right\rangle\right) \tag{6.19}$$

where $\mathcal{P}_{\tau k}^{\ i}$ is the result of the k'th polarization measurement using channel i and $\left\langle \mathcal{P}_\tau^{\ i}\right\rangle$ is the average polarization measured for channel i. The correlation coefficients are then simply extracted from E_{ij} using $\rho_{i-j} \equiv \sigma_{ij}^2/\sigma_i\sigma_j$. Table 6.8 gives a summary of the ρ_{i-j}.

Decay channels	ρ_{i-j}
$\pi - \pi$	0.20
$\rho - \rho$	0.12
$\rho - \pi$	0.16
$e,\mu - \pi$	0.01
$e,\mu - e,\mu$	0.03
$e,\mu - \rho$	0.01

Table 6.8: Correlation coefficients used in combining individual channel results.

This procedure for combining the individual channel results is applied separately in each $\cos\theta$ bin. The systematic error is then computed in each bin for each uncertainty source by combining the systematic errors for the individual channels. This procedure accounts for the relative contribution of each channel, the correlations in the energy scale systematic errors (see section 2.6.3), and the correlation of the charge confusion systematics among all channels except $\tau^- \to \mu^-\bar{\nu}_\mu\nu_\tau$. Other systematic errors are assumed to be uncorrelated in a given $\cos\theta$ bin and are added in quadrature.

6.3.3 Fit for $\mathcal{A}_\tau$ and $\mathcal{A}_e$

$\mathcal{A}_\tau$ and $\mathcal{A}_e$ are determined by fitting Equation 1.32 to the combined, corrected $\mathcal{P}_\tau(\cos\theta)$ distribution. The systematic errors on $\mathcal{A}_\tau$ and $\mathcal{A}_e$ are estimated using the

systematic uncertainties in each $\cos\theta$ bin, taking account of bin-to-bin correlations for the different uncertainty sources.

Systematic error associated with calibration affects the energy distributions for the τ^+ and the τ^- in the same way. Therefore these errors are correlated between $\cos\theta$ bins of opposite sign; there is no correlation between neighboring bins. As a result, calibration uncertainties do not, to first order, contribute to the systematic error on $\mathcal{A}_e$.

Theory errors result in an uncertainty in the energy spectra for $\tau^- \to \pi^-\nu_\tau$ and $\tau^- \to a_1^-\nu_\tau$ which is the same in $\cos\theta$ bin. Therefore these errors are assumed to be fully correlated, so that they affect $\mathcal{A}_e$ and not $\mathcal{A}_\tau$.

The correction for charge confusion moves the polarization in $\cos\theta > 0$ bins in the opposite direction from the polarization in $\cos\theta < 0$ bins. As discussed in section 2.6.4, this shift is nearly symmetric around the average value of $\mathcal{P}_\tau(\cos\theta)$. Thus the uncertainty on the charge confusion correction affects $\mathcal{A}_e$ and not $\mathcal{A}_\tau$.

If the systematic errors associated with selection are fully correlated among the θ bins, they will shift the polarization in each bin in the same way, causing a change in $\mathcal{A}_\tau$ but no change in $\mathcal{A}_e$. On the other hand if there is no correlation between $\cos\theta$ bins, the effect on $\mathcal{A}_\tau$ will be smaller and the effect on $\mathcal{A}_e$ larger. It is difficult to make a reliable estimate of the degree of correlation among selection efficiency errors, so we make the worst case assumption that the errors are fully correlated for the $\mathcal{A}_\tau$ measurement and uncorrelated for the $\mathcal{A}_e$ measurement.

Systematic uncertainties from background estimation in the different $\cos\theta$ bins are assumed to be uncorrelated.

The uncertainties on $\mathcal{A}_e$ and $\mathcal{A}_\tau$ from uncorrelated systematic errors in the $\cos\theta$ bins are determined from the error that results when each point in the $\mathcal{P}_\tau(\cos\theta)$ distribution is weighted in the fit by its estimated systematic error. The uncertainties on $\mathcal{A}_e$ and $\mathcal{A}_\tau$ from the fully correlated systematics are estimated by shifting the polarization in each $\cos\theta$ by its estimated error; the direction of the shift is determined from the nature of the correlation, as discussed above. The change in the fitted value for $\mathcal{A}_\tau$ or $\mathcal{A}_e$ is then the systematic error. The systematic errors on $\mathcal{A}_{e-\tau}$ are estimated following the same basic prescription, except that we set $\mathcal{A}_e = \mathcal{A}_\tau$ in the fit. Table 6.9 summarizes the statistical and systematic errors for $\mathcal{A}_\tau$ and $\mathcal{A}_e$.

The final result of the fit is,

$$\begin{aligned} \mathcal{A}_\tau &= 0.150 \pm 0.013 \pm 0.009 \\ \mathcal{A}_e &= 0.157 \pm 0.020 \pm 0.005 \end{aligned}$$

error from	$\mathcal{A}_\tau$	$\mathcal{A}_e$	$\mathcal{A}_{e-\tau}$
data statistics	0.012	0.019	0.010
Monte Carlo statistics	0.004	0.007	0.004
selection	0.005	0.002	0.004
background	0.002	0.002	0.001
calibration	0.007	0.000	0.005
charge confusion	0.000	0.004	0.001
theory	0.001	0.000	0.001

Table 6.9: Summary of statistical and systematic errors for $\mathcal{A}_\tau$, $\mathcal{A}_e$ and $\mathcal{A}_{e-\tau}$.

where the first error includes data and Monte Carlo statistics and the second error is systematic. Setting $\mathcal{A}_\tau = \mathcal{A}_e$ in the fit yields,

$$\mathcal{A}_{e-\tau} \quad = \quad 0.152 \pm 0.011 \pm 0.007$$

The corrected $\mathcal{P}_\tau$ points and the fitted curves with and without the assumption of universality are shown in Figure 6.11.

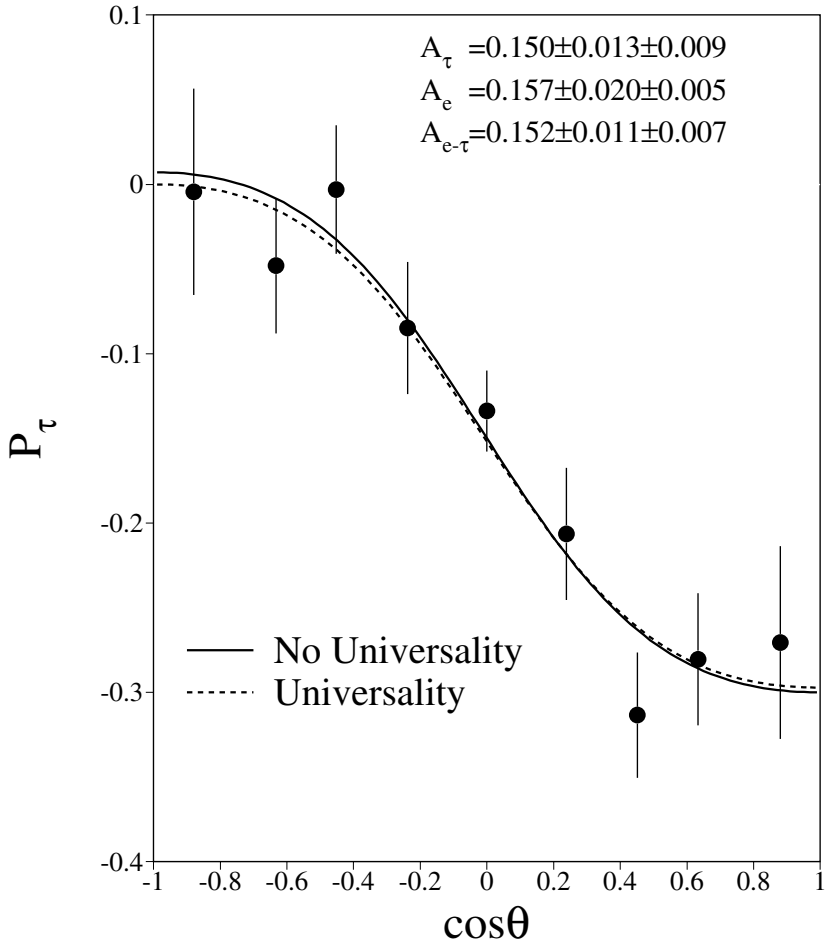

Figure 6.11: $\mathcal{P}_\tau(\cos\theta)$ distribution for all channels combined. The solid and dashed lines show the results of the fit using equation 1.32 with and without the assumption of lepton universality. The error bars include the data and Monte Carlo statistics only. $\mathcal{P}_\tau(\cos\theta)$ is corrected bin-by-bin for initial and final state radiation, γ-exchange, and γ-Z interference.

Chapter 7

Conclusions

The measured asymmetries reported in the previous chapter,

$$\begin{aligned} \mathcal{A}_\tau &= 0.150 \pm 0.013 \pm 0.009 \\ \mathcal{A}_{\rm e} &= 0.157 \pm 0.020 \pm 0.005 \\ \mathcal{A}_{{\rm e}-\tau} &= 0.152 \pm 0.011 \pm 0.007 \end{aligned}$$

are used in equation 1.33 to determine ratio of vector- to axial-vector coupling constants. The result is,

$$\begin{aligned} g_V^\tau / g_A^\tau &= 0.0791 \pm 0.0099 \pm 0.0025 \\ g_V^{\rm e} / g_A^{\rm e} &= 0.0752 \pm 0.0063 \pm 0.0045 \end{aligned}$$

where the first error includes data and Monte Carlo statistics and the second error is a combination of all systematics. This result is consistent with the hypothesis of lepton universality:

$$\frac{g_V^\tau / g_A^\tau}{g_V^{\rm e} / g_A^{\rm e}} = 0.95 \pm 0.16$$

where the statistical and systematic errors have been added in quadrature. Assuming lepton universality, the ratio of vector- to axial-vector couplings is,

$$g_V^\ell / g_A^\ell = 0.0763 \pm 0.0054 \pm 0.0033$$

Inserting this into equation 1.43 yields the effective weak mixing angle,

$$\sin^2 \theta_W^{\rm eff} = 0.2309 \pm 0.0016$$

Measurement	$\sin^2\theta_W^{\rm eff}$
$\mathcal{A}_{FB}^{b\bar{b}}$ [57]	0.2335 ± 0.0021
Combined [58]	0.2312 ± 0.0022

Table 7.1: Other L3 measurements of $\sin^2\theta_W^{\rm eff}$. $\mathcal{A}_{b\bar{b}}$ is the forward-backward charge asymmetry for b's and includes data taken from 1990-1992. The measurement labeled "combined" includes 1990-1992 data for the Z line shape and the forward-backward charge asymmetries for electrons, muons, and taus.

with the statistical and systematic errors combined in quadrature. This result is consistent with other L3 measurements of $\sin^2\theta_W^{\rm eff}$, shown in Table 7.1.

Figure 7.1 shows the variation of the top mass with $\sin^2\theta_W^{\rm eff}$ for a range of higgs masses. Table 7.2 gives the published results for for $\sin^2\theta_W^{\rm eff}$ and the latest preliminary results for $\mathcal{A}_\tau$, and $\mathcal{A}_{\rm e}$ from the other LEP experiments.

Experiment	$\sin^2\theta_W^{\rm eff}$	$\mathcal{A}_\tau$	$\mathcal{A}_{\rm e}$
ALEPH [59]	0.2332 ± 0.0022	$0.137 \pm 0.012 \pm 0.008$	$0.127 \pm 0.016 \pm 0.005$
DELPHI [60]	0.220 ± 0.009	$0.144 \pm 0.018 \pm 0.016$	$0.140 \pm 0.028 \pm 0.003$
OPAL [61]	0.2321 ± 0.0023	$0.153 \pm 0.019 \pm 0.013$	$0.122 \pm 0.030 \pm 0.012$

Table 7.2: Published and preliminary results of the τ polarization measurement from the other LEP experiments. The ALEPH and DELPHI results for $\sin^2\theta_W^{\rm eff}$ are the latest published values. The OPAL result for $\sin^2\theta_W^{\rm eff}$ is final and to be published. The values for $\mathcal{A}_\tau$ and $\mathcal{A}_{\rm e}$ include 1990-1992 data; the ALEPH and DELPHI values are preliminary and the OPAL values are final [58].

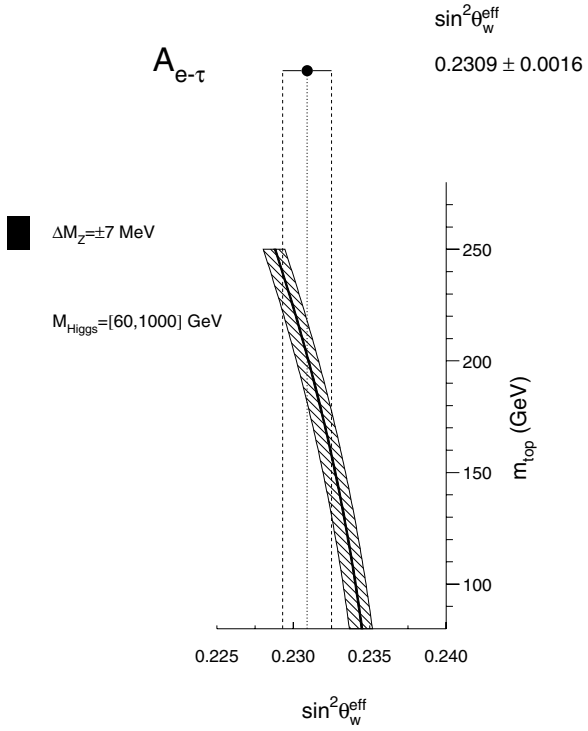

Figure 7.1: Variation of the top mass over a range of $\sin^2\theta_W^{\rm eff}$. The results of the L3 measurement of $\sin^2\theta_W^{\rm eff}$ from $\mathcal{A}_{\tau-{\rm e}}$ are superimposed.

Appendix A

Cross section for $e^+e^- \to \tau^+\tau^-$

The tree-level differential cross section for $e^+e^- \to \tau^+\tau^-$ is given by [10],

$$\begin{aligned}\frac{d\sigma}{d\cos\theta} &= A(s)\left(1+\cos^2\theta\right) + B(s)\left(2\cos\theta\right) \\ &+ \mathcal{P}_\tau\left[C(s)\left(1+\cos^2\theta\right) + D(s)\left(2\cos\theta\right)\right] \end{aligned} \tag{A.1}$$

where $\mathcal{P}_\tau$ is the τ polarization and,

$$\begin{aligned}A(s) &= \frac{\pi\alpha^2}{2s}\left[q_e^2 q_\tau^2 + 2\Re\chi(s) q_e q_\tau g_V^e g_V^\tau + |\chi(s)|^2\left((g_V^e)^2+(g_A^e)^2\right)\left((g_V^\tau)^2+(g_A^\tau)^2\right)\right] \\ B(s) &= \frac{\pi\alpha^2}{2s}\left[2\Re\chi(s) q_e q_\tau g_A^e g_A^\tau + 4\,|\chi(s)|^2 g_V^e g_A^e g_V^\tau g_A^\tau\right] \\ C(s) &= \frac{\pi\alpha^2}{2s}\left[2\Re\chi(s) q_e q_\tau g_V^e g_A^\tau + 2\,|\chi(s)|^2\left((g_V^e)^2+(g_A^e)^2\right) g_V^\tau g_A^\tau\right] \\ D(s) &= \frac{\pi\alpha^2}{2s}\left[2\Re\chi(s) q_e q_\tau g_A^e g_V^\tau + 2\,|\chi(s)|^2\left((g_V^\tau)^2+(g_A^\tau)^2\right) g_V^e g_A^e\right] \end{aligned} \tag{A.2}$$

with,

$$\chi(s) = \frac{s}{s - M_Z^2 + is\Gamma_Z/M_Z} \tag{A.3}$$

The terms in equations A.2 proportional to $|\chi(s)|^2$ describe pure Z exchange, and the terms proportional to $\Re\chi(s)$ originate from $\gamma-$Z interference. The remaining term in $A(s)$ is from pure photon exchange.

The cross sections and asymmetries discussed in section 1.5 may be written,

$$\sigma_{\rm tot} = \frac{8}{3}A(s)$$

$$\begin{aligned} \mathcal{A}_{FB} &= \frac{3}{4}\frac{B(s)}{A(s)} \\ \mathcal{P}_\tau &= -\frac{C(s)}{A(s)} \\ \mathcal{P}_\tau^{FB} &= -\frac{3}{4}\frac{D(s)}{A(s)} \end{aligned} \tag{A.4}$$

For $s = M_Z$ these expressions reduce to the relations between the asymmetries and coupling constants derived in section 1.5.

Bibliography

[1] E. Fermi *Nuovo Cimento* **11** (1934) 1;
E. Fermi *Z. Phys.* **88** 161.

[2] C.S. Wu, *Phys. Rev.* **105** (1957) 1413.

[3] R.L. Garwin, et al., *Phys. Rev.* **105** (1957) 1415;
J.I. Friedman and V.L. Telegdi, *Phys. Rev.* **105** (1957) 1581.

[4] H. Frauenfelder, et al., *Phys. Rev.* **106** (1957) 386.

[5] M. Goldhaber, L. Grodzins, and A.W. Sunyar, *Phys. Rev.* **109** (1958) 1015.

[6] F. Reins and C.L. Cowan, *Phys. Rev.* **113** (1959) 273;
R.E. Carter, et al., *Phys. Rev.* **113** (1959) 290.

[7] G. 't Hooft, *Nucl. Phys.* **B35** (1971) 167.

[8] F.J. Hassert et al., *Phys. Lett.* **46B** (1973) 138.

[9] C.Y. Prescott et al., *Phys. Lett.* **77B** (1978) 347.

[10] S. Jadach, Z. Was et al. in "Z Physics at LEP1", CERN Report CERN-89-08, eds G. Altarelli, R. Kleiss and C. Verzegnassi (CERN, Geneva, 1989) Vol. 1, p. 235.

[11] A. Rougé, "Tau Decays as Polarization Analysers" in Proceedings of the Workshop on Tau Lepton Physics, Orsay, France, September 1990, Eds. M. Davier and B. Jean-Marie.

[12] S. Glashow, *Nucl. Phys.* **22** (1961) 579;
S. Weinberg, *Phys. Rev. Lett.* **19** (1967) 1264;
A. Salam, Elementary Particle Theory, Ed. N. Svartholm, Stockholm, "Almquist and Wiksell" (1968), 367.

[13] UA1 Collab., *Phys. Lett.* **122B** (1983) 103;
UA2 Collab., *Phys. Lett.* **122B** (1993) 476;
UA1 Collab., *Phys. Lett.* **126B** (1983) 398;
UA2 Collab., *Phys. Lett.* **129B** (1983) 130.

[14] K. Hagiwara, A. D. Martin, D. Zeppenfeld, *Phys. Lett.* **B235** (1990) 198;
A. Rougé *Z. Phys.* **C48** (1990) 75.

[15] see for example I.J.R. Aitchison and A.J.G. Hey, *Gauge Theories in Particle Physics*, Adam Hilger, Briston and Philadelphia (1989);
F. Halzen and A. Martin, *Quarks and Leptons*, John Wiley and Dond, New York (1984).

[16] Y. S. Tsai, *Phys. Rev.* **D4** (1971) 2821.

[17] ARGUS Collab., *A. Phys.* **C58** (1993) 61.

[18] ALEPH Collab., *Phys. Lett.* **B321** (1994) 168.

[19] L3 Collab., *Nucl. Inst. Meth.* **A289** (1990) 35.

[20] H. Anderhaub et al., *Nucl. Inst. Meth.* **A235** (1985) 267.

[21] F. Beissel et al., *Nucl. Inst. Meth.* **A332** (1993) 33.

[22] A. Bay et al., UGVA-DPNC 1992/01-150 (1992).

[23] R. Sumner et al., *Nucl. Inst. Meth.* **A265** (1988) 252.

[24] O. Adriani et al., *Nucl. Inst. Meth.* **302A** (1991) 53.

[25] B. Adeva et al., *Nucl. Inst. Meth.* **277A** (1989) 187.

[26] L3 Collab., . *Z. Phys.* **C51** (1991) 179.

[27] S. Jadach, B.F.L. Ward and Z. Was, *Comput. Phys. Comm.* **60** (1991) 276.

[28] The L3 detector simulation is based on GEANT version 3.14. see R. Brun et al. "GEANT 3", CERN DD/EE/84-1, September 1987.

[29] R.P. Feynman, M. Gell-Mann, *Phys. Rev.* **109** (1958) 193;
E.C.G. Sudarshan, R.E. Marshak, *Phys. Rev.* **109** (1958) 1860.

[30] Particle Data Group *Phy. Lett.* **B239** (1992).

[31] J.H. Kühn, E. Mirkes, *Phys. Lett.* **B286** (1992) 381.

[32] I.J. Scott, Ph.D. thesis, Harvard University (1993).

[33] V. Karimaki, UA1/TN/82-24 (1982).

[34] H. Sens, P. Vikas, L3 Note 1027 (1991).

[35] L. Taylor, L3 Note 1480 (1993).

[36] F. Behner, G. Rahal-Callot, P. Zemp, L3 Note 1528 (1993);
F. Beissel et al., *Nucl. Inst. Meth.* **A332** (1993) 33-55.

[37] I. Vorobiev, private communication.

[38] S. Jézéquel, Y. Karyotakis, L3 Note 1272 (1992).

[39] O. Adriani, private communication.

[40] see for eg. L3 Collab., *Phys. Rev.* **236** (1993) 1.

[41] F. James, MINUIT Reference Manual, CERN Program Library, long writeup D506 (1992).

[42] O. Adriani et. al., L3 Note 1637 (1994).

[43] R. Barlow, C. Beeston, *Comp. Phys. Comm.*, **77** (1993) 219.

[44] L3 Collab., *Phys. Lett.* **B265** (1991) 451.
L3 Collab., "A Measurement of Exclusive Branching Fractions of Hadronic One-Prong Tau Decays" in preparation.

[45] D. Bardin et. al., FORTRAN package ZFITTER; CERN-TH 6443/92;
Z. Phys. **C 44** (1989) 493;
Nucl. Phys. **B 351** (1991) 1;
Phys. Lett. **B 255** (1991) 290.

[46] S. Kirsch, Ph.D. thesis, University of Berlin (1994).

[47] M. Finkemeir, Ph.D. thesis, University of Karlsruhe (1994).

[48] J. Shukla, Ph.D. thesis, Carnegie Mellon University (1994).

[49] J.H. Kühun, E. Mirkes, *Phys. Lett.* **B286** (1992) 381;
J.H. Kühun, E. Mirkes, *Z. Phys.* **C56** (1992) 661;
N. Isgur et al., *Phys. Rev* **D39** (1989) 1357;
M. Feindt, *Z. Phys.* **C48** (1990) 681.

[50] E.R. Cohen and B.N. Taylor, *Rev. Mod. Phys.* **59** (1987) 1121.

[51] W.J. Marciano and A. Sirlin, *Phys. Rev. Lett.* **61** (1988) 1815.

[52] LEP Electroweak Working Group, "Combined Preliminary Data on Z Parameters from the LEP Experiments and Constraints on the Standard Model" in preparation.

[53] ALEPH Collab., *Z. Phys.* **C62** (1994) 539;
DELPHI Collab., *Nucl. Phys.* **B418** (1994) 403;
L3 Collab., *Z. Phys.* **C62** (1994) 551;
OPAL Collab., *Z. Phys.* **C61** (1994) 19.

[54] see for eg. A. Olshevski, P. Ratoff, and P. Renton, CERN-PPE/93-88 (1993).

[55] V.A. Novikov, L.B. Okun, and M.I. Vysotsky, *Nucl. Phys.* **B397** (1993) 35;
V.A. Novikov, L.B. Okun, A.N. Rozanov, and M.I. Vyotsky, CERN-TH.7217/94 (1994).

[56] H. Burkhardt, F. Jegerlehner, G. Penso, and C. Verzegnassi, *Z. Phys.* **C43** (1989) 497.

[57] L3 Collab., *Z. Phys.* **C62** (1994) 551.

[58] L3 Collab., CERN-PPE/94-45 (1994).

[59] ALEPH Collab., *Z. Phys.* **C59** (1993) 369.

[60] DELPHI Collab., *Z. Phys.* **C55** (1992) 555.

[61] OPAL Collab., CERN-PPE 94-120 (1994).

[62] Consoli, et al. in "Z Physics at LEP1", CERN Report CERN-89-08, eds G. Altarelli, R. Kleiss and C. Verzegnassi (CERN, Geneva, 1989) Vol. 1, p. 7.; Burgers, et al. in "Z Physics at LEP1" Vol. 1, p. 55.